MICROWAVE SWITCHING AND ATTENUATION WITH SUPERCONDUCTORS

By

G. Darcy Poulin, B.Sc., M.Eng.

A Thesis

Submitted to the Faculty of Graduate Studies

in Partial Fulfilment of the Requirements

for the Degree

Doctor of Philosophy

McMaster University

July 1995

DOCTOR OF PHILOSOPHY (1995) **McMASTER UNIVERSITY**
(Engineering Physics) Hamilton, Ontario, Canada

TITLE: Microwave Switching and Attenuation with Superconductors

AUTHOR: G. Darcy Poulin, B.Sc. (Eng) (Queen's University)
M. Eng. (McMaster University)

SUPERVISOR: Dr. John S. Preston

NUMBER OF PAGES: xxiii, 94.

MICROWAVE SWITCHING AND ATTENUATION WITH SUPERCONDUCTORS

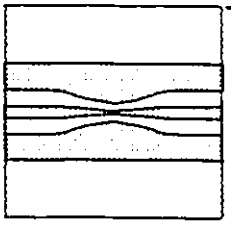

ABSTRACT

The discovery of high temperature superconducting (HTS) materials having a critical temperature above the boiling point of liquid nitrogen has generated a large amount of interest in both the basic and applied scientific communities. Considerable research effort has been expended in developing HTS microwave devices, since thin film, passive, microwave components will likely be the first area to be successfully commercialized.

This thesis describes a new thin film HTS microwave device that can be operated as a switch or as a continuously variable attenuator. It is well suited for low power analog signal control applications and can easily be integrated with other HTS devices. Due to its small size and mass, the device is expected to find application as a receiver protection switch or as an automatic gain control element, both used in satellite communications receivers. The device has a very low insertion loss, and the isolation in the OFF state is continuously variable to 25 dB. With minor modifications, an isolation exceeding 50 dB is readily achievable. A patent application for the device has been filed, with the patent rights assigned to COM DEV.

The device is based on an unusual non-linear response in HTS materials. Under a non-zero DC voltage bias, the current through a superconducting bridge is essentially voltage independent. We have proposed a thermal instability to account for this behaviour. Thermal modelling in conjunction with direct temperature measurements were used to confirm the validity of the model.

We have developed a detailed model explaining the microwave response of the device. The model accurately predicts the microwave attenuation as a function of the applied DC control voltage and fully explains the device operation. A key feature is that the device acts as a pure resistive element at microwave frequencies, with no reactance. The resistance is continuously variable, controlled by the DC bias voltage. This distinguishes it from a PIN diode, since PIN diodes have a capacitive reactance that limits their frequency range.

Measurements made to confirm the microwave model validity resulted in the development of a new cryogenic de-embedding technique. The technique allows accurate microwave measurements to be made on devices at cryogenic temperatures using only room temperature calibration standards. We have also investigated the effect of kinetic inductance on coplanar waveguide transmission lines, and indicate under what conditions kinetic inductance must be considered in transmission line design.

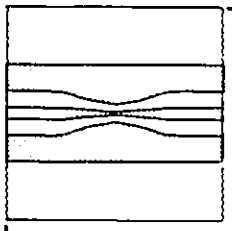

PREFACE

In this thesis, we have developed a new type of superconducting microwave device. The device can be used either as a switch or as a continuously variable attenuator. Our main contribution has been in understanding the principles of operation of the device, and we have not tried to design a fully engineered "off-the-shelf" component. In fact, the device is not well suited to be manufactured as a stand alone part, but is intended to be integrated into a larger assembly of superconducting components.

The thesis is intended for both physicists and microwave engineers, so it may be pedagogic at times. For example, the two fluid model and the London equations of Chapter 2 are well understood by physicists, but are quite foreign to many electrical engineers. Conversely, the basic transmission line theory presented in Chapter 4 will be very familiar to a microwave engineer, but a physicist may be unaccustomed to it.

Chapter 1 presents a general introduction to the use of superconductors in microwave engineering. Chapter 2 reviews necessary superconductivity theory and shows our electrical measurements of superconducting bridges. The measurements show that a superconducting bridge switches from a lossless to a lossy state under an applied DC bias voltage.

To understand the mechanism behind the switching phenomenon, we present a thermal "hotspot" model in Chapter 3. Measurements show that switching occurs with the formation of a small region of the bridge heated above T_c. The model correctly predicts both the measured flat-topped temperature distribution associated with the hotspot and the device resistance as a function of applied DC bias voltage.

Chapter 4 presents the background microwave theory necessary to understand the microwave modelling carried out in Chapter 5, where two different models are developed. At

low frequencies, the hotspot can be considered to be a lumped element resistor, with dimensions much smaller than the wavelength of the microwave signal. From this model, we found that the microwave resistance of the hotspot is equal to its DC resistance. At higher frequencies, a distributed loss transmission line model was developed. This model gives good agreement with measured microwave transmission over the entire frequency range of interest, and allowed us to conclude that the hotspot can be modelled as a pure resistance at all frequencies.

Finally, a summary of the final film processing methodology used to fabricate the devices studied in this thesis is included in Appendix 1. The procedures used to develop this methodology have not been included since they involved a great deal of trial and error.

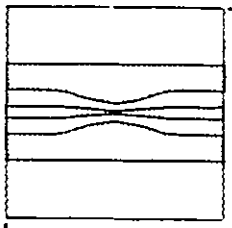

ACKNOWLEDGEMENTS

I have been fortunate to have been involved in a very dynamic research group during my studies at McMaster. For providing an excellent research environment, for his guidance, and for his optimism, I am deeply indebted to Dr. John Preston. I also want to thank Frank Hegmann, Steve Moffat, and Jean Lachapelle, all of whom contributed greatly to the work here. In particular, Frank was the catalyst for the entire project, having first seen the DC switching response, and was always available to bounce ideas off, whether in the lab or in the pool hall. Steve built a top notch measurement apparatus that he allowed me to use extensively, and was the first to propose a hotspot to explain some odd results I had seen and was ready to dismiss as due to a contact problem. He is also a formidable cycling partner, always pushing me through the Headwaters Trail in the Dundas Conservation Area. Jean ably tackled the difficult problem of solving the differential equations describing the hotspot, and gave me a great opportunity to practise my French. I would also like to thank Rob Hughes, Bruce Takasaki, and Gary Dyck for making the lab a fun place to work in.

I am also indebted to Dr. D. Conn and Kent Nickerson at CRL for giving me access to the network analyzer and for introducing me to many of its capabilities. In addition, Dr. Conn was always available to answer my microwave questions, and was sincerely interested in my progress. Venice Perno and Gino Innocente in the machine shop were both invaluable, helping me in many of my designs. Michael Roberts in the instrument machine shop did an outstanding job in machining many intricate microwave housings for me, while Mike Clarke allowed me to use his gold evaporation system. I also want to thank Elaine Moore, Bobby Kartonchik and Fran Allen for their tireless efforts in dealing with all of the graduate students in the department.

I would also like to acknowledge Dr. R. Mansour and Dr. C. Kudsia at COM DEV. Dr. Mansour helped me in investigating my package resonance problems, while Dr. Kudsia kept me on course as a member of my supervisory committee. I would also like to thank COM DEV for supporting our patent application.

Outside the University, my parents Conrad and Sybil Poulin and good friends Margaret and Adam Wiley have given me a ton of support over the past few years. While none of them really knew what I was working on, they were eternally enthusiastic.

Most of all, I want to thank the love of my life, Dawn, for her support, companionship, and inspiration.

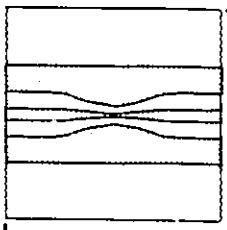

TABLE OF CONTENTS

Chapter 1. INTRODUCTION 1
1.1. Overview of Microwave Superconducting Devices 1
1.2. Microwave Switches and Attenuators 4

Chapter 2. SUPERCONDUCTIVITY AND DC BIASED BRIDGES 9
2.1. Overview of Superconductivity 9
2.2. The London Equations 10
2.3. The Two Fluid Model 13
2.4. Microwave Surface Resistance 15
2.5. DC Biased Superconducting Bridges 18
2.5. Measured I-V Curves for DC Voltage Biased Bridges 21

Chapter 3. THE HOTSPOT MODEL 23
3.1. The Hotspot Model 23
3.2. Hotspot Temperature Distribution Measurements 28
3.3. Hotspot Modelling Results 32
3.4. Optimizing Device Performance 34

Chapter 4. MICROWAVE THEORY 37
4.1. Microwave Engineering 37
4.2. Transmission Line Theory 39
4.3. Scattering Parameters 47
4.4. Lossy Transmission Lines 48
4.4.1. The Lumped Element Approximation 49
4.4.2. The Distributed Loss Model 50
4.5. Coplanar Waveguide Design 53

Chapter 5. MICROWAVE MEASUREMENTS 57
5.1. Packaging 57
5.2. Microwave Network Analyzer 60
5.3. Microwave Measurements and the Lumped Element Model 63
5.4. Microwave Measurements and the Distributed Transmission Line Model 67
5.5. Discussion 77

Chapter 6. CONCLUSIONS 79

Appendix 1. FILM PROCESSING 83

REFERENCES 87

PUBLICATIONS

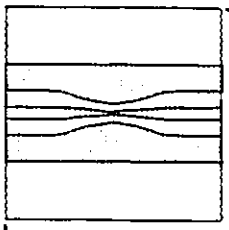

LIST OF PUBLICATIONS

The following publications and a brief summary of their contents and significance are included at the end of the thesis.

1. **Patent Application**

"Voltage Controlled Superconducting Microwave Switch and Method of Operation Thereof"

G. Darcy Poulin, Frank A. Hegmann, Steven H. Moffat, and John S. Preston

2. **Paper A**

"A Superconducting Microwave Switch"

G. Darcy Poulin, Frank A. Hegmann, Jean Lachapelle, Steven H. Moffat, and John S. Preston

IEEE Trans. Appl. Supercond. **5**, 3046 (1995).

3. **Paper B**

"Current-Voltage Characteristics of DC Voltage Biased High Temperature Superconducting Microbridges"

G. Darcy Poulin, Jean Lachapelle, Frank A. Hegmann, Steven H. Moffat, and John S. Preston

Appl. Phys. Lett. **66**, 2576 (1995).

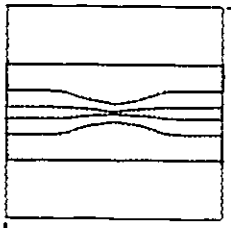

LIST OF ILLUSTRATIONS

Fig. 2.1. Electrical model of a superconductor. 14

Fig. 2.2. Schematic representation of the DC measurement apparatus. 19

Fig. 2.3. Typical I-V curve for a superconductor. 20

Fig. 2.4. DC measurements on the 5 μm wide bridge. 22

Fig. 2.5. DC measurements on the 10 μm wide bridge. 22

Fig. 3.1. Typical I-V curve for a DC voltage biased superconducting bridge. 23

Fig. 3.2. One dimensional model of heat transport in a superconducting bridge. 24

Fig. 3.3. Device used for hotspot temperature measurements. 28

Fig. 3.4. Resistivity versus temperature used for computing hotspot temperature as a function of position. 29

Fig. 3.5. Measured tap voltage as a function of position for different bridge voltages. 30

Fig. 3.6. Temperature as a function of position for different bridge voltages. 30

Fig. 3.7. Hotspot length as a function of bridge voltage. 31

Fig. 3.8. I-V curve for the DC voltage biased bridge. 31

Fig. 4.1. Series circuit with resistor used to derive Kirchoff's laws. 37

Fig. 4.2. Three of the most common types of microwave transmission lines. 40

Fig. 4.3. An incremental section of a transmission line. 42

Fig. 4.4. A transmission line terminated in an arbitrary load impedance Z_L. 45

Fig. 4.5. A two port network. 47

Fig. 4.6. Transmission line of characteristic impedance Z_0 with a series lumped element impedance Z. 49

Fig. 4.7. Microwave model used to describe the effect of a hotspot on microwave transmission. 50

Fig. 4.8. Relationship between center conductor width and the gap between the center conductor and the ground plane for 50 Ω coplanar waveguide. 55

Fig. 4.9. Effective dielectric constant as a function of the center conductor width for a 50 Ω coplanar waveguide transmission line. 55

Fig. 5.1. Microwave housing assembly used for all microwave measurements. 58

Fig. 5.2. Reflection coefficient as a function of applied bias, normalized to the unbiased reflection coefficient, for a tapered CPW transmission line. 64

Fig. 5.3. Transmission coefficient as a function of applied bias, normalized to the unbiased transmission coefficient. 64

Fig. 5.4. Calculated microwave resistance and DC resistance versus bridge voltage at three different microwave frequencies. 65

Fig. 5.5. Measured and modelled transmission coefficient magnitude versus frequency for bias voltages from 1 to 10 V applied to the 5 μm CPW transmission line. 68

Fig. 5.6. Measured and modelled transmission coefficient phase versus frequency for applied bias voltages from 1 to 10 V applied to the 5 μm CPW transmission line. 69

Fig. 5.7. Calculated hotspot length as a function of bridge voltage for the 5 μm wide CPW transmission line. 71

Fig. 5.8. Magnitude and phase of the characteristic impedance of a hotspot having a resistance per unit length of 1.4 Ω/μm. 71

Fig. 5.9. Calculated propagation constant as a function of frequency for a hotspot with a resistance per unit length of 1.4 Ω/μm. 72

Fig. 5.10. Time domain transmission for the 5 μm wide tapered CPW transmission line for bias voltages from 0 to 10 V. 73

Fig. 5.11. Attenuation versus frequency for three different applied bias voltages. 74

Fig. 5.12. Measured and modelled S_{21} magnitude data for a CPW transmission line tapering to a final width of 10 μm. 75

Fig. 5.13. Measured and modelled S_{21} phase data for a CPW transmission line tapering to a final width of 10 μm. 75

Fig. 5.14. Hypothetical transmission coefficient for a CPW transmission line tapering to a final center conductor width of 1 μm. 76

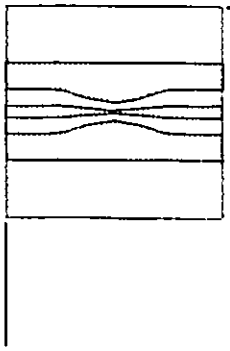

LIST OF TABLES

Table 1.1. Table comparing specifications and features of various types of microwave switches. 7

Table 3.1. Effects of various changes on hotspot length, resistance, and power consumption. 35

Table 5.1. Network analyzer calibration summary. 61

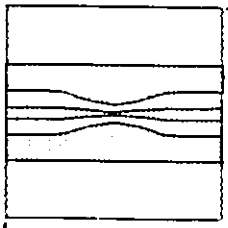

ABBREVIATIONS, VARIABLES, AND CONSTANTS

Abbreviations

ρ-T	resistivity versus temperature
AM	amplitude modulation
CBCPW	conductor backed coplanar waveguide
CPW	coplanar waveguide
dB	decibel, $P(dB) = 10\log_{10}(P/P_0) = 20\log_{10}(V/V_0)$
dBm	decibel with a 1 mW reference level, $P(dBm) = 10\log_{10}(P/[1mW])$ 0 dBm = 1 mW, 10 dBm = 10 mW, 20 dBm = 100 mW.
DVM	digital voltmeter
EMF	electromotive force
GHz	Gigahertz [10^9]
HTS	high temperature superconductor
HTSSE	high temperature superconductivity space experiment
I-V	current versus voltage
J_c	critical current density, normally defined as the current density which results in an electric field of 1 μV/cm. [MA/cm^2]
K	degrees on the Kelvin temperature scale. [K = °C+273.15]
MHz	Megahertz [10^6]
MMIC	monolithic microwave integrated circuit
S parameters	scattering parameters
SMU	source measure unit; a device that can act as a voltage source, and measure current, or as a current source, measuring voltage

SQUID	superconducting quantum interference device
T_C	critical temperature [K]
TE	transverse electric
TEM	transverse electric and magnetic
THz	Terahertz [10^{12}]
TM	transverse magnetic

Variables and Constants

Parameter	Description	Typical Units
α	attenuation coefficient	m^{-1}
α	heat transfer coefficient	$Wcm^{-2}K^{-1}$
β	wave number, $2\pi/\lambda$	m^{-1}
γ	complex propagation constant, $\gamma = \alpha + j\,\beta$	m^{-1}
Γ	microwave reflection coefficient	dimensionless
δ	skin depth	m^{-1}
Δl	spacing between voltage taps	μm
ϵ	dielectric constant	F/m
ϵ_{eff}	effective dielectric constant	dimensionless
ϵ_0	permittivity of free space	F/m
ϵ_r	relative dielectric constant, $\epsilon = \epsilon_r\,\epsilon_0$	dimensionless
η	wave impedance, E/H	Ω
η_N	thermal healing length in normal region	μm^{-1}
η_S	thermal healing length in superconducting region	μm^{-1}
λ	wavelength	mm
λ_L	London penetration depth, $\lambda_L = \left(m/\mu n q^2\right)^{1/2}$	nm
μ	permeability	H/m
ρ	resistivity	Ωcm
ρ_0	zero temperature resistivity intercept	Ωcm

Parameter	Description	Typical Units
σ	conductivity	$(\Omega\text{-m})^{-1}$
σ_N	conductivity due to normal electrons	$(\Omega\text{-m})^{-1}$
σ_S	conductivity due to superconducting electrons	$(\Omega\text{-m})^{-1}$
τ_s	electronic scattering time	ps
ω	radian frequency, $\omega=2\pi f$	radians/s
A	cross sectional area	m^2
A_{TOTAL}	total attenuation	dB
c	speed of light	$2.998\text{x}10^8$ m/s
C	capacitance per unit length	F/m
d	thickness of superconducting film	nm
$\boldsymbol{E}$	electric field	V/m
f	frequency	Hz $[s^{-1}]$
f_A	fraction of attenuation due to absorption	dimensionless
f_R	fraction of attenuation due to reflection	dimensionless
g	gap width in CPW transmission line	µm
G	shunt conductance per unit length	$(\Omega\text{-m})^{-1}$
h	thickness of dielectric	µm
$\boldsymbol{H}$	magnetic field	A/m
I	transmission line current with arbitrary time dependence	A
I	transmission line current with sinusoidal time dependence	A
$\boldsymbol{I}$	electric current	A
j	$\sqrt{-1}$, denotes a complex number	-----
$\boldsymbol{J}$	electric current density	A/m^2
K_N	thermal conductivity in the hotspot	$Wcm^{-1}K^{-1}$
K_S	thermal conductivity in the superconductor	$Wcm^{-1}K^{-1}$
L	inductance per unit length	H/m
L_{KIN}	kinetic inductance per unit length	H/m

Parameter	Description	Typical Units
m	mass of electron	9.11×10^{-31} kg
n	number of electrons per unit volume	m^{-3}
n_N	number of normal electrons per unit volume	m^{-3}
n_S	number of superconducting electrons per unit volume	m^{-3}
P_A	absorbed power	W
P_I	incident power	W
P_R	reflected power	W
P_T	transmitted power	W
q	electronic charge	C
R	resistance per unit length	Ω/m
R_S	surface resistance	Ω
S_{11}	microwave reflection coefficient (for matched load only)	dimensionless
S_{21}	microwave transmission coefficient (matched load only)	dimensionless
T	microwave transmission coefficient	dimensionless
T	temperature	K
T_b	bath temperature	K
v	mean electron velocity	m/s
v	transmission line voltage with arbitrary time dependence	V
V	transmission line voltage with sinusoidal time dependence	V
V_0^+	complex amplitude of forward travelling voltage wave	V
V_0^-	complex amplitude of backward travelling voltage wave	V
V_{app}	applied voltage	V
V_b	voltage appearing across the superconducting bridge	V
v_p	phase velocity, $\left[c/\sqrt{\epsilon_{eff}},\ 1/\sqrt{LC}\right]$	m/s
w	width of center conductor in CPW transmission line	μm
W	width of superconducting bridge	μm
x_0	position of hotspot-superconductor interface	μm

Parameter	Description	Typical Units
Z_0	characteristic impedance, $\sqrt{L/C}$	Ω
Z_L	load impedance	Ω

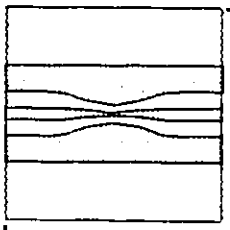

INTRODUCTION

1.1. Overview of Microwave Superconducting Devices

The discovery of high temperature superconducting (HTS) materials having a critical temperature above the boiling point of liquid nitrogen has generated a large amount of interest in both the basic and applied scientific communities. Considerable research effort has been expended in developing HTS microwave devices, since it is expected that thin film, passive, microwave components may be the first area to be successfully commercialized. A variety of HTS microwave prototypes have been developed that have demonstrated performance advantages over similar devices based on conventional technology. HTS devices are now being considered for microwave systems where small size, low weight, and high performance are necessary.

The development of HTS microwave devices was precipitated by a US Navy program: the High Temperature Superconductivity Space Experiment (HTSSE).[1] HTSSE is a program funded by the Naval Research Laboratory (NRL) with goals of demonstrating the feasibility of incorporating HTS materials into space systems and of reducing the time required to insert the technology into operational satellite systems. The program, initiated in 1988, is non-traditional, funding many research organizations and encouraging them to share information to attain these goals. The first phase of the program, HTSSE I, involved devices from twenty industrial research organizations, and included a number of filters, resonators, antennas, and delay lines. Devices were delivered in 1990, with a launch in 1993.[a] The second phase of the

[a]As a result of the Challenger explosion in 1986, there was a large backlog of payloads and the NRL had to put HTSSE I on a military rocket in early 1993. All that is known of the mission is that it "did not achieve orbit" presumably exploding during takeoff. All devices were lost, but their operation was demonstrated on the ground.

program, HTSSE II, continued in the same manner, with a goal of producing a complete HTS assembly. All devices have now been delivered to NRL, and launch is expected in 1996.

The development of HTS microwave devices has been greatly influenced by the HTSSE program. Early device contributors included large industrial laboratories such as Westinghouse[2], MIT Lincoln Laboratories[7], and the Naval Research Laboratories[7]. In Canada, COM DEV has developed filters[3] and multiplexers[4] both for HTSSE II and for internal use. HTSSE has also greatly benefitted film suppliers such as Dupont, Conductus, and Superconducting Technologies Inc. (STI), and has helped in funding their device development programs. Dupont seems to have emerged as the main supplier of high quality films, while Conductus and STI appear to be focussing on devices in a variety of applications areas.

Two excellent review articles[5,6] give a general overview of applications areas of HTS materials. Perhaps one of the most poignant examples of an area in which HTS microwave devices can be used advantageously is in the field of satellite communications. A typical twenty-four channel communications satellite must receive ground based signals, amplify them, then re-transmit them over a broad area. Since it is not possible to design a linear amplifier covering the entire bandwidth of the received signal, the signal must first be 'channelized', or split, into smaller frequency segments. Each of these channels is amplified individually, then recombined, or multiplexed, for transmission. Channelizing involves passing the received signal through many microwave filters, each tuned to a slightly different frequency. The filter characteristics are very important; the rolloff at the edges of the passband determines how closely spaced adjacent channels can be without introducing signal distortion. Because the overall bandwidth allocated to the satellite is fixed, filter characteristics ultimately determine the satellite information capacity. Therefore, only waveguide filters have been used in communication satellites to date, since smaller planar filters fabricated with gold or copper conductors are too lossy and therefore do not exhibit sharp enough rolloff characteristics. These waveguide filters are large and heavy; the filters, their mechanical support and wiring harnesses represent approximately one-eighth of the total 1500 kg mass of a typical communication satellite. With launching costs of approximately $50,000 per kilogram, there is a large driving force behind producing smaller, lighter, filters.

Superconductors, with their greatly reduced losses, exhibit similar performance in planar geometries as conventional waveguide filters. Because of the planar geometry, they do so with greatly reduced weight and volume, even after adding in the cryogenic system required to cool the superconducting components down to a suitable operating temperature.

The development of superconducting bandpass filters has been one of the most active areas in applied superconductivity, and a variety of filters have been demonstrated over the past five years.[7,8] In general, high performance filters can be made from HTS materials. More recently, companies have been developing filters for the cellular phone communications market[9], with the filters targeted for use in cellular phone base stations.

In addition to filters, superconductors are also being developed for other microwave devices, with the goal of constructing a complete communications system using HTS materials. For example, heterodyne communications receivers require a mixer to convert the incoming signal to a lower intermediate frequency, using a device with a non-linear I-V curve. With conventional materials, a diode is commonly used as the non-linear device. However, Josephson junctions fabricated from HTS films also have a non-linear I-V characteristic and superconducting mixers have been developed that operate to 61 GHz.[10,11] Another device under development is a superconducting delay line. Delay lines (or phase shifters) are used in phased array antennas and are an integral component in signal processing. Because of their low losses, stripline[12] and coplanar waveguide[13] superconducting transmission lines have been developed to produce up to 25 ns of delay with losses of 0.08 dB/ns on a two-inch diameter $LaAlO_3$ substrate. These wafers can be cascaded, and delays of 100 ns have been demonstrated by placing four wafers in series. Conventional delay lines are fabricated using a long piece of coaxial cable. With RG-142 coaxial cable, one would require 20 m of cable and the loss would be 0.3 dB/ns in generating a 100 ns delay.

The future of applied high temperature superconductivity is currently at a critical point in its evolution. A variety of devices have been demonstrated, but to date no commercially viable applications have emerged, and the entire technology has been existing on government sponsored research programs. Clearly this state cannot continue to exist, and all of the companies involved are in need of a paying customer. While it is unclear when this will

happen, it may occur with the development of superconducting satellites or cellular phone base stations.

1.2. Microwave Switches and Attenuators

Switches are used extensively in microwave systems. They are used both to direct signal flow between components, and to construct other types of control circuits such as phase shifters. The two most important parameters used in characterizing a switch are the insertion loss and the isolation. Ideally, a switch would have no loss in the ON state, and infinite loss in the OFF state. The small, non-zero loss in the ON state is called the insertion loss, while the loss in the OFF state is the isolation.

There are several different types of microwave switches. The two most common types are the mechanical and the PIN diode switch. Mechanical switches are composed of a simple mechanical relay. They have low insertion loss, high isolation, and can handle high power levels. However, mechanical switches are slow, and often require large amounts of power to operate since they are actuated by energizing an electromagnet. They also cannot be used as variable attenuators, since they are binary devices; they are either on or off.

Semiconductor-based PIN diodes are the most widely used type of microwave switch. This device comprises a p-type anode separated from an n-type cathode by an undoped, intrinsic region. While the I-V characteristic of the PIN diode is very similar to that of a pn junction, the presence of the intrinsic region greatly reduces the junction capacitance[14] by increasing the length of the depletion region. A diode in the OFF state can be modelled[15] as a capacitance in series with a small resistance, so a small capacitance is imperative in achieving large impedances and therefore high isolation. This capacitance ultimately limits the frequency response of the device. When the PIN diode is forward biased, the junction capacitance is removed, and the diode is in a very low impedance state. In general, PIN diodes have high isolation, a large insertion loss, and are fabricated using silicon. However, there has been considerable effort in the past ten years to develop a suitable GaAs PIN diode. While the characteristics of Si and GaAs PIN diodes are similar, GaAs is the material of choice for monolithic microwave integrated circuits (MMIC's). Because the electron mobility

in GaAs is much larger than in silicon, GaAs transistors operate at much higher frequencies, and GaAs MMIC's are now quite common. The disadvantage of MMIC PIN diodes is that they typically have insertion losses even larger than their bulk semiconductor counterparts. PIN diodes can also be used as voltage controlled attenuators in microwave control circuits.

In this thesis, we present a superconducting microwave device that can be operated either as an attenuator or as a switch. As we have seen, superconductors are used in a variety of microwave devices, and a superconducting switch will be an important adjunct component for high performance signal control circuits. Of course the main advantage of using superconducting devices is that they exhibit very low microwave losses, so a superconducting device will have a very small insertion loss. Additionally, semiconductor-based devices are difficult to integrate with high temperature superconducting materials. If a complete HTS microwave circuit is to be assembled, superconducting switches and attenuators will be important.

Several types of superconducting microwave switches have been developed. Martens *et al.* proposed[16] a coplanar waveguide switch with an external heater to raise the temperature of a small region of the transmission line above T_C, resulting in switching. They were able to produce a switch with an isolation of approximately 30 dB over a frequency range of 0.5 to 8.5 GHz. To reduce the power dissipated by the switch, they thinned the film from 200 to 50 nm and used thermal insulation above the heated section of the film, achieving switching with only 5 mW of heater power. The overall design of this switch is similar to the switch proposed in this thesis, and its frequency range can likely be extended to 30 GHz or more. By varying the applied heater power, it should also be possible to use this device as a variable attenuator.

A second type of switch, developed by researchers at STI,[17] is an optically switched HTS bandstop filter. This device differs markedly from the switches described above, as it is inherently a very narrow bandwidth device. It comprises three U shaped hairpin resonators in parallel with a transmission line, with each resonator "shorted" by a piece of semi-insulating GaAs. The GaAs is switched optically using a fiber optic signal. When no light is incident on the GaAs, it is resistive and the resonator is open circuited. When light is incident on the

GaAs, it becomes conductive and the resonator is short circuited. In this fashion, the band reject region is shifted to higher frequencies, so that "switching" occurs. The insertion loss of the device was 2 dB, and isolation of 50 dB was reported. The rather large insertion loss is caused by a finite resistance of the GaAs in the resistive state. Power consumption for the three resonator device was ≈15 mW, or 5 mW per fiber.

In this thesis, we have developed a new type of microwave device. The device is composed of a tapered coplanar waveguide transmission line, and switching is accomplished by the application of a DC bias voltage to the center conductor of the transmission line. In Chapter 3, we derive a thermal model that explains the observed DC response of the device. We show that switching occurs due to the formation of a small region in the transmission line heated above the critical temperature, T_C. This "hotspot" is shown to have a flat-topped temperature distribution independent of the applied DC bias voltage. Its length increases linearly with the applied bias, so the DC resistance of the hotspot is a linear function of the voltage. In Chapters 4 and 5, the microwave response of the device is investigated. It was found that the device is purely resistive in the switched state, with a microwave resistance equal to the DC resistance. A transmission line model is derived that explains the measurements and allows predictions to be made to optimize device performance. Because the hotspot is purely resistive, there are no parasitic elements to limit the operating bandwidth of the device as there is in PIN diodes. The switch can also be used as a voltage controlled variable attenuator. The attenuation is shown to be virtually continuously variable between zero and its maximum value.

To summarize, the superconducting device discussed in this thesis has very low insertion loss, wide operating bandwidth, and is easy to integrate with other superconducting components. Its disadvantages are that it is only useful for relatively low power levels, has a relatively slow switching speed, and has only moderate isolation. Due to the slow switching speed, the device cannot be used for high speed digital applications. However, it could be used advantageously in analog microwave signal control applications. Table 1.1 shows a summary of the various types of switches, comparing key features of each.

	Mechanical Switch	COM DEV Mechanical Switch	Discrete PIN Diode Switch	MMIC GaAs PIN Diode Switch	Marten's HTS Switch	5 μm Tapered CPW HTS Switch	Hypothetical 1 μm Tapered CPW HTS Switch
Insertion Loss (dB)	0.2 dB @ 2 GHz 0.4 dB @ 12 GHz NA @ 30 GHz	NA @ 2 GHz 0.3 dB @ 12 GHz NA @ 30 GHz	0.8 dB @ 2 GHz 1.1 dB @ 12 GHz NA @ 30 GHz	1 dB @ 2 GHz 2.1 dB @ 12 GHz NA @ 30 GHz	≈0 dB	≈0 dB	≈0 dB
Isolation (dB)	80 dB @ 2 GHz 60 dB @ 12 GHz NA @ 30 GHz	NA @ 2 GHz 65 dB @ 12 GHz NA @ 30 GHz	75 dB @ 2 GHz 95 dB @ 12 GHz NA @ 30 GHz	65 dB @ 2 GHz 55 dB @ 12 GHz NA @ 30 GHz	32 dB @ 2 GHz NA @ 12 GHz NA @ 30 GHz	20 dB @ 2 GHz 22 dB @ 12 GHz 30 dB @ 30 GHz	32 dB @ 2 GHz 50 dB@ 12 GHz 70 dB@ 30 GHz
Bandwidth	DC-26 GHz	10.95-12.75 GHz	2-18 GHz	DC-20 GHz	0.5-8.5GHz	DC - >30 GHz	DC - >30GHz
Power Consumption	3.9 Watts	Negligible except during switching	625 mW	0.25 mW	5 mW	125 mW	25 mW
Switching Speed	≈15 ms	20 ms	20 ns	3 ns	On-Off 0.75μs Off-On 4 μs	Not Measured, but estimated at≈500 μs	Not Measured.
Power Handling	High (Several Watts)	High (10 Watts)	Moderate (≈100 mW)	Low (≈10 mW)	Low (≈ 4 mW)	Moderate (≈100 mW)	Low (≈20 mW)
Mass	NA	50 g	8 g	1 mg (plus connectors)	NA	3.25 mg (plus connectors)	3.25 mg (plus connectors)
Ease of Fabrication	Poor	Poor	Poor	Poor	Good	Good	Good
Ease of Integration with HTS	Poor	Poor	Poor	Poor	Good	Good	Good
Reference	Loral Part Number SEM124	COM DEV Ku- band SMA switch	Watkins-Johnson Part Number WJ-MSE133	MA-COM Part Number. MASW20000	Reference 16	Chapter 5	Chapter 5

Table 1.1. Table comparing specifications and features of various types of microwave switches. The COM DEV switch is self latching, so power is consumed only during switching. Power handling for all superconducting switches was estimated assuming that the maximum incident microwave power is 75% of the DC power dissipated in the switched state. Switching times for the tapered CPW switch are estimates only, based on measurements presented in Ref. 67. Actual switching times may be faster, since it is not clear why the switching speed should be two orders of magnitude slower than Martens' switch.

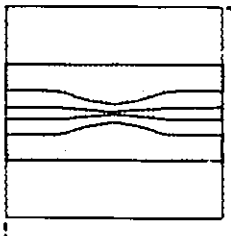

SUPERCONDUCTIVITY AND DC BIASED BRIDGES

2.1. Overview of Superconductivity

The phenomenon of superconductivity was first discovered in mercury in 1911 by a Dutch researcher, Heike Kamerlingh Onnes.[18] Over the next seventy years, steady research efforts succeeded in identifying many other superconducting elements and compounds. By the mid 1980's, more than three dozen elements and a number of binary compounds were known to be superconducting. The material with the highest critical temperature (T_C) was Nb_3Ge, with T_C=23K. The theory describing superconductivity was well understood, and the entire technology was quite mature. Research in the field had peaked in the early 1970's, and interest in these exotic materials had dwindled considerably. However, late in 1986, Bednorz and Müller[19] at the IBM research laboratories in Zurich discovered a new material, $La_{1.85}Ba_{0.15}CuO_4$, with a critical temperature of 35K. This discovery was closely followed by one even more startling. A similar compound, $YBa_2Cu_3O_{7-\delta}$[b], with a critical temperature of 93K, was discovered by Wu, Ashburn, and Torng[20] in January of 1987. The discovery of a material that could be operated in liquid nitrogen sparked a massive surge of research interest. Research investigating other superconductors has continued, and materials with even higher critical temperatures have been discovered. Currently, the material with the highest T_C is a HgBaCaCuO compound, exhibiting T_C=164K under pressure.

An equally intense effort has been devoted to developing superconductor applications. The fact that these new materials can be cooled by liquid nitrogen is an enormous advantage, since liquid nitrogen is cheap and readily available. In Chapter 1, a variety of applications in

[b]The superconducting properties of $YBa_2Cu_3O_{7-\delta}$ are quite sensitive to the oxygen content. The properties are optimal if the material is slightly oxygen deficient with $\delta \approx 0.1$.

microwave engineering were discussed. However, superconductors also find application in myriad other fields.[21] For example, superconductors are currently either in use or in development for use in power transmission, magnetic energy storage, electronics, photodetection, magnetically levitated trains, electromagnetic shielding, high field magnets, and as ultra-sensitive detectors of magnetic fields. Each of these applications uses a different feature of superconductivity which gives the superconductor a unique advantage over traditional technology. In power transmission, a superconducting wire can carry a much larger electrical current than can copper, so superconductors are currently under development to replace the overcrowded electrical conduits in large urban centers where there is simply not enough room to run more conduits. In shielding applications, due to the Meissner effect, superconductors can screen out electromagnetic fields down to very low frequencies where any traditional technique would fail. When superconductors are fabricated into a superconducting quantum interference device (SQUID), extremely small quantities of magnetic flux can be detected, several orders of magnitude smaller than can be detected with any other technique. SQUIDs are being developed for use in magnetoencephalography (the magnetic equivalent of an EEG), and in mineral exploration.

2.2. The London Equations

To be classified as a superconductor, a material must possess two characteristics. First of all, it must have zero DC resistance[c] for temperatures below the critical temperature. Secondly, a superconductor must expel magnetic fields, a phenomenon known as the Meissner effect. The Meissner effect is important in explaining the behaviour of superconductors in applied DC magnetic fields. However, if no DC field is applied, the behaviour of a superconductor can be well described without the Meissner effect. When high

[c] Strictly speaking, the DC resistance will only be zero in the limit that the DC current approaches zero, as there are very small losses which arise for any finite current. For all practical purposes, however, the DC resistance of a superconductor is zero as long as the current is kept much smaller than the critical current density. For example, persistent currents set up in superconducting loops have been monitored, and they have been shown to flow for many years without any signs of decay, putting an upper limit on the DC resistivity of $10^{-25}\ \Omega$.

frequency fields are applied to a superconductor, the fields are still screened out, but the screening is caused by simple eddy currents and the Meissner effect is not relevant.

The London equations[22], developed by Heinz and Fritz London between 1935 and 1940, are useful for modelling superconductor electrodynamics. The first London equation is derived using a phenomenological theory allowing us to investigate the consequence of a material with zero DC resistance. In conjunction with the two fluid model, described below, it explains why the AC resistance of a superconductor is not zero. The second London equation is concerned with the Meissner effect, and will not be considered here.

The first London equation can be derived[23] using the Drude model of electronic conduction in a solid. Drude theory[24] assumes that each charge carrier is independent, and interacts with the lattice by scattering from impurities and atoms within the lattice. When an electric field $\boldsymbol{E}$ is applied, the charge carriers are accelerated. However they are also scattered and therefore move with some average velocity, v. The net drag force on each carrier, in analogy with viscous drag, is proportional to the velocity. The net force $\boldsymbol{F}_{net}$ is therefore

$$\boldsymbol{F}_{net} = q\boldsymbol{E} - \frac{m}{\tau_s} v \,, \tag{2.1}$$

where q is the electronic charge, τ_s is the scattering time and m is the mass of the carrier. The scattering time represents the average time between collisions; the more often a charge carrier collides with something, the greater the drag force. Newton's Law, assuming a harmonically varying electric field, is

$$\boldsymbol{F}_{net} = m\frac{dv}{dt} = j\omega m v \,. \tag{2.2}$$

Combining these two equations allows us to solve for the velocity in terms of the electric field:

$$v = \left(\frac{q\tau_s}{m}\right)\frac{1}{1+j\omega\tau_s}E \,. \tag{2.3}$$

The current density J flowing in the material is the sum of the responses from all the carriers. If there are n carriers per unit volume, the current density is $J = nqv$ so the current density can be expressed in terms of the electric field:

$$J = \left(\frac{nq^2\tau_s}{m}\right)\frac{1}{1+j\omega\tau_s}E \,. \tag{2.4}$$

We can now investigate two different limits of this equation. We will see that the two limits correspond to conduction in normal metals and in superconductors, respectively. If the scattering time is short enough so that $\omega\tau_s \ll 1$, Eq. 2.4 simplifies to

$$J = \left(\frac{nq^2\tau_s}{m}\right)E \equiv \sigma E \,. \tag{2.5}$$

This is simply Ohm's Law, stating that the current density is proportional to the electric field, with the electrical conductivity as the constant of proportionality. Ohm's Law is widely used to describe the electrical conduction of metals. For copper at room temperature, the electrical conductivity can be measured, giving an estimate for the scattering time of $\approx 2.5\times10^{-14}$ seconds. This means that for metals, the approximation that $\omega\tau_s \ll 1$ holds for frequencies to the THz range, and Ohm's Law will be frequency independent for essentially all frequencies of interest. In practice this is not exactly true, but it is a good approximation.

The second limit occurs when the scattering time approaches infinity. In this case, Eq. 2.4 simplifies to

$$J = \frac{1}{j\omega}\left(\frac{nq^2}{m}\right)E \,. \tag{2.6}$$

This equation states that in the absence of scattering, the current density will always be 90° out of phase with the applied electric field, and no power will be dissipated by the material.[d]

[d] The work done on each carrier per AC cycle is $W = \int F\cdot dl = \int qE\cdot v\,dt = \frac{q^2E^2}{\omega}\int_0^T \cos\omega t \sin\omega t\,dt = 0$.

This is precisely the situation that occurs for superconductors, and this phenomenological theory can be used to explain many of the electrical properties of superconductors. For example, it states that the conductivity becomes infinite as the frequency approaches zero. Intuitively, this is very reasonable, since a material with a true zero resistance will carry an infinite current for any infinitesimally small applied voltage. This is observed in superconducting materials, since a superconductor can not support a DC voltage. We will show later in this chapter that when a DC voltage is applied to a superconductor, the current increases rapidly until the superconducting state is destroyed, albeit in a special manner. Equation 2.6 also tells us that a superconductor does have an impedance for non-zero frequencies. Since the current density (and hence the current) lags the electric field (and hence the voltage) by 90°, the superconductor is completely analogous to an ideal inductor. This inductance is due solely to the inertia of the charge carriers; an electric field is required to change their velocity. The inductance is therefore called the kinetic inductance. It should be emphasized that all conductors possess kinetic inductance, but in normal metals, the scattering time is so small that the effect is essentially completely suppressed.[c]

2.3. The Two Fluid Model

In Section 2.2 we analyzed the behaviour of a system consisting of charge carriers that are not scattered, and found that the system adequately describes a fully superconducting state. Another important aspect of superconductivity is seen if Ampère's Law is combined with the first London equation to describe the propagation of electromagnetic fields in a superconductor. It can be shown[25] that when an electromagnetic wave is incident on a dielectric superconductor boundary, the fields that penetrate are exponentially attenuated with the distance travelled into the superconductor. The characteristic length, λ_L, over which the field has been reduced to $1/e$ of its initial value is known as the London penetration depth. In

[c] One of Faraday's initial induction experiments was to show that the inductance of a wire was greatly increased when coiled into a helix and was not simply proportional to the length of the wire as one would expect from an inertial mass effect. See M. Faraday, *Experimental Researches in Electricity*, Vol. I, Bernard Quaritch, London, 1839, pp. 330.

the two fluid model, the penetration depth is $\lambda_L = \sqrt{\frac{m}{\mu n q^2}}$, where m is the mass of the superconducting charge carriers, q is their charge, n is their number density, and μ is the permeability. The penetration depth depends only on fundamental material properties and has been measured as a function of temperature using microwave resonator techniques. Initial pioneering work in this field using low temperature superconductors was done by A.B. Pippard.[26] Recent work on $YBa_2Cu_3O_{7-\delta}$ thin films has shown[27,28] that the London penetration depth has approximately a $\left[1-(T/T_C)^2\right]^{-1/2}$ functional dependence[f], with a zero temperature value of between 150 and 270 nm. The penetration depth increases with temperature, going to infinity as T approaches T_C. Since the only parameter in the definition of the penetration depth that can change with temperature is the number density of superconducting charge carriers, n must be temperature dependent. The two fluid model assumes the total number of charge carriers (normal electrons, n_N, plus superconducting charge carriers, n_S) is constant, so there must be a mixture of normal and superconducting electrons present at all temperatures except for at absolute zero. Above T_C, all carriers are normal electrons. Below T_C, some electrons condense into superelectrons, and the fraction of superconducting to normal electrons increases to one as the temperature is reduced to absolute zero.

With the two fluid model and the first London equation, we get a more complete picture of electrical conduction in superconductors. Because there are both normal (lossy) electrons, obeying Ohm's law, and superconducting (lossless) electrons, obeying the London

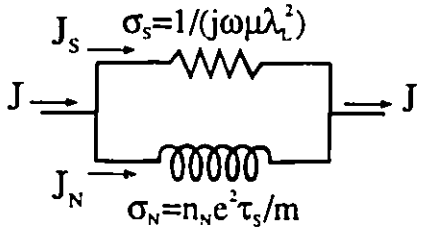

Fig. 2.1. Electrical model of a superconductor. The inductor represents the kinetic inductance of the charge carriers, while the resistor represents losses from the normal state electrons that have not yet condensed into the superconducting state.

[f] This functional dependence highlights another difference between low T_C and high T_C materials. Low T_C materials have a penetration depth that varies approximately as $[1-(T/T_C)^4]^{-1/4}$. This different functional form also causes a different temperature dependence of the superelectron fraction in the two fluid model.

equation, the overall system can be depicted as shown in Fig. 2.1. It is now apparent that a superconductor is only lossless at zero frequency, since the inductor will appear as a perfect short circuit at DC only. At any non-zero frequency, the inductor will have an impedance, so some of the current will be shunted to the resistor and dissipation will occur.

2.4. Microwave Surface Resistance

At low frequencies, the discussion of Section 2.3 is convenient and it gives a good representation of electrical conduction in superconductors. At higher frequencies where we must take the wave nature of the electromagnetic fields into account, we instead use the surface resistance to characterize losses. For any transmission line, the conductive losses are a function of the conductor properties; a material with higher conductivity results in lower losses. However, the losses also depend on the electric field configuration, so conductive losses are also a function of the type of transmission line. The surface resistance is a calculated quantity that takes all of the electrical properties of the conductor into account.[8]

The surface resistance is derived by considering a plane electromagnetic wave normally incident from a dielectric onto a conductor. The wave is partially transmitted into the conductive region, where it is attenuated exponentially, resulting in conductive power losses. A straightforward application of Maxwell's equations shows that[29] the propagation constant in the conductor is

$$\gamma = j\omega\sqrt{\mu\epsilon}\left(1 - \frac{j\sigma}{\omega\epsilon}\right)^{1/2}, \tag{2.7}$$

while the wave impedance describing the ratio of the electric to magnetic field in the conductor is

$$\eta \equiv \frac{E}{H} = \frac{j\omega\mu}{\gamma}. \tag{2.8}$$

[8]For coplanar waveguide transmission lines, Wadell [Ref. 51] gives an expression that can be used to determine conductive losses. The expression is rather complex, but it shows that the losses are given by the surface resistance multiplied by a function depending only on the CPW geometry.

If E and H are in phase, the voltage and current will be in phase, and conductive losses will result. The real part of the wave impedance is therefore associated with the losses in the conductor, and is defined as the surface resistance. Although this derivation has been done for a plane electromagnetic wave, it is also valid for wave propagation in transmission line structures.

For a normal conductor, the conductivity is real and is given by Eq. 2.5. Since $\sigma/\omega\epsilon \gg 1$ for all practical frequencies, the propagation constant and wave impedance are simplified tc

$$\gamma = (1+j)\sqrt{\frac{\omega\mu\sigma}{2}} = \frac{1+j}{\delta} \tag{2.9}$$

and

$$\eta = (1+j)\left(\frac{\omega\mu}{2\sigma}\right)^{1/2}, \tag{2.10}$$

where $\delta = (2/\omega\mu\sigma)^{1/2}$ is known as the skin depth. The skin depth is analogous to the penetration depth in a superconductor, since the electromagnetic fields in a normal metal are attenuated to $1/e$ of their initial value after travelling a distance equal to the skin depth. The surface resistance is the real part of the wave impedance, so it is

$$R_S = \sqrt{\frac{\omega\mu}{2\sigma}} \tag{2.11}$$

This equation shows that in normal metals, the surface resistance increases as the square root of frequency.

Microwave losses in a superconductor can be determined similarly, using the fact that there will be both normal and superconducting electrons present. The conductivity due to the superconducting electrons is given by Eq. 2.6, while the conductivity due to the normal electrons is still given by Eq. 2.5. However, in both cases, the carrier densities must be modified to take the two fluid model into account. The conductivity due to the normal electrons is reduced below T_C because many of them will have condensed into superelectrons.

If we denote the conductivity of the normal electrons below T_C as σ_N and that of the superconducting electrons as σ_S, then the conductivity of the superconductor will be

$$\sigma = \sigma_N + \sigma_S = \sigma_N + \frac{1}{j\omega\mu\lambda_L^2} ,$$

where λ_L has been substituted for the material constants in Eq. 2.6. When this expression is substituted into Eq. 2.8, the wave impedance can be simplified to[h]

$$\eta \approx \frac{\omega^2\mu^2\sigma_N\lambda_L^3}{2} + j\omega\mu\lambda_L . \qquad \textbf{(2.13)}$$

The surface resistance is now[i]

$$R_S = \frac{\omega^2\mu^2\sigma_N\lambda_L^3}{2} , \qquad \textbf{(2.14)}$$

so it increases as the square of the frequency for superconductors, compared with a square root dependence for normal metals. At 1 GHz, the surface resistance of a superconductor at 77K is three orders of magnitude smaller[5] than that of copper at 77K. However, because of the different frequency dependence, losses increase more rapidly with frequency in superconductors than in metals. For $YBa_2Cu_3O_{7-\delta}$, the surface resistance is equal to that of copper at about 200 GHz, so there is no advantage to using it above this frequency range unless the temperature is reduced. Another difference between metallic conductors and superconductors can be seen by comparing their respective wave impedances. In good conductors, the electric and magnetic fields (and hence the electric field and the current) are 45° out of phase with one another. Superconductors show a phase difference of almost 90°, so they appear almost completely reactive.

---

[h] Here the simplification requires $\omega^2\mu\epsilon\lambda^2 \ll 1$ and $\omega\mu\sigma_N\lambda^2 \ll 1$. Both of these conditions are satisfied for frequencies less than 1 THz.

[i] This expression is the theoretical lower bound on the surface resistance; the measured value will also depend on film quality. Only recently have manufacturers been able to approach this limit.

Accurate measurements of the surface resistance of high quality $YBa_2Cu_3O_{7-\delta}$ single crystals have been carried out by Bonn *et al.*[30] They found that the surface resistance at 77K varied as the square of the frequency, as expected. However, they were able to reduce the surface resistance significantly by doping the crystals with zinc. They explained their results by extracting the real part of the conductivity from their microwave measurements. They found that scattering is greatly reduced below T_C. A decrease in the scattering rate results in an increase in the conductivity, which in turn will increase the surface resistance, as is evident in Eq. 2.6. By choosing a dopant which did not significantly affect the superconducting electrons but which did increase the scattering rate of normal state electrons, they were able to decrease the surface resistance by a factor of two. Work is ongoing in various laboratories to try and gain further improvements in the microwave properties of superconductors.

To summarize this section, it is useful to try and get an intuitive picture explaining why superconductors show much lower losses than normal metals. First of all, since the penetration depth is less than the skin depth for frequencies below 50 GHz, electromagnetic fields do not penetrate as far in a superconductor as they do in a normal metal. The field that does penetrate into the superconductor 'sees' only a small number of normal electrons that have not condensed into the superconducting state, and a very large number of superelectrons that are purely reactive. Only the normal electrons contribute to the losses. Having said all of this, we will ignore superconducting losses in the remainder of this thesis. Because we are investigating switching, we are more concerned with putting the superconductor into a highly lossy state. When the device is fully superconducting, the insertion loss will be negligible. As we show below, when the device is in a switched state, superconductivity has been destroyed and the derivation above is no longer relevant.

2.5. DC Biased Superconducting Bridges

We now investigate the DC properties of superconducting microbridges. As discussed in Section 2.2, a superconductor cannot support a DC voltage, since any electric field will result in a current increasing with time to infinity. We are interested in studying switching, so we will investigate the consequences of applying a DC voltage to a superconductor.

Figure 2.2 shows the four-point apparatus used to make all of the DC measurements. To ensure that comparisons between the DC and microwave measurements could be made, the same device was used for each, eliminating film to film variations. Patterning was carried out, as described in Appendix 1, on 1x1 cm $YBa_2Cu_3O_{7-\delta}$ films on 508 μm thick $LaAlO_3$ substrates using a citric acid etch. The Keithley 238 source-measure unit was configured to source voltage (V_{app}) and measure current. A Keithley 182 nanovoltmeter was used to measure the voltage across the bridge (V_b). No external resistor was used for the measurements. The resistor shown in Fig. 2.2 represents the total lead and contact resistance and is typically approximately 1 Ω. Except for resistance versus temperature measurements which were made in vacuum using a probe designed by Steven Moffat, all measurements were made by immersing the device in liquid nitrogen. The data collection was automated using IEEE control of all the apparatus.

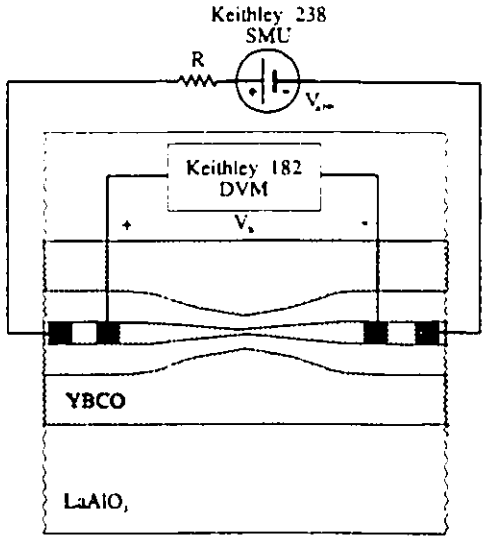

Fig. 2.2. Schematic representation of the DC measurement apparatus. The filled in black squares represent gold contact pads vacuum deposited onto the $YBa_2Cu_3O_{7-\delta}$ film to reduce the contact resistance. Wires were attached to the contact pads with silver paint.

Figure 2.3 shows a typical current versus voltage (I-V) curve. Because the I-V curve is highly non-linear, DC load lines must be used to relate the applied voltage to the measured bridge voltage. The current in the circuit of Fig. 2.2 is $I=\frac{V_{app}-V_b}{R}=-\frac{V_b}{R}+\frac{V_{app}}{R}$ so the load line has a slope of -1/R and intercepts the voltage axis at V_{app}. Three different load lines are depicted in the figure. Load line 1 applies when the applied voltage is $\mathbf{V_1}$. The operating point will be at **A**, and the device will still be in a fully superconducting state. When the applied voltage has increased to $\mathbf{V_2}$, the operating point is **B** and the device is now in the switched state, since the current has been reduced substantially. Load line 3 illustrates why we do not use current biasing. If current biasing is used, load line 3 applies and the device will be forced to operate at point **C**. Device failure is probable because of the high power dissipation.

A key feature to be noted in the DC I-V curve is that once switching has occurred, the current is approximately constant, independent of the bias voltage, so the bridge resistance increases linearly with voltage. Two mechanisms are postulated to explain an increasing resistance with voltage. The temperature of the hotspot could rise, increasing the resistivity. Alternatively, an increasing hotspot length would also give rise to a resistance increase. The hotspot model, discussed in the next chapter, addresses this issue, and it will be shown that the temperature remains constant while the length of the hotspot increases.

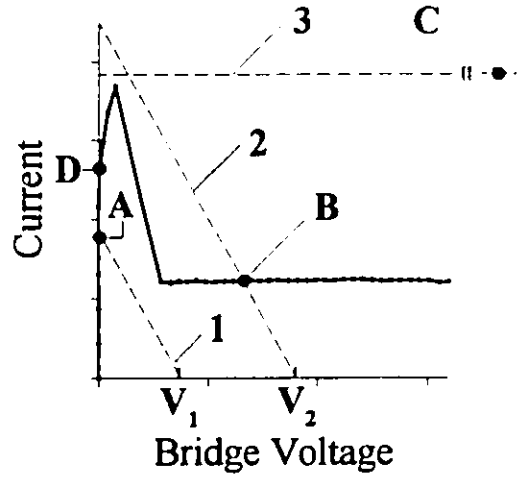

Fig. 2.3. Typical I-V curve for a superconductor. The solid line is the I-V curve, while the dashed lines represent different load lines as discussed in the text.

2.5. Measured I-V Curves for DC Voltage Biased Bridges

In this section, measured I-V curves for two different devices are presented. Both were fabricated using 200 nm thick Conductus $YBa_2Cu_3O_{7-\delta}$ films, with T_C=85K. The first was patterned with a 5 μm wide bridge structure, while the second was patterned with a 10 μm wide bridge structure. Four point DC measurements were made on both devices.

Figures 2.4(a) and 2.5(a) show measured V-I curves for both devices. DC current biasing is used, and the bridge voltage is measured. This measurement is useful for determining the critical current density (J_C) of the films, and also shows the current where switching occurs with the formation of a hotspot. For small currents, the bridge voltage is below the noise floor of the measurement apparatus. However, as the current increases, a measurable voltage eventually appears across the bridge. The critical current density, based on the 1 μV/cm criterion, is 0.9 MA/cm^2 for the 5 μm wide bridge, and 1.1 MA/cm^2 for the 10 μm wide bridge. As the current is increased further, switching is eventually observed, with the formation of a hotspot. It forms at a current of 23 mA (2.3 MA/cm^2) for the 5 μm wide bridge, and at 60 mA (3 MA/cm^2) for the 10 μm wide bridge. Differences in J_C and the thermal switching current indicate non-uniform film properties, varying from device to device.

Figures 2.4(b) and 2.5(b) show measured I-V data for the same devices. This data was measured by applying a DC voltage across the device, and measuring the current. Note that the hotspot forms at the same current as seen in the current biased measurement. The bridge resistance has also been calculated from the I-V data, and is shown on the same figure. It was computed by dividing the bridge voltage by the current. It increases linearly with voltage, reaching a maximum level of 820 Ω and 440 Ω for the 5 μm and 10 μm wide devices, respectively, with a bridge voltage of 10V.

Figures 2.4(c) and 2.5(c) show computed resistance versus power dissipation curves for the two devices, again for voltage biasing, where the voltage varied between 0 and 10 V. The power dissipation was calculated by taking the product of the current and bridge voltage. The narrower bridge results in a higher resistance (820 Ω versus 440 Ω) and a lower power dissipation (125 mW versus 250 mW). Reasons for this behaviour are explored in the next chapter, when a detailed model of the hotspot is developed.

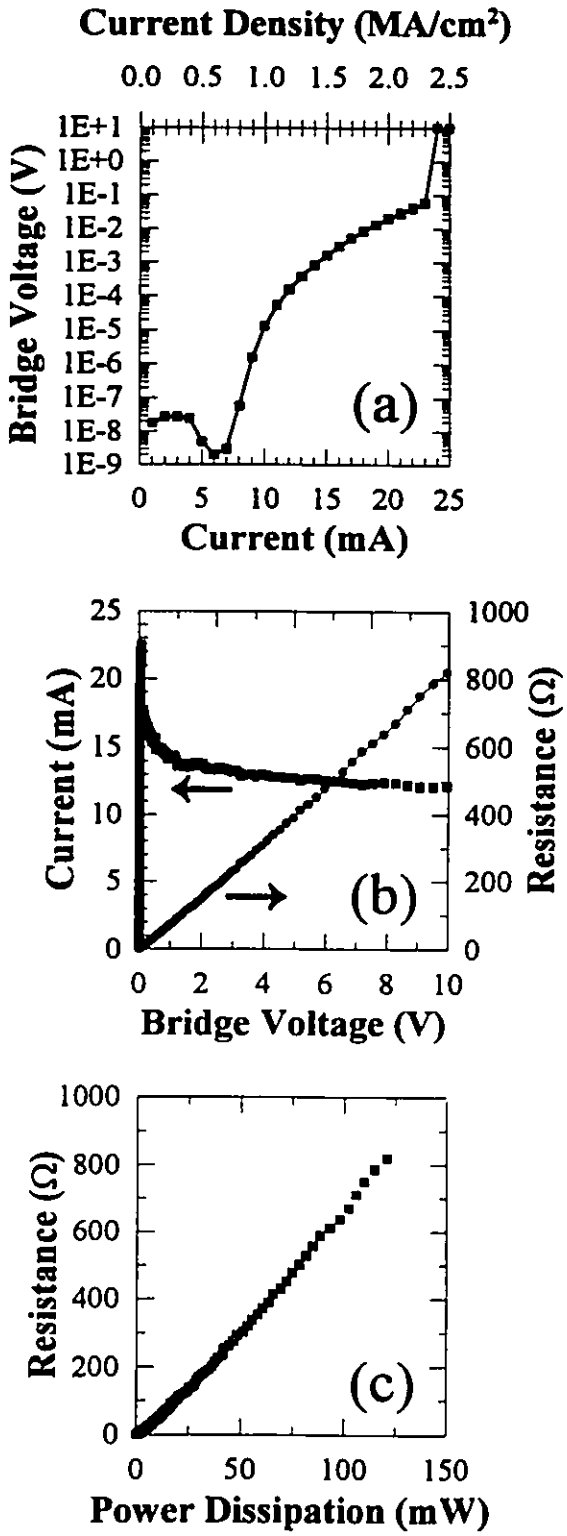

Fig. 2.4. DC measurements on the 5 μm wide bridge.

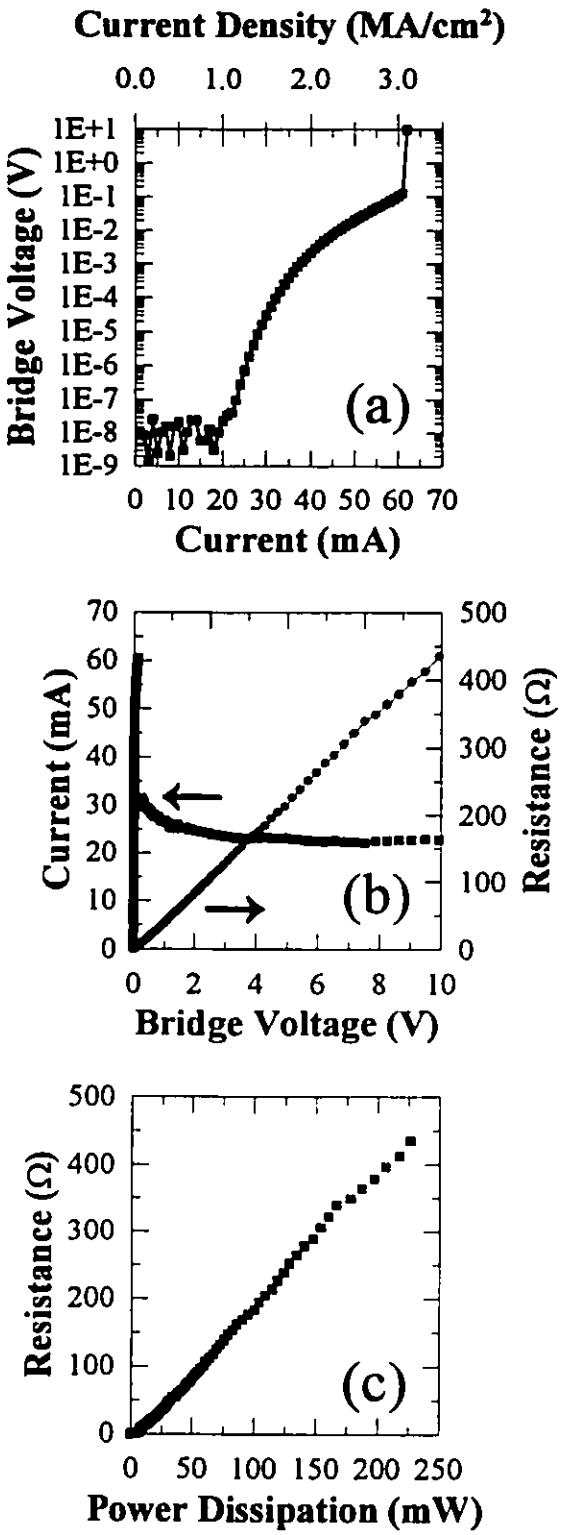

Fig. 2.5. DC measurements on the 10 μm wide bridge.

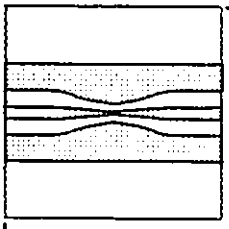

THE HOTSPOT MODEL

3.1. The Hotspot Model

Figure 2.3, repeated in this chapter as Fig. 3.1 shows that large currents can flow with virtually no voltage appearing across a superconducting bridge. However, as the current increases beyond point **D**, losses in the superconductor start to become non-negligible, and a non-zero voltage begins to appear across the bridge. A variety of dissipation mechanisms[31,32,33] involving the motion of vortices have been postulated to explain these losses, and this area is currently an active area of research. For the purpose of this thesis, it suffices to say that when the current has exceeded the critical current density, losses result. Although these losses are important in precipitating switching, their exact origin is of minimal importance here. The result of the loss mechanisms is that power is absorbed by the superconductor, appearing as heat. This heat must be transferred to the cryogen to ensure that the bridge remains in a superconducting state.

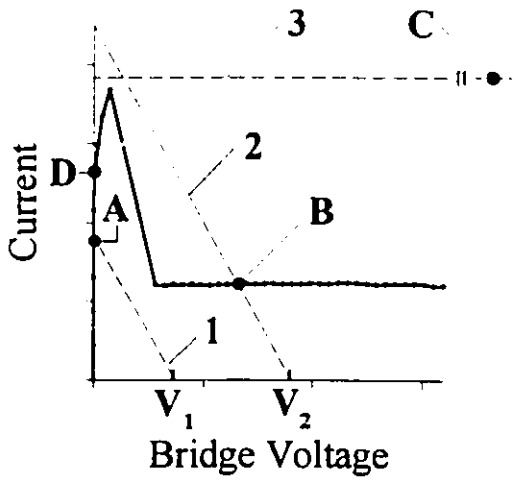

Fig. 3.1. Typical I-V curve for a DC voltage biased superconducting bridge. The dashed lines are DC load lines.

As the applied voltage is further increased, power dissipation also increases. When the rate of power generation exceeds the rate of heat removal by the cryogen, the temperature in a small region of the film increases above T_c and the bridge goes into a switched state due to the formation of a hotspot. The formation of hotspots under current biasing was proposed[34] for low T_c materials as early as 1958, and a complete theory describing their formation was put forth by Skocpol *et al.* in 1974.[35] The following derivation is based on Skocpol's work, modified for high T_c materials.[36] We discovered that there are significant differences between switching in low T_c and high T_c materials, mostly because the resistivity is essentially independent of temperature above T_c for low T_c materials, while it increases linearly with temperature for high T_c materials.

Consider a superconducting bridge of width W, length L, and thickness d, biased so that a hotspot exists as shown in Fig. 3.2. We analyze this structure using a simple one dimensional heat flow model. The hotspot is heated above T_c, so it is resistive. Because of the current flowing in the bridge, Joule heating occurs in the hotspot. This is the only source of heat generation, since the superconductor, defined as the region where $T < T_c$, is assumed to be perfectly lossless with a resistivity of zero. Above T_c, the resistivity is assumed to be a linear function of temperature, $\rho(T) = cT + \rho_0$, where ρ_0 is the zero temperature intercept. We assume that heat conduction[37] occurs along the bridge $[K_N d^2T/dx^2]$ and that each point along the bridge at temperature T(x) is linearly coupled $[\alpha(T-T_b)/d]$ to a bath at temperature

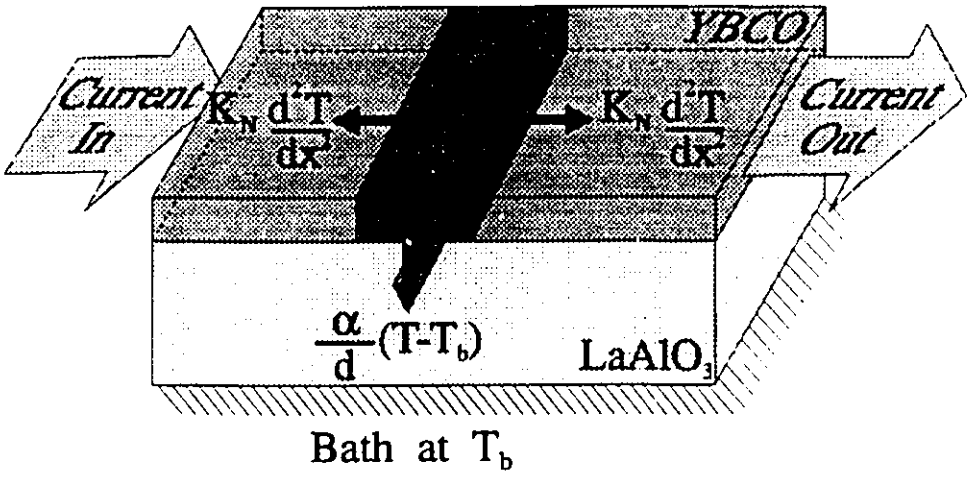

Fig. 3.2. One dimensional model of heat transport in a superconducting bridge biased so that a hotspot is present.

T_b. We look for the steady state solution to the heat flow problem, so the net heat flow out of the hotspot must exactly equal the net heat generated by it. This gives rise to the following one dimensional equations:

$$\begin{aligned} -K_N \frac{d^2T}{dx^2} + \frac{\alpha}{d}(T - T_b) &= \left(\frac{I}{wd}\right)^2 (cT + \rho_0) \qquad [|x| \le x_0] \\ -K_S \frac{d^2T}{dx^2} + \frac{\alpha}{d}(T - T_b) &= 0 \qquad [|x| \ge x_0] \end{aligned} \tag{3.1}$$

where K_N and K_S are the thermal conductivities ($Wcm^{-1}K^{-1}$) of the film in the normal and superconducting state, α is the combined heat transfer coefficient ($Wcm^{-2}K^{-1}$) to the substrate and bath, and I is the electrical current in the bridge. The boundary conditions used to solve these equations are: the temperature at the ends of the bridge must be fixed at the bath temperature [$T(\pm L/2) = T_b$], the temperature at x_0, the interface between the hotspot and superconductor, must equal T_C [$T(\pm x_0) = T_C$], and the heat flow must be continuous at the interface $\left[K_N\left(\frac{dT}{dx}\right) = K_S\left(\frac{dT}{dx}\right) \text{ at } x = \pm x_0\right]$.

The sclution to Eq. 3.1 involves hyperbolic functions. However, by symmetry we know the temperature distribution must be an even function, so the solution has the form

$$\begin{aligned} T_N(x) &= \beta \eta_N^2 + \left(T_C - \beta \eta_N^2\right)\left[\frac{\cosh\left(\frac{x}{\eta_N}\right)}{\cosh\left(\frac{x_0}{\eta_N}\right)}\right] \qquad [|x| \le x_0] \\ T_S(x) &= T_b + (T_C - T_b)\left[\frac{\sinh\left(\frac{L/2 - |x|}{\eta_S}\right)}{\sinh\left(\frac{L/2 - x_0}{\eta_S}\right)}\right] \qquad [|x| \ge x_0] \quad , \end{aligned} \tag{3.2}$$

where

$$\beta = \frac{T_b \alpha W^2 d + \rho_0 I^2}{K_N W^2 d^2}, \quad \eta_S = \sqrt{\frac{K_S d}{\alpha}},$$
$$\text{and } \eta_N = \sqrt{\frac{K_N d}{\alpha}} \left(1 - \frac{c I^2}{\alpha W^2 d} \right)^{-1/2}. \tag{3.3}$$

Equation 3.2 is an exact solution of Eq. 3.1; no approximations were used in getting it to this form. We refer to η_S and η_N as the thermal healing lengths in the superconducting and normal regions, respectively. The reason for this is clear when the temperature distribution is examined. Because of the exponential nature of the hyperbolic functions, the temperature changes rapidly over a length on the order of the thermal healing length. Outside of this region, the temperature is approximately constant. This fact will be apparent later in the chapter when measured and modelled temperature distributions are plotted.

The solution for the temperature distribution involved only the first two boundary conditions. When the final boundary condition is applied to Eq. 3.2, we get an expression that allows us to solve for the current:

$$\left(T_c - \beta \eta_N^2\right) \tanh\left(\frac{x_0}{\eta_N} \right) = - \left(\frac{K_S}{K_N} \right) \left(\frac{\eta_N}{\eta_S} \right) (T_c - T_b) \coth\left(\frac{L/2 - x_0}{\eta_s} \right). \tag{3.4}$$

This transcendental equation must be solved numerically.

The only unknown parameters involved in the solution of Eq. 3.1 are the thermal conductivity in the hotspot (K_N) and superconducting (K_S) regions, the heat transfer coefficient (α), and the length of the hotspot ($2x_0$); all other parameters are measurable quantities. Furthermore, we make the reasonable assumption[38] that the thermal conductivity in the hotspot equals the thermal conductivity in the superconducting region, and is 0.1 $Wcm^{-1}K^{-1}$, so we are left with only two parameters. However, these two parameters are not independent, so there is only one adjustable parameter in the model: the heat transfer coefficient.

To solve these equations, we assume a value for α, and set x_0 to a value where the

hotspot is half the length of the bridge. We then iteratively solve Eq. 3.4 to get a value for the current. We compare this value with the measured current and adjust α until the modelled and measured currents agree, then fix α. At this point, all of the parameters in Eq. 3.1 are known, and we can solve for the temperature distribution. Since the temperature dependence of the resistivity is known, we can now compute the total resistance of the bridge, and therefore the bridge voltage. This gives us one point on the modelled I-V curve. Without changing α, we repeat the procedure for different values of the hotspot length. The current, temperature distribution, and bridge voltage are computed for each different length, and more points are added to the I-V curve.

The solution can be simplified considerably if the zero temperature intercept of the resistivity versus temperature curve, ρ_0, is zero, and if $\eta_N \ll x_0 \ll (L/2 - \eta_S)$. The first assumption is often true for HTS films. The second one is true over a wide range of applied voltages since the thermal healing lengths are on the order of 1 μm, and it will be shown that the hotspot length is a linear function of the applied voltage. In this case, $\beta\eta_N^2 = T_C^2/T_b$, so the temperature at the center of the hotspot is T_C^2/T_b, and the current is

$$I = \sqrt{\frac{\alpha W^2 d}{c}} \left[1 - \frac{T_b^2}{T_C^2} \right]^{1/2} . \qquad \textbf{(3.5)}$$

Still under this same approximation, the voltage across the bridge, neglecting the small voltage drop across the transition region, is given by

$$V = 2x_0 T_C \sqrt{\frac{\alpha c}{d}} \left[\frac{T_C^2}{T_b^2} - 1 \right]^{1/2} . \qquad \textbf{(3.6)}$$

Equations 3.5 and 3.6 are of great use in predicting the effects of various changes on the resistance, power dissipation, and length of the hotspot. This will be discussed further in Section 3.4 on page 34.

3.2. Hotspot Temperature Distribution Measurements

Experiments were performed on 200 nm thick Conductus $YBa_2Cu_3O_{7-\delta}$ films to measure the temperature distribution as a function of the applied bias voltage. These measurements were then compared with theoretical predictions to confirm the modelling.

Temperature measurements were made using a 5x5 mm film patterned as shown in Fig. 3.3. The voltage distribution along the microbridge was measured for different applied bias voltages. The spacing between voltage taps, Δl, was 50 μm, and the taps were made 3 μm wide to minimize thermal perturbations to the bridge under test. The bridge had a length, L, of 450 μm and a width, W, of 10 μm. The DC voltage was applied using a Keithley 238 SMU, while the tap voltages were measured with an eight channel Keithley 199 DVM (for taps one to eight) and a Keithley 182 nanovoltmeter (for tap nine). All voltage measurements were made with respect to tap 10. The current, I, flowing in the bridge was measured using the SMU. A program was written to automate the measurements.

To convert the voltage measurements to temperature, we first measured the resistance versus temperature between taps 1 and 10 and then converted it to resistivity using $\rho(T)=\frac{Wd}{L}R(T)$, where d is the film thickness. A fifth order polynomial was fit to the curve so that the temperature could be determined as a function of resistivity. The measured resistivity versus temperature curve is shown in Fig. 3.4. We then immersed the device in

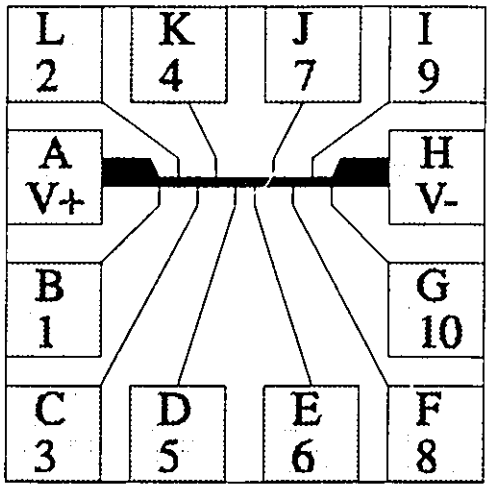

Fig. 3.3. Device used for hotspot temperature measurements. A DC voltage was applied between pads **A** and **H**, and the remaining 10 pads were used to measure the voltage distribution along the bridge.

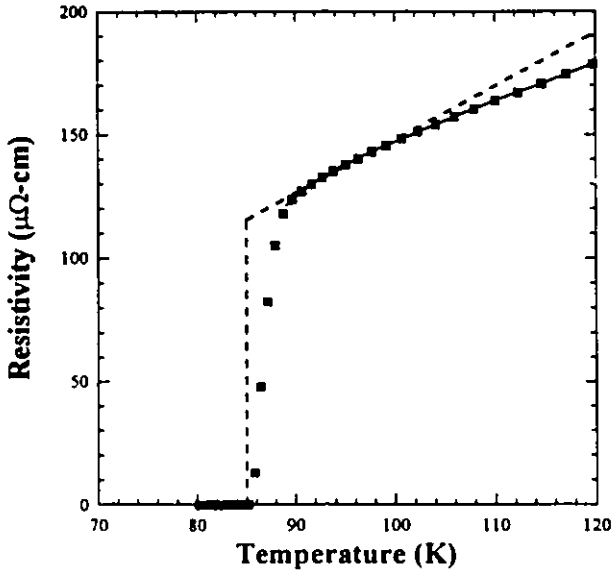

Fig. 3.4. Resistivity versus temperature used for computing hotspot temperature as a function of position. The data points are measured values. The solid line is a fifth order polynomial fit, fit between 89 and 120K. The dashed line is a linear interpolation used in the hotspot model, fit using data between 90 and 100K. It has a slope of c=2.164 μΩ-cm/K and a zero temperature intercept of ρ_0=-68.188 μΩ-cm.

liquid nitrogen, and measured the voltage V between each tap and the current I for different applied bias voltages. These were converted to resistivity using $\rho = \frac{V}{I}\frac{Wd}{\Delta l}$. The bridge voltage was also measured; it is the voltage between taps 1 and 10. In this manner, the average temperature between adjacent taps was measured as a function of the bridge voltage.

The measured tap voltage as a function of position is shown in Fig. 3.5, and the data has been converted to temperature versus position in Fig. 3.6. Although theory predicts that the hotspot should form right at the center of the bridge, in fact it has formed at one end, presumably where the bridge is narrowest or superconductivity is depressed. The small variations in the measured temperature across the hot spot are likely due to processing limitations; the width of the bridge typically varies by approximately 10 percent. Note that for all bias voltages shown, the temperature of the hotspot remains constant, and only its length changes. Furthermore, its length grows very nearly linearly with the bridge voltage, as shown in Fig. 3.7. Finally, Fig. 3.8 shows the measured I-V curve for this device. Note that the current is not constant, but decreases slightly as the voltage increases.

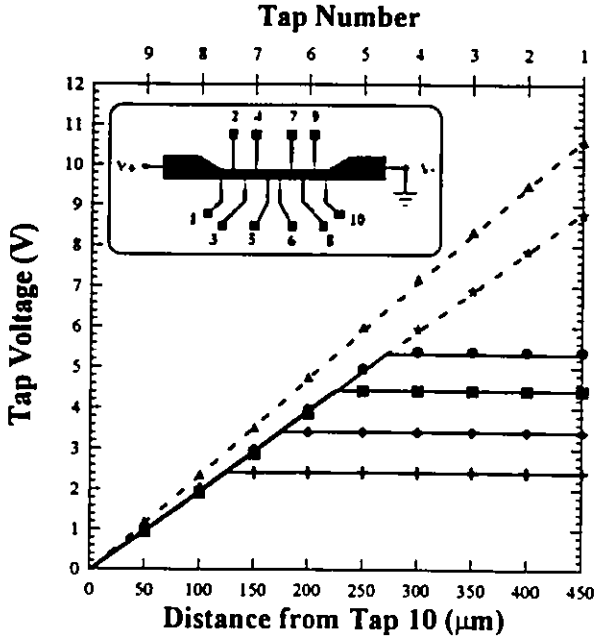

Fig. 3.5. Measured tap voltage as a function of position for bridge voltages of 2.4 (✚), 3.4(◆), 4.4(■), 5.4(●), 8.8(★), and 10.6(▲) Volts. The solid lines are determined from the thermal model. Since the model is only valid when the hotspot length is less than the length of the bridge, modelled results are not shown for the two largest voltages. The dashed lines are linear fits to the data, and are meant only as guides to the eye.

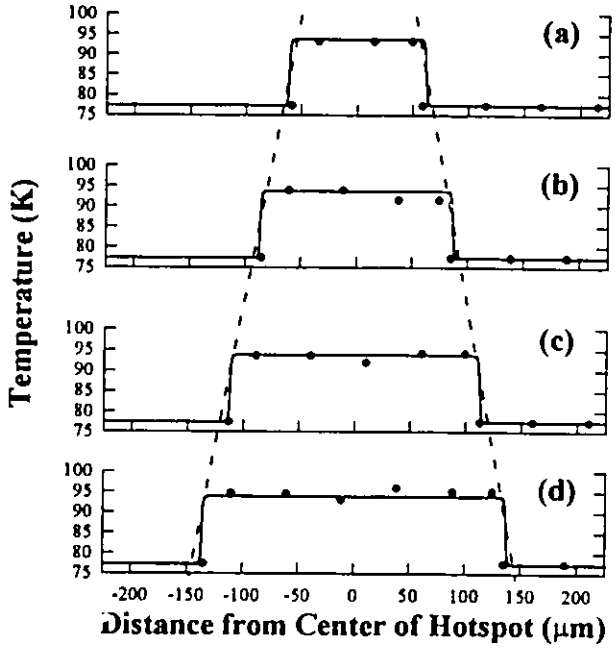

Fig. 3.6. Temperature as a function of position along the bridge for bridge voltages of (a) 2.4, (b) 3.4, (c) 4.4, and (d) 5.4 Volts. The data points are computed temperatures from Fig. 3.5, while the solid lines are calculated from the thermal model. The temperature remains constant at 94K for all voltages.

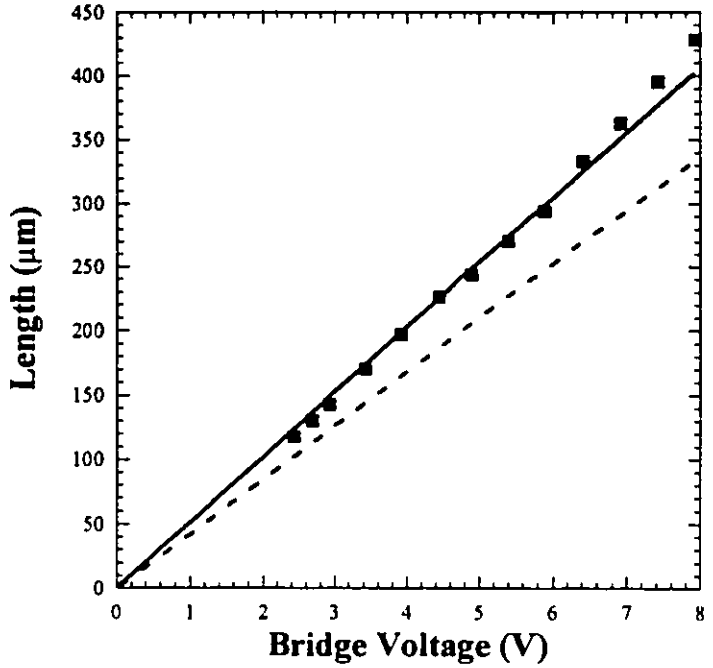

Fig. 3.7. Hotspot length as a function of bridge voltage. The data points are computed lengths from Fig. 3.6, while the solid line is computed from the thermal model. The dashed line is calculated from the simplified expression, Eq. 3.6.

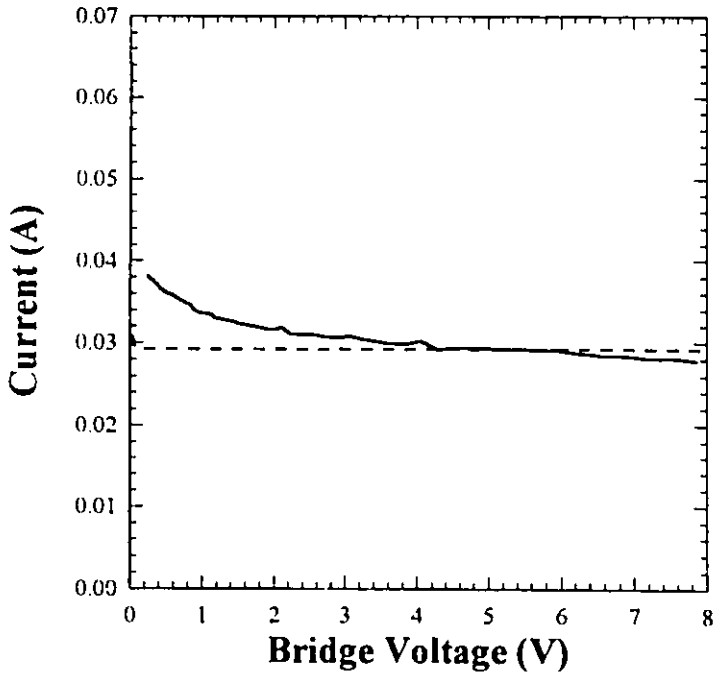

Fig. 3.8. I-V curve for the DC voltage biased bridge. The solid line shows the measured I-V curve, while the dotted line shows the predicted I-V curve based on the thermal model.

3.3. Hotspot Modelling Results

In order to confirm that the hotspot theory discussed above correctly describes the behaviour of a superconducting bridge biased with a DC voltage, a comparison was made between theoretical predictions based on the hotspot model and the actual measurements of the temperature distribution and I-V curve.

The first step was to determine the values for the slope c and intercept ρ_0 of the ρ-T curve. Since we had already measured the temperature of the hot spot and knew that it was approximately 95K, we did a linear least squares fit to the measured data centered at 95K. The fit is shown in Fig. 3.4. Note that the measured ρ-T curve is non-linear, especially close to T_C, but the straight line fit is quite accurate between 90 and 100K. Other known values were also inserted into the model at this time: L=450 μm, d=200 nm, T_C=85K, T_b=77.4K, W=10 μm, and the thermal conductivities of the normal and superconducting material were both set at 1×10^{-5} $Wcm^{-1}K^{-1}$.

We next determined an appropriate value for the thermal heat transfer coefficient, α. To do this, we wanted to ensure that we were in a regime where the model predicted the current was constant. The thermal model predicts that the current will increase both when the hotspot is very small, and when it has almost filled the entire length of the bridge. We therefore chose an intermediate hotspot length to determine α. Since the bridge had an overall length of 450 μm, we set x_0 to 112.5 μm so that the hotspot filled half the bridge, and adjusted the heat transfer coefficient until the modelled current and voltage agreed with measured values. It was found that α=350 $Wcm^{-2}K^{-1}$ gave good agreement with the data, and is in good agreement with measured values.[39] This value was then fixed, and the temperature distribution, current, and voltage were determined for a range of values of x_0.

Figures 3.5, 3.6, 3.7, and 3.8 show that the agreement between measured and modelled results is quite good. Figure 3.5 shows that for voltages less than 8.8V, our model predicts that the length of the hotspot will be proportional to the voltage, since the temperature is independent of the voltage and is approximately T_C^2/T_b. Note that the total voltage drop predicted from the thermal model agrees well with the measured bridge voltage even though we have approximated the ρ-T curve with a step function. Given the current

flowing in the bridge, the transition will be significantly broadened. However, since the thermal healing lengths are much smaller than the length of the hotspot, this leads to negligible differences in the total bridge voltage. Beyond 8.8V, the entire bridge is heated, and the hotspot model is no longer applicable. The temperature is still uniform along the bridge, and now increases with increasing voltage. For the bridge voltage of 10.6V, we obtain a temperature of 105K from the slope of the fitted straight line.

Figure 3.6 shows the excellent agreement between the temperature distribution determined from Fig. 3.5 and the modelled temperature distribution. The temperature is flat-topped, and independent of the applied voltage. The endpoints of the measured hotspot temperature profile were determined by assuming a very narrow transition, and extrapolating the constant slope hotspot regions of Fig. 3.5 to find the intersection with the superconducting regions.

Figure 3.7 shows a small discrepancy for large bridge voltages, when the hotspot length is comparable to the bridge length. This occurs only for large voltages because the temperature at the ends of the bridge can no longer be assumed to be fixed at the bath temperature. Also, note that our measurements are limited to hotspots longer than about 100 μm because our tap spacing is 50 μm. The simple approximation for the hotspot length, Eq. 3.6, is also shown in this figure. It underestimates the hotspot length because for this film, the zero temperature resistivity intercept, ρ_0, is not zero.

The only significant discrepancy occurs in Fig. 3.8 , where the model predicts that the current should be constant except for at very small bridge voltages. In reality, the current is a monotonically decreasing function of the voltage, and diverges from model predictions below 2V. The modelled I-V curve can be broadened by increasing K_N and K_S, but the increases required to broaden the transition significantly are unphysical. We believe the disparity between modelled and measured results are caused by variations of the effective value of the heat transfer coefficient. In our model, α is constant. However, it likely decreases as the hotspot grows, with lateral heat diffusion in the substrate near the ends of the hotspot becoming less important. We chose to treat α as a constant, since varying it to achieve a better fit to the I-V curve would not add any significant insight to the problem. More exact

modelling would require a full three dimensional solution of the thermal transport which has not been attempted.

3.4. Optimizing Device Performance

Equations 3.5 and 3.6 on page 27 can be used as an aid in predicting which parameters should be changed to increase the device resistance and/or decrease the power dissipation. Although these equations are only exact when the zero temperature intercept of the ρ-T curve is zero and over a limited range of applied voltages, they are good approximations of the current and bridge voltage even when these conditions are not exactly met, and certainly can be used to predict overall trends in device performance.

The bridge resistance, $R=V/I$, is simply the quotient of these equations, while the power dissipation, $P=IV$, is given by their product. Since we are interested in looking at the resistance and power dissipation as a function of bridge voltage, we first express the hotspot length in terms of the voltage using Eq. 3.6:

$$x_0 = \frac{V}{2T_C}\sqrt{\frac{d}{\alpha c}}\frac{T_b}{\sqrt{T_C^2 - T_b^2}} \qquad (3.7)$$

We next substitute this into the expressions for resistance and power dissipation to get:

$$R = \frac{V}{I} = 2x_o\frac{T_C^2}{T_b}\frac{c}{dW} = \frac{V}{W}\sqrt{\frac{c}{\alpha d}}\frac{T_C}{\sqrt{T_C^2 - T_b^2}}$$

$$P = IV = 2x_0\alpha W\left(\frac{T_C^2 - T_b^2}{T_b}\right) = VW\sqrt{\frac{\alpha d}{c}}\frac{\sqrt{T_C^2 - T_b^2}}{T_C} \qquad (3.8)$$

We can use these equations to predict general trends in device performance. These trends are summarized in Table 3.1. We have already seen that increasing the voltage results in a linear increase in the bridge resistance. However, it also causes a linear increase in the

Action	Effect on Hotspot Length	Effect on Bridge Resistance	Effect on Power Dissipation
Increase the voltage, V	Increases linearly	Increases linearly	Increases linearly
Decrease the line width, W	No effect	Increases linearly	Decreases linearly
Decrease film thickness, d	Decreases	Increases	Decreases
Decrease the heat transfer coefficient, α	Increases	Increases	Decreases
Increase bath temperature, T_b	Increases	Increases	Decreases

Table 3.2. Effects of various changes on hotspot length, resistance, and power dissipation.

power dissipation. Clearly the most effective technique to improve the performance of the device will be to decrease the width of the bridge and/or to decrease the film thickness, since both of these techniques will result in larger resistance and decreased power dissipation for the same applied voltage. Decreasing the film thickness has another advantage. Since the length of the hotspot decreases, it will be possible to bias the bridge with higher voltages before it is completely saturated, so even larger resistance values will be possible. Of course both of these changes will reduce the microwave power handling capacity of the device if it is used as a microwave switch. Other changes, including increasing the bath temperature or modifying the heat transfer coefficient (perhaps by mounting the device on a cold finger in vacuum) will also increase the resistance of the device, although they do so sub-linearly and cause an increase in the hotspot length and power dissipation. Although not addressed in this thesis, ion irradiation has been shown[40] to increase the normal state resistivity of HTS films, so it can also be used to increase the resistance of the device in the switched state.

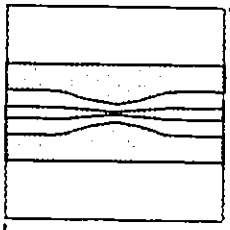

MICROWAVE THEORY

4.1. Microwave Engineering

The term *microwave* refers to electromagnetic signals with frequencies between 300 MHz and 300 GHz. Microwave engineering is concerned with designing and building circuits used in this frequency range. Because of the high frequencies, the wavelength of the electrical signal is relatively short, varying from about 1 mm to 1 m, and standard circuit theory cannot be used to solve microwave network problems. This can be demonstrated[41] by considering a simple circuit consisting of a voltage source and a series resistor, as shown in Fig. 4.1. Basic circuit theory allows us to solve for the electrical current flowing in the circuit at low frequencies using Kirchoff's law giving $V_0(t) - RI(t) = 0$. To illustrate how standard circuit theory breaks down at higher frequencies, we derive Kirchoff's Law directly from Maxwell's equations.

We begin by applying Faraday's law to this circuit, $\nabla \times \boldsymbol{E} = -\frac{\partial \boldsymbol{B}}{\partial t}$. Applying Stoke's theorem allows us to write this as

$$\oint \boldsymbol{E} \cdot d\boldsymbol{l} = -\frac{d}{dt} \iint \boldsymbol{B} \cdot d\boldsymbol{S} \quad , \tag{4.1}$$

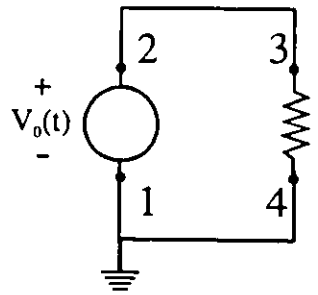

Fig. 4.1. Series circuit with resistor used to derive Kirchoff's Law.

where the electric field is integrated around the entire circuit [the path is 1-2-3-4-1] and defines the boundary of the surface S. The loop integral of the electric field can be broken down into only two components, since the connecting wires are assumed to be good conductors, and the equation becomes

$$-\int_1^2 \boldsymbol{E}\cdot d\boldsymbol{l} - \int_3^4 \boldsymbol{E}\cdot d\boldsymbol{l} = \frac{d}{dt}\iint \boldsymbol{B}\cdot d\boldsymbol{S} \quad . \tag{4.2}$$

The first term on the left hand side of the equation is the voltage supplied by the voltage generator, while the second term is the potential difference across the resistor. We can immediately see that this expression is not equivalent to the expression resulting from Kirchoff's law due to the non-zero term on the right hand side of the equation. However, we recognize that this term is the contribution to the EMF due to the rate of change of magnetic flux in the circuit. If this contribution is not negligible, its effect can be accounted for by adding an inductor to the circuit, and Kirchoff's law still holds.[j] For the remainder of this section, we will assume that this EMF is negligible.[k] To evaluate the second term on the left hand side of the integral, we invoke Ohm's law, $\boldsymbol{J} = \sigma\boldsymbol{E}$. If the current is uniformly distributed over the cross sectional area A of the resistor, the current density is $\boldsymbol{J} = \boldsymbol{I}/\mathrm{A}$. We substitute this into the integral to get

$$-V_0 + \int_3^4 \frac{\boldsymbol{I}}{\sigma A}\cdot d\boldsymbol{l} = 0 \quad . \tag{4.3}$$

---

[j] The inductance L of a circuit loop is defined as the ratio of the magnetic flux linking the loop to the current flowing within it, so the right hand side of the equation can be written as $\frac{d}{dt}[LI]$ or, assuming the inductance is independent of time, $L\frac{dI}{dt}$.

[k] The right hand side is precisely zero only at DC. The term becomes more important as the frequency is increased, necessitating the use of a series inductance for more accurate circuit modelling.

If the current is constant along the entire length of the resistor, this equation simplifies to

$$-V_0 + \frac{I}{\sigma A}\int_3^4 dl = -V_0 + \frac{l}{\sigma A} I = -V_0 + RI = 0 \quad . \tag{4.4}$$

This is the same result one obtains from standard low frequency circuit theory.

At higher frequencies when the wavelength becomes comparable to the physical length of the device, the current is no longer constant across the entire length of the resistor. This is the essence of microwave engineering, with the size of the device becoming a significant fraction of the electrical wavelength. There are also other effects that become important at higher frequencies. The current distribution within the resistor will change, becoming non-uniform over the cross section. Secondly, the connecting wires will have a significant electrical length, and stray inductances and capacitances will become much more important. In fact, as we will see in the next section, the inductance and capacitance of the "wires" are precisely controlled in microwave transmission lines so that electrical signals can be efficiently transmitted.

Because circuit theory is well understood and allows us to analyze circuits without having to resort to using Maxwell's equations, one would like to use it in microwave engineering. Transmission line theory, to be discussed in the next section, gives us a way to do this. We will see that we can continue to use circuit theory by employing distributed rather than discrete components.

4.2. Transmission Line Theory

Transmission lines are structures designed to distribute microwave power from one point to another. Coaxial cable is one of the most common types of transmission lines, as it is widely used for the transmission of cable television signals. However, because the signal conductor is completely enclosed, it is inaccessible making it very difficult to use coaxial cable for microwave integrated circuits. The majority of microwave circuits are fabricated using planar transmission lines. Figure 4.2 shows a summary of some of the most common types

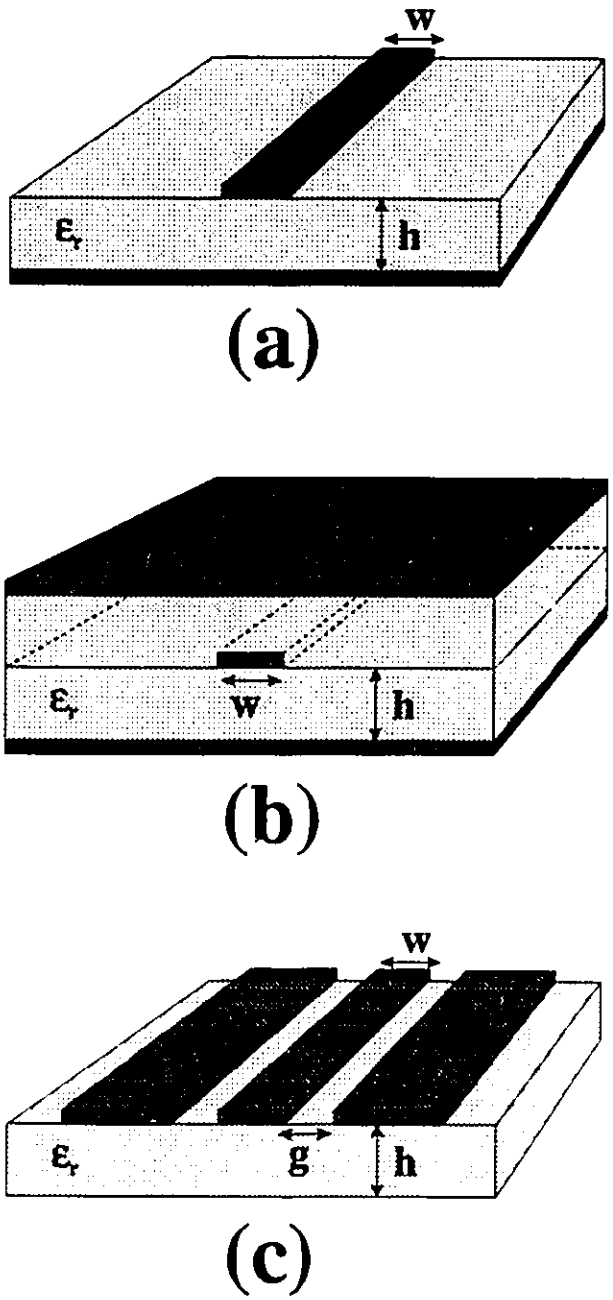

Fig. 4.2. Three of the most common types of microwave transmission lines. Fig. (a) shows a microstrip line in which a narrow signal conductor of width w is on the top surface of a dielectric of thickness h and dielectric constant ϵ_r. A ground plane completely covers the bottom surface of the dielectric. The characteristic impedance is a function of w, h, and ϵ_r. Fig. (b) is a stripline transmission line in which the signal conductor of width w is completely enclosed by dielectric material of height $2h$. The characteristic impedance is again a function of w, h, and ϵ_r. Fig. (c) shows a coplanar waveguide transmission line having a central signal conductor of width w and two adjacent ground planes separated from the signal conductor by an amount g. The dielectric has a thickness h. The characteristic impedance is a function of w, g, and ϵ_r. If a conductor is added to the back surface, the structure is a conductor backed coplanar waveguide (CBCPW), and the impedance is a function of w, g, h, and ϵ_r.

of planar lines. Microstrip is probably the most widely used since it is easy to fabricate and allows for straightforward integration with other components. Stripline was widely used in the past, although its use is in decline because of integration difficulties. Its main advantage is that it offers a pure TEM propagation mode, and, because the electromagnetic signal is totally confined within a single dielectric medium, dispersion is eliminated.[1] Coplanar waveguide (CPW) is now quite widely used, especially in applications involving active circuitry. Its main advantage is that the ground planes are very easily accessible, so that ground connections are available without having to use vias. A further advantage is that the characteristic impedance of CPW is a function of both the width of the center conductor and the gap between the center conductor and the adjacent ground planes. This is attractive in applications where it is desirable to change the width of the center conductor without altering the characteristic impedance of the transmission line. For example, microwave integrated circuits consist of a series of microwave devices connected with a transmission line. CPW can be used to match the line width to the variable component lead widths while keeping the characteristic impedance constant.

Transmission line theory offers a powerful technique to analyze microwave circuits. In essence, it treats a transmission line as an electrical circuit having distributed impedances. The model most widely used is shown in Fig. 4.3. The series inductance is due to the total inductance of the two conductors, including both self inductance and kinetic inductance. The series resistance represents resistive losses in the transmission line due to the finite conductivity of the conductors. The shunt conductance represents dielectric loss in the material between the conductors.

We wish to derive an expression that describes the propagation of travelling voltage and current waves along the transmission line. We restrict the analysis to TEM modes so we

---

[1] Because the field is confined to a single dielectric, all frequencies propagate in an identical dielectric environment so that geometric dispersion is eliminated in stripline. The intrinsic material dispersion of the dielectric is still present. In microstrip and coplanar waveguide, the field is present in two different dielectrics, and it becomes more concentrated in the higher dielectric constant material at higher frequencies. This results in a frequency dependence of the effective dielectric constant and dispersion results. This argument is only valid for TEM (or quasi TEM) propagation modes. Higher order TE or TM modes will exhibit dispersion in all types of transmission lines.

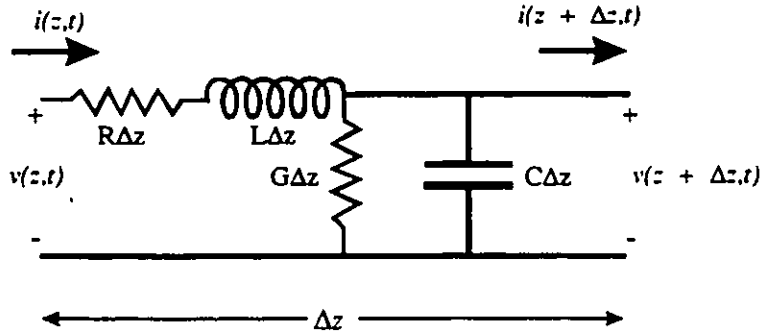

Fig. 4.3. An incremental section of a transmission line of length Δz having an inductance per unit length L, a capacitance per unit length C, a series resistance per unit length R and a shunt conductance per unit length G.

can define a unique voltage and current.[42] We use standard circuit theory to analyze the incremental section shown in Fig. 4.3, then cascade many sections together to treat a finite line length. We begin by applying Kirchoff's voltage and current laws to get

$$\begin{aligned} v(z,t) - R\Delta z\, i(z,t) - L\Delta z \frac{\partial i(z,t)}{\partial t} - v(z + \Delta z,t) &= 0 \\ i(z,t) - G\Delta z\, v(z + \Delta z,t) - C\Delta z \frac{\partial v(z + \Delta z,t)}{\partial t} - i(z + \Delta z,t) &= 0 \,. \end{aligned} \tag{4.5}$$

In these equations, v and I represent the total voltage and current, respectively, and include time dependence. Because we are analyzing an incremental section of the transmission line, its length is much smaller than the wavelength, and Kirchoff's laws are valid. Dividing these equations and taking the limit as $\Delta z \to 0$ gives us the following set of coupled differential equations:

$$\begin{aligned} \frac{\partial v(z,t)}{\partial z} &= - Ri(z,t) - L\frac{\partial i(z,t)}{\partial t} \\ \frac{\partial i(z,t)}{\partial z} &= - Gv(z,t) - C\frac{\partial v(z,t)}{\partial t} \,. \end{aligned} \tag{4.6}$$

These equations are valid for arbitrary time dependence. All of the work in this thesis involves fields having a sinusoidal time dependence. For the sinusoidal steady state, these equations simplify to:

$$\frac{dV(z)}{dz} = -(R + j\omega L)\, I(z)$$
$$\frac{dI(z)}{dz} = -(G + j\omega C)\, V(z)\,, \tag{4.7}$$

where V and I are phasors that contain magnitude and phase information for each specific frequency ω. These equations are solved simultaneously to yield wave equations for the voltage and the current. Taking the derivative of the top equation, then substituting dI/dz from the lower one gives

$$\frac{d^2V(z)}{dz^2} - \gamma^2 V(z) = 0$$
$$\frac{d^2I(z)}{dz^2} - \gamma^2 I(z) = 0 \tag{4.8}$$

where $\gamma = \alpha + j\beta = \sqrt{(R + j\omega L)(G + j\omega C)}$.

Equations 4.8 can now be solved independently to get expressions for the voltage and current. The travelling wave solutions are given by

$$V(z) = V_0^+ e^{-\gamma z} + V_0^- e^{\gamma z}$$
$$I(z) = \frac{\gamma}{R + j\omega L}\left[V_0^+ e^{-\gamma z} - V_0^- e^{\gamma z}\right]. \tag{4.9}$$

This is the most general solution of Eq. 4.6, yielding expressions for the voltage and current at different positions along the transmission line in terms of its fundamental physical properties. Both the voltage and current comprise a forward and backward travelling wave. The complex propagation constant, γ, gives us the attenuation coefficient (α) and the wavenumber (β). The prefactors in front of the exponentials give the magnitude and phase

of the forward or negative travelling component. For example, V_o^+ represents the forward travelling component of the voltage wave. In Eq. 4.9, we use complex exponentials to describe the wave propagation, since they greatly simplify the analysis. The actual wave is given by the real part of the equation only, since electromagnetic waves are measurable quantities. Since we are using phasors to represent the wave, we have omitted the $e^{j\omega t}$ term that describes the time dependence of the wave for convenience. To clarify these points, the actual voltage wave represented by Eq. 4.9 is given by

$$v(z,t) = \left|V_0^+\right| e^{-\alpha z}\cos(\beta z - \omega t + \phi^+) + \left|V_0^-\right| e^{\alpha z}\cos(\beta z + \omega t + \phi^-) \qquad (4.10)$$

where ϕ^+ and ϕ^- are the initial phases of the forward and backward travelling waves.

The ratio of the forward travelling voltage wave to the forward travelling current wave is known as the characteristic impedance of the transmission line. From Eqs. 4.8 and 4.9, the characteristic impedance is

$$Z_0 \equiv \frac{V_0^+}{I_0^+} = \frac{R + j\omega L}{\gamma} = \sqrt{\frac{R + j\omega L}{G + j\omega C}} \qquad (4.11)$$

Unless the transmission line is lossless ($R=G=0$), the characteristic impedance will be complex so that the voltage and current will not be in phase. Most low loss transmission lines are approximated as lossless with a characteristic impedance of

$$Z_0 = \sqrt{\frac{L}{C}} \qquad (4.12)$$

and a purely imaginary propagation constant of

$$\gamma = \alpha + j\beta = j\omega\sqrt{LC} \qquad (4.13)$$

so that the attenuation coefficient α is zero and the phase velocity is $v_p = \frac{\omega}{\beta} = \frac{1}{\sqrt{LC}}$.

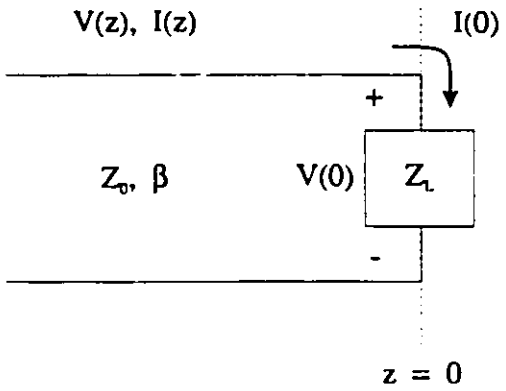

Fig. 4.4. A transmission line terminated in an arbitrary load impedance Z_L. The voltage and current will be reflected at the load to ensure that $V/I = Z_L$ at $z = 0$. The reflection results in the presence of a standing wave on the line.

The concept of characteristic impedance is important in the design of microwave circuits and transmission lines. To understand why, we investigate the propagation of a wave along a lossless transmission line terminated in an arbitrary load impedance. Unless the load impedance is equal to the characteristic impedance of the transmission line, we will see that a fraction of the incident power will be reflected by the load, and not all the incident power will be transmitted.

Consider a lossless transmission line of characteristic impedance Z_0, length l, and wavenumber β terminated in an impedance Z_L as shown in Fig. 4.4. The total voltage and current at any point z along the line will be made up of the incident and reflected components, given by

$$V(z) = V_0^+ e^{-j\beta z} + V_0^- e^{j\beta z}$$

$$I(z) = \frac{V_0^+}{Z_0} e^{-j\beta z} - \frac{V_0^-}{Z_0} e^{j\beta z} \qquad \textbf{(4.14)}$$

Since the impedance of the load, Z_L, is fixed, the ratio of the total voltage to the total current must equal Z_L at $z = 0$. When this condition is imposed, we get an expression for the reflected voltage wave in terms of the impedance mismatch and the incident wave. The reflection coefficient, Γ, is the ratio of the reflected to the incident voltage wave:

$$\Gamma \equiv \frac{V_0^-}{V_0^+} = \frac{Z_L - Z_0}{Z_L + Z_0} \quad . \tag{4.15}$$

Clearly there will be a reflected component of the voltage if the load impedance is not matched to the characteristic impedance of the transmission line. Greater mismatches give rise to larger reflected components. Note that terminating the transmission line in a short circuit ($Z_L = 0$) gives a reflection coefficient of -1 so that the voltage is completely reflected with a 180° phase shift. When the line is terminated in an open circuit ($Z_L = \infty$), the reflection coefficient is +1 so the voltage is completely reflected with no phase shift. The average power flowing along the line is[43]

$$P_{average} = \frac{1}{2} Re[V(z)I(z)^*] = \frac{1}{2} \frac{\left|V_0^+\right|^2}{Z_0} \left(1 - |\Gamma|^2\right) \quad . \tag{4.16}$$

Equation 4.16 shows that the time averaged power flow is constant at any position along the transmission line. More importantly, reflections reduce the power delivered to the load. No power can be delivered to an open or short circuit. All the power is delivered to the load only when the reflection coefficient is zero.

The analysis so far has concentrated on the effect of a transmission line terminated in a fixed load impedance, and we have seen that unless the load is matched to the line, the voltage and current will be partially reflected. This conclusion also applies to transmission lines with impedance discontinuities. Whenever an impedance mismatch is encountered, partial reflection and partial transmission of the signal will occur, with the reflection coefficient given by Eq. 4.15.[m]

[m] Strictly speaking, this statement is only true if the impedance mismatch does not involve any geometric changes, for example if the impedance change is due only to a change in the dielectric constant. When there is a geometric discontinuity in a transmission line, the characteristic impedance will change, but there will also be additional reflections due to geometric mismatch. This geometric mismatch can be modelled using lumped element inductors and capacitors if high precision is required. Fairly

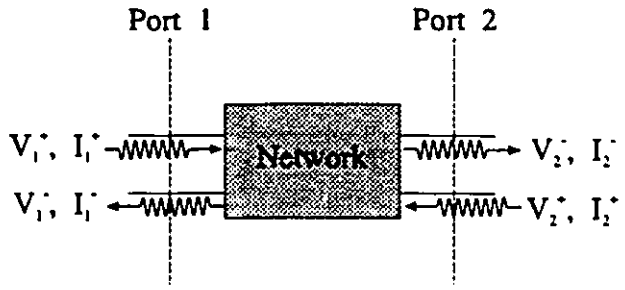

Fig. 4.5. A two port network.

4.3. Scattering Parameters

Scattering parameters[44] (S parameters) are routinely used to characterize the performance of a microwave network. While S parameters can be used for N-port networks, only two port networks as shown in Fig. 4.5 will be discussed here, since the microwave switch investigated in this thesis is a two port network. In addition, we assume that both ports are connected to a 50 Ω transmission line, so we do not need to consider generalized S parameters. The scattering matrix is defined to give a relation between the incident and reflected voltage waves, as shown below:

$$\begin{bmatrix} V_1^- \\ V_2^- \end{bmatrix} = \begin{bmatrix} S_{11} & S_{12} \\ S_{21} & S_{22} \end{bmatrix} \begin{bmatrix} V_1^+ \\ V_2^+ \end{bmatrix} \quad . \tag{4.17}$$

Equation 4.17 tells us that the voltage travelling outwards on port 1, V_1^-, is S_{11} times the incident wave on port 1 plus S_{21} times the incident wave on port 2. Note that S_{11} is the reflection coefficient at port 1 only when there is no incident wave on port 2. This means that one will only measure the true reflection coefficient when port 2 is terminated in a matched load. Similarly, S_{21} is the transmission coefficient only when port 1 is terminated in a matched load. S_{11} and S_{21} are also complex quantities, carrying both magnitude and phase information.

---

accurate models of Microstrip discontinuities that are valid over a limited range of frequencies and dielectric constants exist. However, there are still relatively few accurate models for CPW discontinuities. See, for example, T.C. Edwards, *Foundations for Microwave Circuit Design*, Wiley, New York, 1981.

In working with attenuator or switch applications, the attenuation is an important parameter. The total attenuation is

$$A_{TOTAL} = -10\log_{10}|S_{21}|^2 \quad . \tag{4.18}$$

One can use S parameters to determine how much of the attenuation is due to reflection, and how much is due to absorption.[45] If the power incident on the network is P_I, the power reflected from it is P_R, the power absorbed is P_A, and the power transmitted is P_T, then the fraction of incident power reflected is P_R/P_I and the fraction of incident power transmitted is P_T/P_I. The remainder of the power is absorbed. Since $P_R/P_I = |S_{11}|^2$, $P_T/P_I = |S_{21}|^2$, and $P_I=P_R+P_A+P_T$, the fraction of attenuation due to reflection, f_R, and absorption, f_A, is

$$\begin{aligned} f_R &= |S_{11}|^2 \\ f_A &= 1 - |S_{11}|^2 - |S_{21}|^2 \quad . \end{aligned} \tag{4.19}$$

For example, if $S_{11} = 0.80 = -1.94\,\text{dB}$ and $S_{21} = 0.03 = -30.45\,\text{dB}$, 64% of the incident power is reflected, 0.09% of the power is transmitted, and 35.91% of the power is absorbed.

4.4. Lossy Transmission Lines

We have seen in Chapters 2 and 3 that when a HTS microbridge is subjected to a DC voltage bias, the superconductor switches from a lossless to a lossy state. The switching mechanism is the formation of a stable hotspot, or a region where the temperature has been increased above T_C, so that the superconductor is in the normal state. The length of the hotspot is predicted to increase as the applied voltage is increased. When the hotspot is present on a microwave transmission line, the transmission line is lossy, and microwave signals are attenuated. Lossy transmission lines are treated in several books,[46,47] although they only treat the special case where the losses are small, and are uniformly distributed along the entire line. When a hotspot is present on a transmission line, the losses are usually not small, and they are localized to a small region of the entire line. In this section, we develop the theory to explain the operation of transmission lines under these conditions. Two different

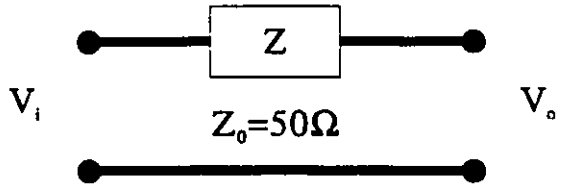

Fig. 4.6. Transmission line of characteristic impedance Z_0 with a lumped element impedance Z in series.

regimes are investigated. Under conditions of small bias voltages and low frequencies, the hotspot can be treated as a lumped element impedance (a zero length approximation). With larger biases and/or at higher frequencies, the lumped element approximation breaks down and a more detailed model that takes into account both the hotspot attenuation and the multiple reflections from each end of the hotspot must be used.

4.4.1. The Lumped Element Approximation

In this section, we derive the transmission coefficient S_{21} for a transmission line of characteristic impedance Z_0 having a lumped element series impedance Z as shown schematically in Fig. 4.6. A lumped element refers to a resistor, inductor, or capacitor having a length much smaller than the operating wavelength. While the concept of a lumped element is strictly valid only as the length and/or operating frequency approach zero, in practice they can be used as good approximations provided that their length is less than $\lambda/10$.

To derive the transmission coefficient for the circuit shown in Fig. 4.6, one can use the so-called transmission or $ABCD$ matrix.[48] If a lumped element series impedance Z is inserted into a lossless transmission line of characteristic impedance Z_0, the $ABCD$ matrix can be used to show that the transmission coefficient is

$$S_{21} = \frac{2Z_0}{2Z_0 + Z} \quad . \tag{4.20}$$

It should be emphasized that this transmission coefficient must be measured at the location of the impedance. If S_{21} is measured at some distance l beyond the impedance, it will have an additional phase shift of $e^{-j\beta l}$, where β is the propagation constant of the lossless transmission line. Eq. 4.20 can be inverted to solve for the impedance, giving

$$Z = 2Z_0\left(\frac{1 - S_{21}}{S_{21}}\right) \quad . \tag{4.21}$$

4.4.2. The Distributed Loss Model

At frequencies and/or applied voltages when the hotspot is longer than about $\lambda/10$, using a lumped element analysis is no longer possible. Instead, the distributed nature of the hotspot must be accounted for. Shown below in Fig. 4.7, the hotspot is modelled as a very lossy section of transmission line of characteristic impedance Z and length l imbedded in a lossless transmission line of characteristic impedance Z_0. The hotspot has a resistance per unit length R, and the inductance and capacitance per unit length, L and C, are unchanged from their values in the adjacent lossless regions.[n]

The characteristic impedance of the lossy transmission line is given by Eq. 4.11, although we will ignore the shunt conductance loss term, G. This is a good assumption because the losses in the dielectric are quite small. The loss tangent[49] of the $LaAlO_3$ substrate

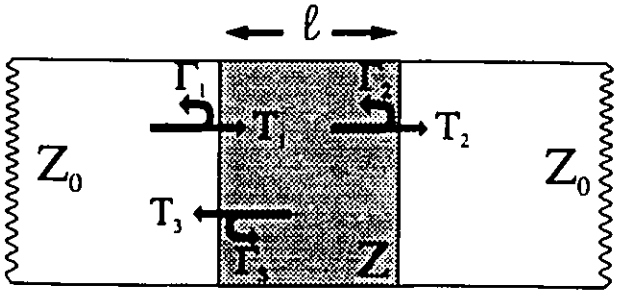

Fig. 4.7. This figure shows the model used to describe the effect of a hotspot on microwave transmission. The hotspot is modelled as a lossy section of transmission line imbedded within a lossless transmission line. Shown in the figure are the voltage reflection and transmission coefficients. At both interfaces, the microwave signal is partially reflected and partially transmitted, and the signal is attenuated while travelling through the lossy section.

[n] The inductance and capacitance per unit length depend primarily on the geometry of the transmission line. For the capacitance per unit length, this is fairly clear. The inductance per unit length, however, is made up of the series combination of the geometric inductance of the transmission line and the kinetic inductance of the superconductor. Since the temperature of the superconductor is above T_c, the kinetic inductance term vanishes in the hotspot, so the inductance should decrease slightly in the hotspot region. The kinetic inductance, however, is smaller than the geometric inductance, so the net effect is small. This approximation will be justified at the end of this chapter.

used in this work is less than 1×10^{-5} at 77K and 10 GHz.[50] For comparative purposes, the loss tangent of G-10, an epoxy-glass composite dielectric commonly used in electronic applications, is 0.008.[51] With such a small loss tangent, the dielectric losses at 10 GHz in a coplanar waveguide transmission line would be[52] 0.04 dB/cm. Since the hotspot introduces losses on the order of 20 dB/cm, the dielectric loss can be ignored. The propagation constant can be calculated using Eq. 4.8, again simplified by ignoring the shunt conductance per unit length. Because there is an impedance mismatch at both superconductor-hotspot interfaces, there will be a partial reflection and partial transmission, with a reflection coefficient at each interface governed by Eq. 4.15. Summarizing, the characteristic impedance in the lossless region and in the hotspot are, respectively,

$$Z_0 = \sqrt{\frac{L}{C}}, \quad \text{and } Z = \sqrt{\frac{R + j\omega L}{j\omega C}}. \tag{4.22}$$

The propagation constant in the hotspot is given by

$$\gamma = \sqrt{(R + j\omega L)(j\omega C)}, \tag{4.23}$$

and the voltage and current are determined using Eq. 4.9. Note that in the hotspot, because of the resistive loss term, both the characteristic impedance and the propagation constant are complex numbers. For the characteristic impedance, this means that the voltage and current are no longer in phase. For the propagation constant, travelling waves will be exponentially attenuated as they move through this region. The reflection coefficients shown in Fig. 4.7 are given by

$$\Gamma_1 = \frac{Z - Z_0}{Z + Z_0}, \text{ and } \Gamma_2 = \Gamma_3 = \frac{Z_0 - Z}{Z + Z_0} = -\Gamma_1. \tag{4.24}$$

The transmission coefficients are simply related to the reflection coefficients. Since the voltage must be continuous across any interface, the transmission coefficient, T, at any interface is given by $T = 1 + \Gamma$. Therefore, the transmission coefficients shown in Fig. 4.7 are

$$T_1 = 1 + \Gamma_1 = \frac{2Z}{Z + Z_0},$$

$$T_2 = 1 + \Gamma_2 = \frac{2Z_0}{Z + Z_0} = 1 - \Gamma_1, \qquad (4.25)$$

$$\text{and } T_3 = 1 + \Gamma_3 = T_2 .$$

We would like to determine the total transmission coefficient. Since we know the reflection and transmission coefficients and the propagation constant of the lossy section of the line, the total transmission coefficient can now be determined by the infinite series shown below:

$$T = T_1 T_2 e^{-\gamma l} + T_1 T_2 \Gamma_2 \Gamma_3 e^{-3\gamma l} + T_1 T_2 (\Gamma_2 \Gamma_3)^2 e^{-5\gamma l} + \ldots$$

$$= T_1 T_2 e^{-\gamma l} \left[\sum_{n=0}^{\infty} \left(\Gamma_2 \Gamma_3 e^{-2\gamma l} \right)^n \right]. \qquad (4.26)$$

This infinite series may be evaluated by noting[53] that $\sum_{n=0}^{\infty} x^n = \frac{1}{1 - x}$ for $|x| < 1$. Simplifying and expressing the reflection and transmission coefficients in terms of Γ_1 gives

$$T = \frac{\left(1 - \Gamma_1^2\right) e^{-\gamma l}}{\left(1 - \Gamma_1^2 e^{-2\gamma l}\right)} . \qquad (4.27)$$

This expression allows us to determine the magnitude and phase of the transmission coefficient as a function of the length and resistance per unit length of the hotspot with respect to its leading edge. As for the lumped element approximation, if the transmission coefficient is measured at some position other than the leading edge, there will be an additional phase shift that must be accounted for.

4.5. Coplanar Waveguide Design

A coplanar waveguide transmission line, shown in Fig. 4.2(c), consists of a center signal conductor of width w and two adjacent ground planes separated from the center conductor by a gap of width g. CPW, like microstrip, has two different dielectric media in which the electromagnetic wave must propagate. Consequently, attaining a true TEM wave is impossible, since the phase velocity in the air and dielectric filled regions are different. While the actual fields constitute a hybrid TE-TM wave, they are adequately approximated at low frequencies by a quasi-TEM approximation.[54] In this approximation, the effect of the multiple dielectrics is accounted for by using an effective dielectric constant, ϵ_{eff}. The effective dielectric constant can be thought of as an average value calculated so that the phase velocity in the overall transmission line obeys normal TEM equations: $v_p = c/\sqrt{\epsilon_{eff}}$.

Design equations for CPW exist[55,56] that allow the characteristic impedance and effective dielectric constant to be calculated for any given geometry and material parameters. The characteristic impedance is given by

$$Z_0 = \frac{30\pi}{\sqrt{\epsilon_{eff}}} \frac{K(k')}{K(k)} \quad \textbf{(4.28)}$$

The effective dielectric constant is given by

$$\epsilon_{eff} = 1 + \frac{\epsilon_r - 1}{2} \frac{K(k')K(k_1)}{K(k)K(k_1')} \quad \textbf{(4.29)}$$

In these two equations, K is the complete elliptic integral of the first kind,

$$k = \frac{w}{w + 2g}, \quad k_1 = \frac{\sinh\left(\frac{\pi w}{4h}\right)}{\sinh\left(\frac{\pi(w + 2g)}{4h}\right)}, \quad \text{and } k' = \sqrt{1 - k^2}. \quad \textbf{(4.30)}$$

To minimize the DC power consumption of the microwave switch, the center conductor must be made as narrow as possible. We therefore taper the width of the center conductor from a relatively wide value to allow good mating with connectors to a relatively narrow value. This tapering must be done maintaining a 50 Ω characteristic impedance throughout the transition to reduce any impedance mismatch reflections. This type of transition can be done in CPW, but could not be done in microstrip where the impedance solely depends on the width of the conductor.

Shown in Fig. 4.8 is the required relationship between the gap and width for a 508 μm thick dielectric with a dielectric constant of 24. These are the material parameters corresponding to the $LaAlO_3$ substrates used for all work described in this thesis. Using a third order polynomial fit to the data, the gap required to maintain a 50 Ω impedance is $g = -0.1558 + 1.9271w + (6.1339\text{x}10^{-4})w^2 - (4.4797\text{x}10^{-6})w^3$. Figure 4.9 shows the effective dielectric constant as a function of the width of the center conductor. The gap has been chosen so that the characteristic impedance is 50 Ω.

The capacitance and inductance per unit length can be determined once the effective dielectric constant is known. The phase velocity is $v_p = \frac{1}{\sqrt{LC}} = \frac{c}{\sqrt{\epsilon_{eff}}}$. The characteristic impedance is given by Eq. 4.11, $Z_0 = \sqrt{\frac{L}{C}}$. This allows us to solve for the capacitance per unit length in terms of the characteristic impedance and the effective dielectric constant:

$$C = \frac{\sqrt{\epsilon_{eff}}}{Z_0 c} \quad . \tag{4.31}$$

Since the characteristic impedance is 50 Ω, the capacitance per unit length is determined once the effective dielectric constant is known. The self inductance per unit length is also easily determined, since $L = Z_0^2 C$. For a CPW line with a 508 μm thick dielectric of dielectric constant 24, a center conductor width of 5 μm and a gap of 9.46 μm, the characteristic impedance is 50 Ω and the effective dielectric constant is 12.50. This means the capacitance per unit length is 2.35 pF/cm, and the geometric inductance per unit length is 5.9 nH/cm.

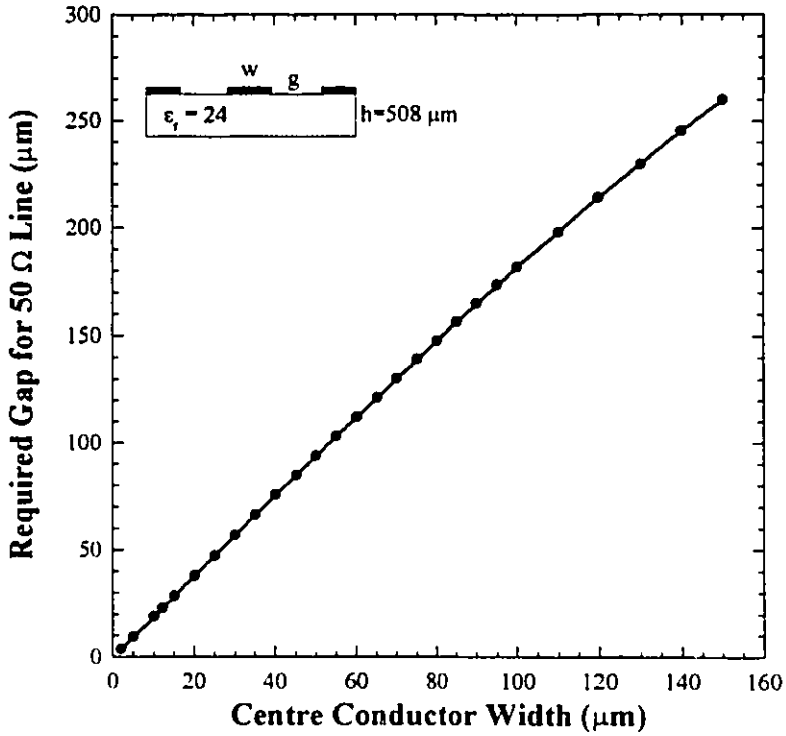

Fig. 4.8. Relationship between center conductor width and the gap between the center conductor and the ground plane for 50 Ω coplanar waveguide.

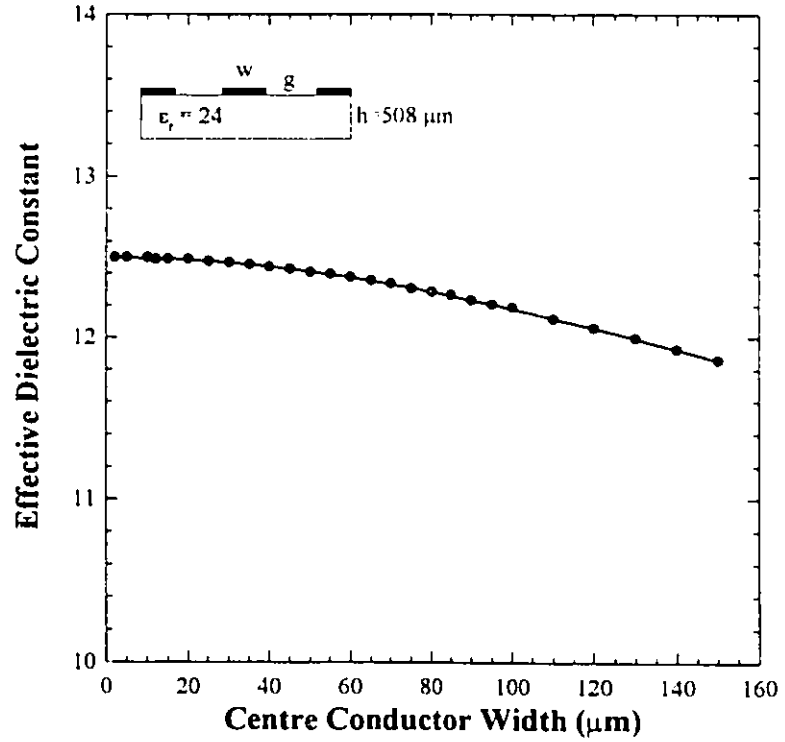

Fig. 4.9. Effective dielectric constant as a function of the center conductor width for a 50 Ω coplanar waveguide transmission line.

We can now determine if the kinetic inductance for the devices studied in this thesis is smaller than the geometric inductance as discussed in footnote n on page 50. We have designed two different structures tapering to final line widths of 5 and 10 μm, respectively. In both cases, the length of the narrow tapered region was 1 mm. The kinetic inductance per unit length of a superconducting bridge of width w and thickness d is approximately given by[57]

$$L_{kin} = \frac{\mu \lambda_L^2}{wd} \quad , \tag{4.32}$$

where μ is the permeability and λ_L is the London penetration depth. A more complicated and accurate expression derived specifically for a CPW transmission line is found in Ref. 28 where the kinetic inductance of a 200 nm thick, 5 μm wide CPW patterned $YBa_2Cu_3O_{7-\delta}$ film having a penetration depth of 250 nm[27] at 77K is 1.25 nH/cm (Eq. 4.32 gives an estimate of 0.8 nH/cm). Since the kinetic and geometric inductances add in series, the kinetic inductance represents about 17% of the total inductance of the transmission line. This fraction increases at higher temperatures because the penetration depth increases rapidly as the temperature approaches T_C as discussed in Chapter 2. As seen in Eq. 4.32, kinetic inductance is also more important for thinner lines since the geometric inductance is insensitive to changes in the line width, while the kinetic inductance increases with decreasing line width. For example, for a 1 μm wide CPW transmission line, both the geometric and kinetic inductances are 5.9 nH/cm, and the kinetic inductance will be important in transmission line design. Conversely, for a 10 μm wide line, the geometric inductance is unchanged, but the kinetic inductance has decreased to 0.07 nH/cm, and can be ignored in modelling. In this thesis, the kinetic inductance has been ignored in the design of both the 5 and 10 μm wide CPW transmission lines. This will not affect the 10 μm wide line appreciably. For the 5 μm wide line, the actual characteristic impedance will be approximately 8% higher than given in Eq. 4.28 when the device is in the superconducting state.

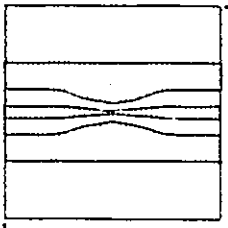

MICROWAVE MEASUREMENTS

5.1. Packaging

In order to carry out measurements on a processed $YBa_2Cu_3O_{7-\delta}$ device, it is necessary to enclose the device in a suitable microwave housing and to make electrical connections to it that are compatible with the network analyzer. The enclosure and the electrical connections must be designed to minimize measurement artifacts. A schematic view of the housing used for all microwave measurements is shown in Fig. 5.1. Note that the device is supported only along its edges, and there is a large air space between the bottom of the mounted device and the lower surface of the housing. This was done to ensure that the transmission line is a true coplanar waveguide (CPW), and not a conductor backed coplanar waveguide (CBCPW) where a ground plane exists on the backside of the device. CBCPW is attractive because it allows for good thermal contact to the back surface of the device. Unfortunately, this structure can support microstrip-like modes in addition to the desired CPW mode.[58,59] These modes can resonate inside the package, leading to sharp resonance features in transmission and reflection measurements. Initial designs for the microwave switch discussed in this thesis used CBCPW transmission lines, and these resonances were clearly observable. A variety of techniques including the fabrication of vias[60] from the upper to lower ground planes and the use of multiple dielectric layers[61,62] have been proposed to eliminate the microstrip-like modes. However, the most effective technique is to ensure that there is no lower ground plane present. This was done by inserting microwave absorbing foam[63] into the air space underneath the mounted device. The foam is used as damping material to suppress package resonances. It has no significant effect on the insertion loss of the device.

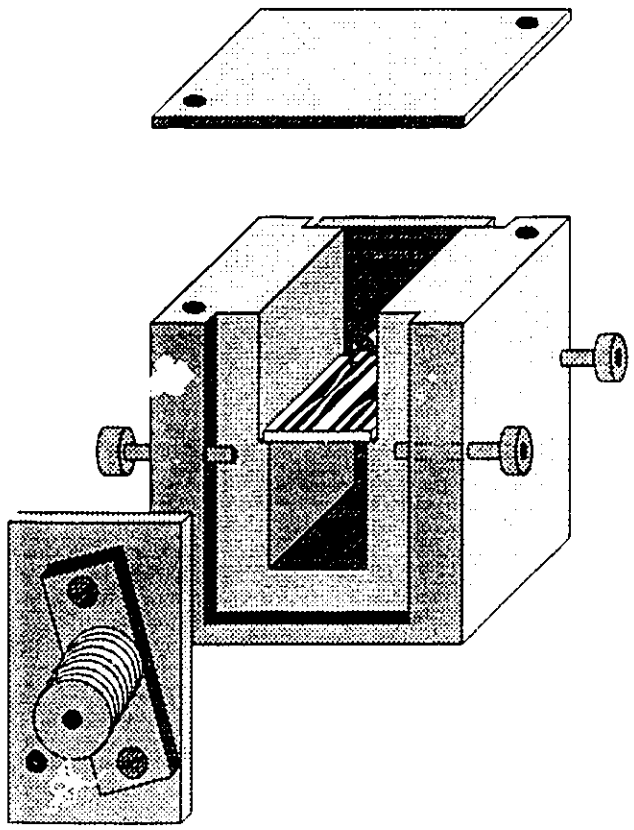

Fig. 5.1. This figure illustrates the microwave housing assembly used for all microwave measurements. The housing is fabricated from brass, and is designed to accept 1x1 cm films on 508 μm thick substrates. Two devices, separated by 5 mm, are fabricated on each film. Because the coaxial connector is quite large, only one K-connector™ can be installed on each end at one time. To make measurements on the other device, the coaxial connector is pivoted about the top screw on the end plate. A top plate is installed to firmly hold the end plates in position when the network analyzer test set cables are connected with a torque of 8 in-lb. The housing is not completely sealed once the top plate is installed, as there are several holes (not shown in the figure) that allow liquid nitrogen to enter and fill the housing, thereby ensuring that the device has a good thermal heat sink.

The patterned device was fixed in place to the housing by applying silver paint around the device periphery. The end plates were then installed, held in place with two counter opposing screws, and Wiltron K-connectors™[64] with sliding pin contacts were used to make electrical connections to the signal conductors of the device. The use of counter opposing screws gave a lateral adjustment of 2 mm to the end plates so that the sliding contacts could always be positioned exactly over the 150 μm wide center conductor. Once this was done, a short piece of 150 μm wide, 25 μm thick rectangular gold ribbon was attached between the sliding contact and the gold contact pad on the center conductor using a Westbond 7400A ultrasonic bonder. The ultrasonic bonder was fitted with a TiC wedge bonding tip heated to 150°C, and bonding was carried out using 650 mW of ultrasonic power applied for 300 msec. These power settings are important. If too much ultrasonic power is applied for too long a period of time, the gold contact pads will be damaged; if the power is too low, the gold ribbon will not stick to the contact pads. The advantage of using this technique to make electrical connections is that the sliding contacts and gold ribbon act as a built in strain relief, and connections are much less likely to fail when subjected to the thermal shock of being immersed in liquid nitrogen. Additionally, there is very little geometric mismatch between the sliding contact, the gold ribbon, and the center conductor, and connector reflections are thereby minimized.

After the K-connectors™ had been attached to the center signal plane of the CPW circuit, the ground planes were electrically connected to the housing with conductive silver paint. The silver paint was applied so that the housing was in electrical contact with each of the gold contact pads on the ground planes. Because the gap between the center conductor and the ground plane was only 260 μm, care was taken to ensure that the ground planes were not shorted to the signal planes. When all of the electrical connections had been tested, the lid was installed onto the housing.

The device could now be connected to the network analyzer for testing. To ensure that the network analyzer test set cables were not damaged by the liquid nitrogen in which the device was immersed, two 15 cm long Wiltron flexible coaxial connectors[65] were inserted between the test set cables and the K-connectors™. The flexible connectors were bent to

allow the device under test to rest on the bottom of the liquid nitrogen container, and the test set cables were not subjected to a cryogenic environment.

5.2. Microwave Network Analyzer

Microwave measurements were carried out using an HP8510B network analyzer operating with an output power of 10 dBm. It was calibrated at room temperature using open, short, and 50 Ω load calibration standards, since suitable cryogenic standards did not exist.[66] The calibration standards were attached to the ends of the 15 cm long flexible coaxial cables. Because the calibration was done at room temperature, an absolute measurement of the insertion loss of the unbiased device was not possible. However, since the transmission line is fully superconducting, this insertion loss is expected to be negligible. The entire calibration technique is summarized in Table 5.1 and is described in detail in the remainder of this section. The accuracy of the network analyzer for transmission measurements is specified to be ±0.22 dB, and the phase accuracy is ±4.7 degrees.

Biasing of the device under test was carried out using the built in bias-tee in the network analyzer. The bias voltage was applied to port 1, and port 2 was grounded. The bias-tee introduces a series resistance between the Keithley Model 238 Source Measure Unit (SMU) used for biasing and the device under test. The total series resistance, comprising the bias-tee, cable, and contact resistance, was determined by immersing the device in liquid nitrogen, applying a 100 μA DC current, and measuring the total supply voltage. For a 5 μm wide, 200 nm thick bridge, 100 μA corresponds to a current density of 0.01 MA/cm^2, two orders of magnitude smaller than the critical current density. With negligible bridge resistance, the total series resistance of the bias-tee, cables, and contacts was measured to be 18 Ω. In determining the resistance of the device, this value was always subtracted from the total resistance measured on the SMU.

All transmission measurements were made relative to the unbiased, lossless line using the memory division feature of the network analyzer. A measurement of the magnitude and phase of S_{21} was made with no bias applied to the transmission line. This measurement was stored in the network analyzer's internal memory, and all subsequent measurements made on biased lines were divided by the stored data. In this manner, the S_{21} magnitude data is

1. Do a full two port calibration using open, short, and load calibration standards at room temperature.
2. Connect the superconducting device to the test set cables and cool it to 77K.

Reflection (S_{11}) Measurement	Transmission (S_{21}) Measurement
R1. With no bias applied, observe the time domain reflection using the time domain low pass feature of the network analyzer.	T1. With a 10 V bias applied, observe the transmitted signal in the time domain using the time domain bandpass feature.
R2. To ensure that we are justified in gating out the connector reflections, increase the bias to 10 V so that a large reflection from the hotspot occurs. If the reflection from the first connector is unchanged, we are justified in gating it out. Repeat the procedure for S_{22} to ensure the other connector can also be gated out. The gate width can now be determined. It is chosen to be as wide as possible while removing the reflections from both connectors. A gate width of 0.125 ns was found to be satisfactory.	T2. Centre the gate on the peak of the transmitted signal. With the gate applied, observe the signal in the frequency domain. Turn off the gating, and observe the change in the transmission data. If the ripple is removed without altering the overall shape of the S_{21} curve, the gate width is appropriate. If the shape changes substantially, the gate width should be increased. A width of 0.17 ns was optimal.
R3. Reset the bias to 0 V. Centre the 0.125 ns wide gate midway between the connector reflections. With the gate in effect, observe and store the reflection data in the frequency domain. [With no applied bias, there is no reflection from the hotspot, so the gate cannot be centred on the reflection from the hotspot].	T3. Set the applied bias voltage to zero, and centre the 0.17 ns wide gate on the peak of the transmitted signal. Store this data (both magnitude and phase) in the network analyzer memory.
R4. Apply a non-zero bias voltage and observe the reflection in the time domain. Centre the 0.125 ns wide gate on the peak of the reflected signal.	T4. Apply a non-zero bias voltage, and observe the transmitted signal in the time domain. Centre the gate on the peak of the transmitted signal.
R5. Observe and store the reflection data in the frequency domain. Repeat steps R4 and R5 for all other applied bias voltages.	T5. Observe the transmission data in the frequency domain. Normalize it to the unbiased transmission line by dividing it by data stored in memory. Use complex division so both magnitude and phase are normalized. Store the normalized data.
	T6. Repeat steps T4 and T5 for all other bias voltages.

Table 5.1. Calibration summary.

normalized to the unbiased data so that, on a logarithmic scale, the unbiased data is subtracted from the biased data. Since the unbiased S_{21} data will be very close to 0 dB, the magnitude correction will be a small one. The actual correction was found to be less than 3 dB over the entire frequency range of 75 MHz to 30 GHz.

There is a greater advantage in using the memory division for the S_{21} phase data. The phase of the transmission coefficient is always measured with respect to reference planes, as depicted in Fig. 4.5 on page 47. These reference planes are determined during the calibration, with the port 1 reference plane located at the position of the calibration standards placed on port 1, and the port 2 reference plane located at the position of the calibration standards placed on port 2. Since there will necessarily be a transmission line of length l between the two ports, the measured phase, $\phi = -\beta l$, will be a linear function of frequency. We are primarily interested in the effect of the hotspot on the transmission coefficient, so the linear phase is unimportant. By using the memory division feature, the phase of the transmission coefficient with no bias applied is subtracted from the measured phase with bias applied, when a hotspot exists. Memory division therefore gives us the relative effect of the hotspot on the phase of the transmitted signal. This relative measurement is of importance since we can easily compare it with theory. An absolute phase measurement would require knowledge of the exact position of the reference planes, the exact electrical length of the coaxial connector and the transmission line between the reference planes and the hot spot, and the exact position and length of the hot spot.

One further feature of the network analyzer which was used extensively was time domain gating. The network analyzer is fundamentally a frequency domain instrument. However, it has a built in Fourier transform routine which can convert the frequency domain data to time domain data. When S_{11} measurements are being made, this feature can be used to do time domain reflectometry measurements. When S_{21} measurements are selected, the Fourier transform displays the amplitude of the transmitted signal as a function of time. Gating is then used to remove those parts of the transmitted signal which are not associated with the device under test, but which nevertheless affect the measurement. One very common use of this technique is to artificially remove the effects of imperfect connectors. Ideally, the connectors would be lossless and they would not give rise to any reflections. In practice, of

course, the connectors always cause small reflections. These reflections are responsible for a small amplitude ripple in the frequency domain that is unrelated to the physical characteristics of the device under test, but is only an artifact caused by packaging imperfections. In the transmission measurements presented in this chapter, a rectangular gate 0.17 ns wide° was centered on the peak of the transmitted time domain signal. Any transmitted components outside of this gate (corresponding to multiple reflections from the connectors) were filtered out. The time domain data was then reconverted to frequency domain data by the network analyzer, removing any spurious connector induced ripple from the transmission data. Typically, prior to gating, the ripple had a peak to peak height of less than 2 dB, and was periodic in frequency with a period of approximately 300 MHz. The gate width was chosen somewhat empirically. It was made as long as possible so that ripple was removed, but the overall shape of the transmission data was unaltered.

All of the procedures described above were automated. A computer program was written to control the network analyzer and the SMU so that the device under test could be biased appropriately, its DC resistance could be measured, and microwave measurements could be made with appropriate gating. Both time domain and frequency domain measurements were recorded.

5.3. Microwave Measurements and the Lumped Element Model

Shown in Figs. 5.2 and 5.3 are graphs showing the measured reflection and transmission coefficients as a function of the applied bias. As expected, as the bias voltage increases, the reflection increases while the transmission decreases. Reflection data for the

---

° From Fig. 5.9, the phase velocity in the hotspot is ω/β = 23 mm/s at 15 GHz, so a 0.17 ns wide gate corresponds to a length of 4 mm. The maximum length of the hotspot is 1 mm, so this gate width will allow at least two multiple reflections in the hotspot. Since the signal will be strongly attenuated in this region, two reflections are sufficient to get an accurate measurement. Outside of the hotspot, the effective dielectric constant is 12.5, so signals propagate at 85 mm/ns and a time of 0.17 ns corresponds to a length of 14.5 mm. Since the distance between the connector and hotspot is about 5 mm, it will be possible to get a single multiple reflection, but all further reflections are removed. The connector reflections were quite obvious when time domain measurements of the S_{11} data were carried out. The reflection from the first connector was observed to be constant as the bias voltage was increased, while the reflection from the hotspot increased dramatically.

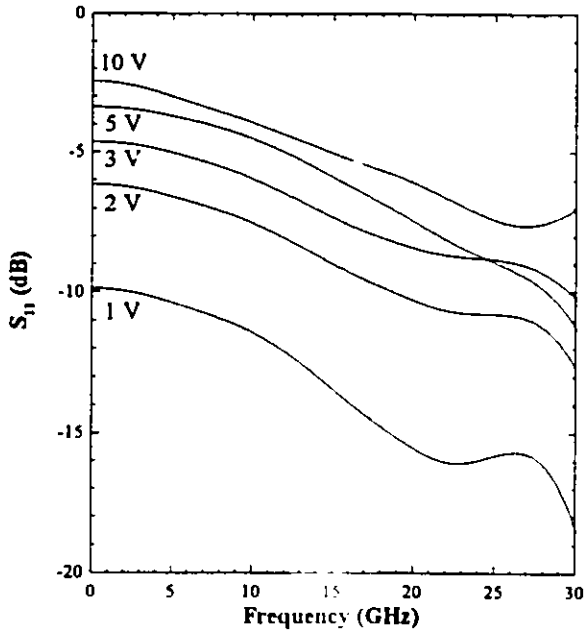

Fig. 5.2. Reflection coefficient as a function of applied bias for a tapered CPW transmission line. The line tapers to a final center conductor width of 5 μm, and the length of the 5 μm wide region is 1 mm. Each curve consists of 401 data points, equally spaced in frequency from 75 MHz to 30.075 GHz. For clarity, only five curves are shown. The unbiased transmission line (not shown in the figure) has a return loss of greater than 20 dB.

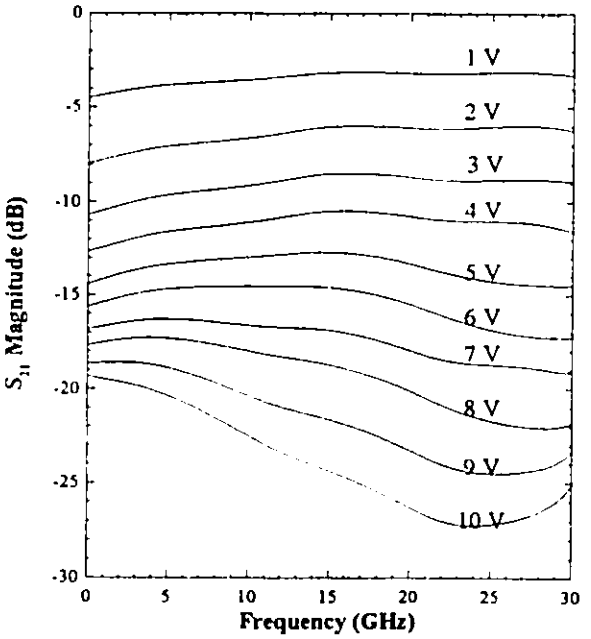

Fig. 5.3. Transmission coefficient as a function of applied bias, normalized to the unbiased transmission coefficient. Each curve consists of 401 data points, equally spaced in frequency from 75 MHz to 30.075 GHz.

unbiased transmission line is not shown, since it is off the scale of the graph. It was less than -20 dB over the entire frequency range. In this section, the transmission data will be compared with predictions based on the lumped element model, where the hotspot is assumed to be electrically short.

As discussed in Section 4.4.1 on page 48, the lumped element model can be used to describe device performance at low frequencies and/or when the bias voltage is small so that the hotspot length is much smaller than the wavelength. The relationship between the series impedance and the transmission coefficient is given by Eq. 4.21. When this equation is applied to the data in Fig. 5.3, the microwave resistance as a function of bridge voltage can be determined[P] at different frequencies, and we can see over what range the lumped element approximation is valid. More importantly, we can gain an insight regarding the microwave performance of the hotspot, as discussed below. Figure 5.4 shows the computed microwave resistance and the measured DC resistance as a function of the bridge voltage.

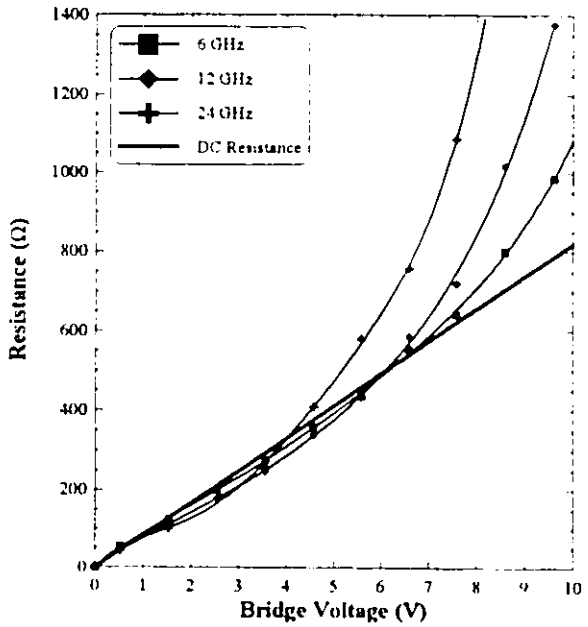

Fig. 5.4. Calculated microwave resistance and DC resistance versus bridge voltage at three different microwave frequencies.

[P]In general, S_{21} has both a magnitude and a phase. The phase is not shown here, but in Section 5.4, it will be shown to be zero at low frequencies and/or with small applied bias voltages, i.e. under those conditions where the lumped element approximation is valid. This means that both S_{21} and the series impedance Z are real and the hotspot looks like a pure series resistor.

There are several important conclusions to be drawn from this figure. At all frequencies, the microwave resistance is essentially equal to the DC resistance for small bridge voltages (less than 4V in Fig. 5.4). This was initially rather surprising, since the microwave resistance was expected to equal the small signal resistance of the device (the inverse of the slope of the I-V curve), with the DC bias fixing the operating point of the device. Since the current is almost constant after switching, the small signal resistance should be quite large. This apparent discrepancy can be explained by considering the response time of the hotspot to changes in the applied voltage. At very low frequencies, the hotspot will easily be able to follow the changes; as the voltage increases, the hotspot will become longer and its resistance will increase to remain in equilibrium with its environment. However, as seen in Chapter 2, the size of the hotspot is governed by the rather slow diffusion of heat from the film to the substrate and cryogen. Therefore, as the frequency increases, the hotspot will eventually no longer be able to respond quickly enough to follow the changes in the applied voltage. At frequencies greatly exceeding the intrinsic hotspot response time, the hotspot will not respond at all to the voltage changes, and the resistance will equal the DC resistance. A detailed investigation of the frequency response of the small signal resistance has been carried out,[67] and the small signal resistance appears to saturate at its DC value for frequencies above 100 kHz. The response time of the hot spot is indeed quite slow.

A second conclusion that may be drawn from Fig. 5.4 concerns the range of validity of the lumped element approximation. Note that the calculated microwave resistance departs significantly from the DC resistance as the bridge voltage is increased. Furthermore, this departure voltage decreases as the frequency increases. At 6 GHz, the microwave resistance is seen to equal the DC resistance until a bridge voltage of approximately 8.5V. At 24 GHz, the microwave resistance departs from the DC resistance at 4V. The shorter wavelength associated with a higher frequency results in the lumped element approximation being valid over a smaller voltage range.[q]

[q] The range of validity of the lumped element approximation can be investigated further with the aid of the distributed loss model and Figs. 5.7 and 5.9. At 6 GHz, the wavenumber within the hotspot is computed to be 0.0024 μm^{-1} so the wavelength is 2.6 mm. With an applied voltage of 8V, the hotspot length is 450 μm, corresponding to an electrical length of $\lambda/6$. At 24 GHz, the wavenumber is 0.0054

5.4. Microwave Measurements and the Distributed Transmission Line Model

The distributed transmission line model, initially discussed on page 50 in Section 4.4.2, gives a more complete explanation than the lumped element approximation. To reiterate, this model assumes that the resistive losses in the hotspot are distributed along its entire length, while the inductance and capacitance per unit length are unchanged from the lossless region. Because of the added resistance in the hotspot, the characteristic impedance in this region is no longer 50 Ω so there will be reflections at the hotspot-superconductor interfaces at both ends of the hotspot. The net transmission coefficient is computed by summing the multiple reflections, taking into account the exponential attenuation occurring within the hotspot, as described by Eq. 4.27. All of the parameters in this equation are directly determined from the resistance, inductance, and capacitance per unit length and the length of the hotspot.

The model makes predictions for the magnitude and phase of the transmitted signal. Because the capacitance and inductance per unit length are known, the only two unknown parameters which can be adjusted to fit the model to the measured data are the resistance per unit length and the length of the hotspot. These two parameters are related since the total resistance of the hotspot, given by their product, is known, and must equal the DC resistance. This fact is clear in light of results from the lumped element model described above, where it was seen that the microwave resistance is equal to the DC resistance. One additional piece of information comes from the DC hotspot measurements discussed in Chapter 4. When the bias voltage is increased, only the length of the hotspot changes. The temperature distribution and therefore the resistance per unit length of the hotspot does not change, so the resistance per unit length used in the distributed loss model must be independent of the applied voltage. As a result, the resistance per unit length can be adjusted at one voltage only so the model matches the measured data. All subsequent modelling for other applied voltages is done using this value, with the hotspot length calculated by dividing the measured DC resistance by the constant resistance per unit length.

Figures 5.5 and 5.6 show the magnitude and phase, respectively, of S_{21} for bias voltages from 1 to 10V. As discussed above in Section 5.2, the measured data has been

---

μm^{-1}, the wavelength is 1.16 mm, and the hotspot length is 200 μm, or again $\lambda/6$.

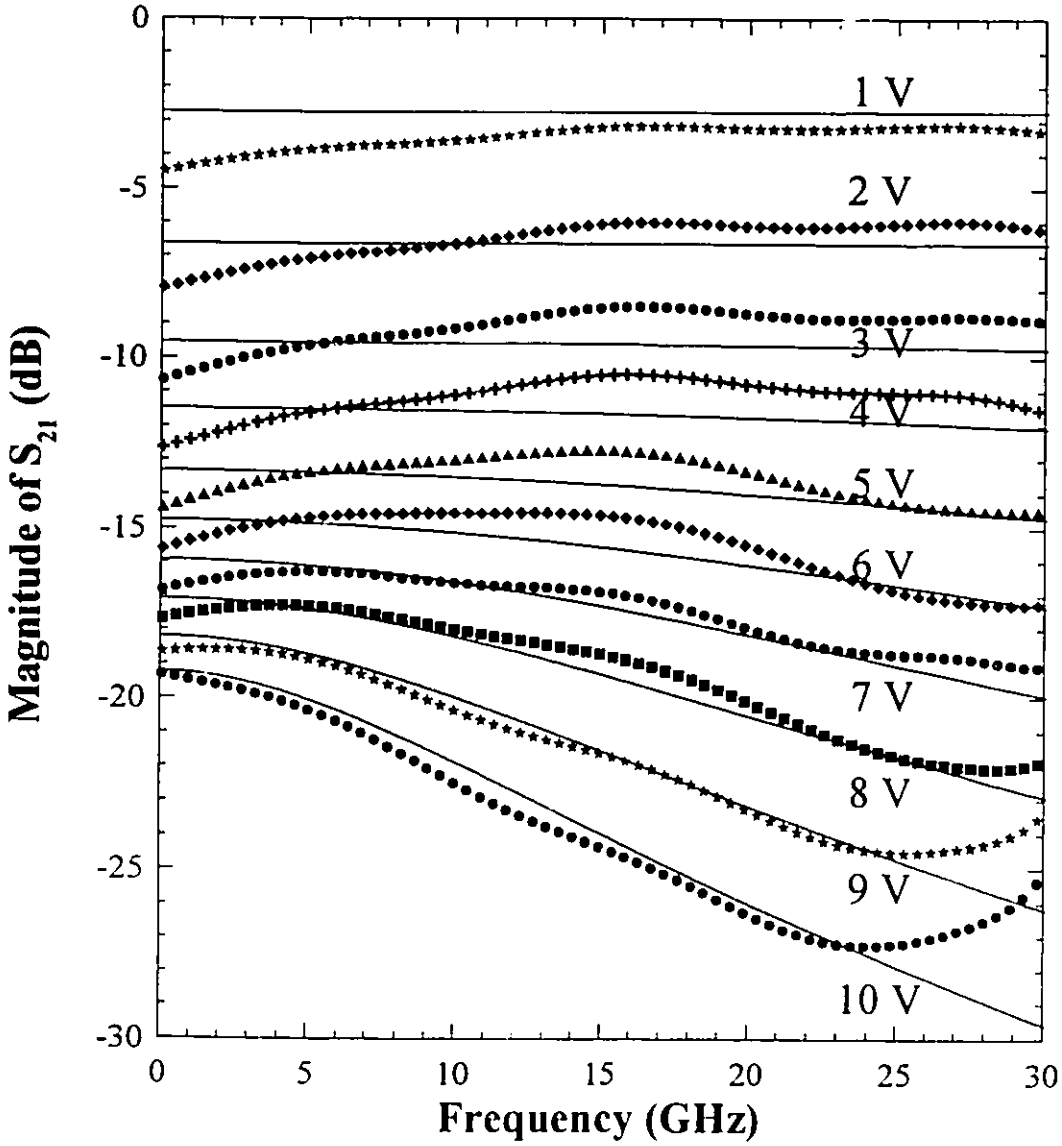

Fig. 5.5.Measured (symbols) and modelled (lines) transmission coefficient magnitude versus frequency for applied bias voltages from 1 to 10 V applied to a tapering CPW transmission line with a final center conductor width of 5 μm. For graph clarity, only every sixth measured data point is shown. The model used a capacitance per unit length of 235.70 pF/m, an inductance per unit length of 589.25 nH/m, and a resistance per unit length of 1.4 Ω/μm.

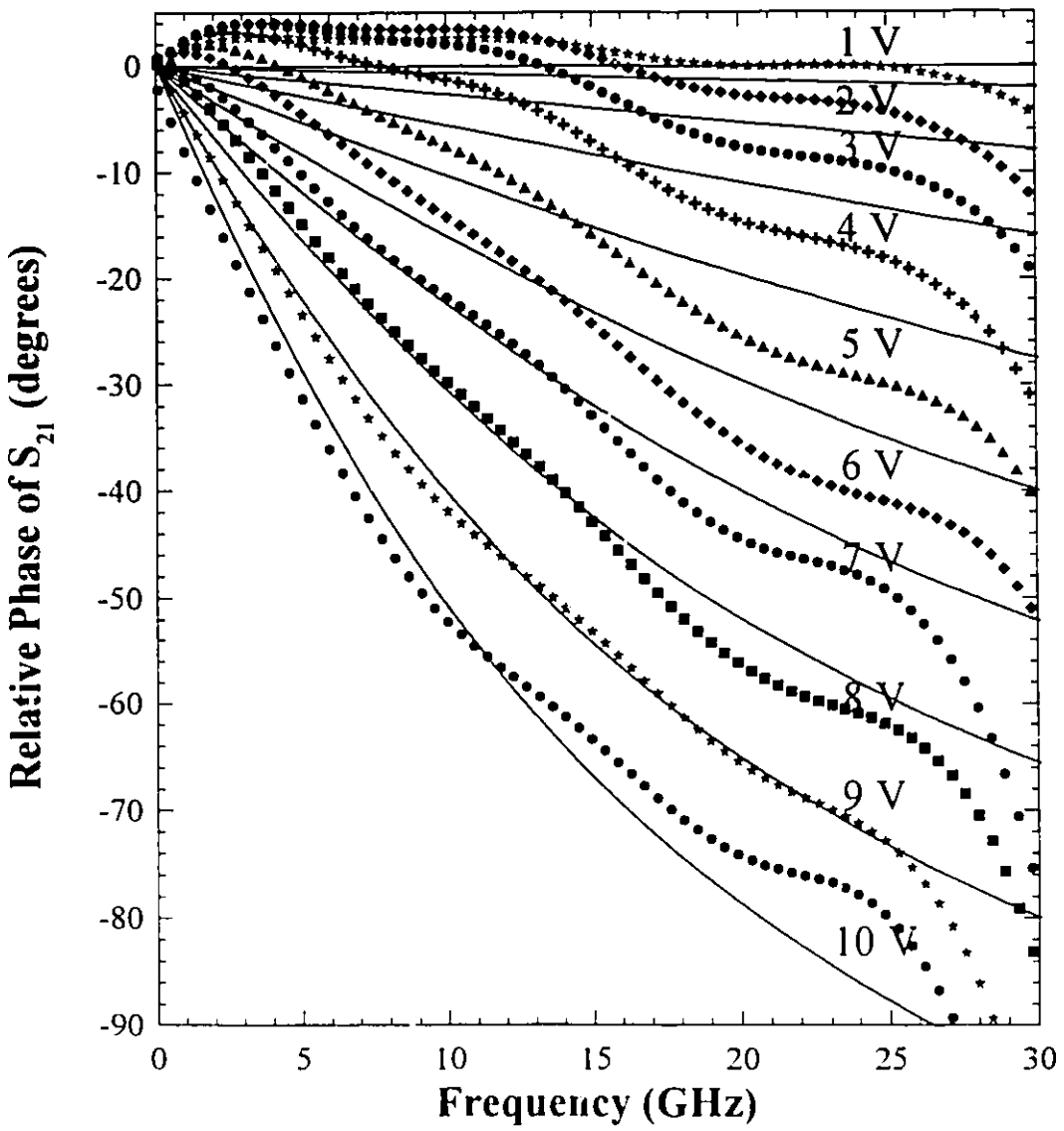

Fig. 5.6. Measured (symbols) and modelled (solid line) transmission coefficient phase as a function of frequency for applied bias voltages from 1 to 10 V. The phase is measured relative to the unbiased transmission line.

normalized to the unbiased transmission line data. The modelled data, shown by the solid lines in the figures, was computed with a resistance per unit length of 1.4 Ω/μm. This value was chosen to give the best match between the measured and modelled data. The distributed loss model gives results that agree well with the measured data. It correctly predicts the increase in attenuation with frequency at higher bias voltages, and the overall phase response due to the hotspot.

There are two areas where there is discrepancy between the measured and modelled results. In Fig. 5.6, the measured phase is slightly positive at low frequencies for small bias voltages, attaining a maximum value of 5°. This is believed to be an indication that the measured phase of the network analyzer is only accurate to about ±3°. The phase also begins to decrease sharply close to 30 GHz, and there is an apparent decrease in attenuation near 30 GHz with bias voltages of 9 and 10 V. This is likely due to overmoding of the transmission line. When measurements are made to 50 GHz, a strong resonance is seen at approximately 33 GHz. Wadell[68] reports that in microstrip, the lowest order TE mode frequency is given by $f_c = c/\left(4h\sqrt{\epsilon_r - 1}\right)$, where c is the speed of light, h is the dielectric thickness, and ϵ_r is the dielectric constant. For our geometry, this equation predicts that the lowest order TE mode can propagate for frequencies above 30.8 GHz, and we assume that the equation is also valid for CPW. Because this mode will not couple well to the K-connectors™, any electromagnetic radiation coupled into this mode will remain in the dielectric, and resonances will result.

Since the hotspot resistance per unit length was assumed to be constant, the length of the hotspot was determined from the total bridge resistance. In Chapters 2 and 3, we saw that the length of the hotspot increases linearly with the bridge voltage, so we expect that the computed hotspot length will also vary linearly with the bridge voltage. Figure 5.7 shows that this is indeed the case.

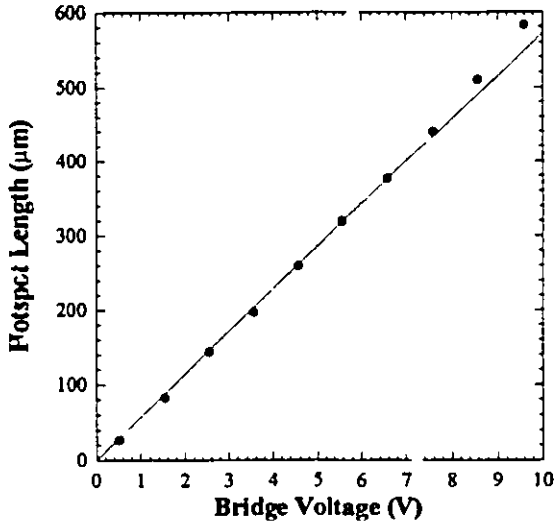

Fig. 5.7. Calculated hotspot length as a function of bridge voltage for the 5 μm wide CPW transmission line. The length was calculated by dividing the measured bridge resistance by the resistance per unit length used in the distributed loss model. The bridge voltage was determined by subtracting the voltage drop in the bias-tee, test set cables, and connectors from the total voltage supplied by the SMU. The solid line is a linear fit to the data.

To understand the behaviour of the transmission as a function of frequency and bias, it is instructive to look at various pieces of information extracted from the distributed loss model. The characteristic impedance of the hotspot, defined in Eq. 4.22 on page 51 is shown in Fig. 5.8. Because the resistance per unit length is independent of the applied bias, this curve will apply for all bias voltages. The magnitude of the reflection at the superconductor-hotspot

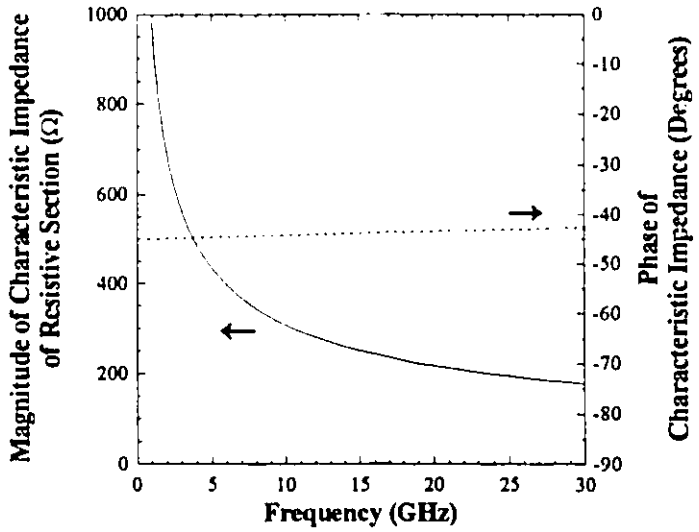

Fig. 5.8. Magnitude and phase of the characteristic impedance of a hotspot having a resistance per unit length of 1.4 Ω/μm. The calculation was done for a line width of 5 μm and a gap of 9.46 μm.

interface depends on the degree of impedance mismatch, so the size of the reflection should decrease with frequency since the characteristic impedance magnitude decreases with frequency. This prediction will be verified in Fig. 5.11.

Because the reflection at the superconductor-hotspot interface gets smaller with increasing frequency, one might expect the transmission to increase with frequency. Figure 5.5 shows that the transmission actually decreases with frequency. This can be understood by looking at the propagation constant, defined in Eq. 4.23 on page 51, and shown in Fig. 5.9. The attenuation coefficient increases with frequency, and this is the main factor which gives rise to enhanced attenuation at higher frequencies.

Looking at the time domain signal is also informative. Shown in Fig. 5.10 is a plot of the transmitted voltage as a function of time, as computed using the Fourier transform feature of the network analyzer. As expected, the transmitted amplitude decreases substantially as the applied bias voltage is increased. Additionally, the pulse arrival time is delayed as the bias is increased. Figure 5.9 shows that the wavenumber in the hotspot always exceeds that of the

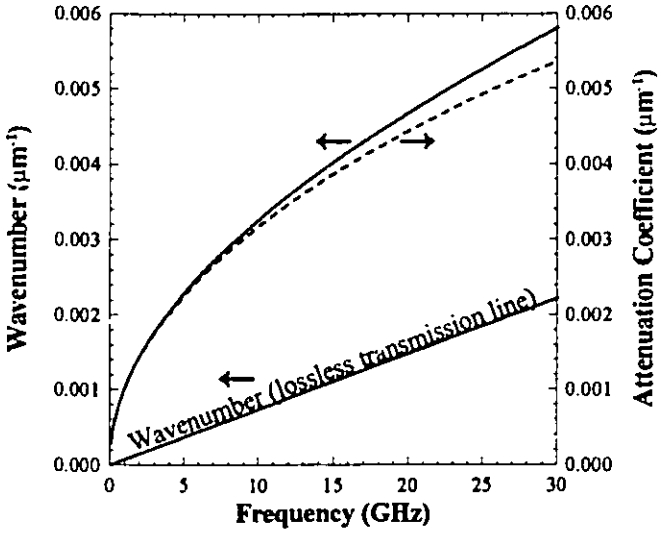

Fig. 5.9. Calculated propagation constant as a function of frequency for a hotspot with a resistance per unit length of 1.4 Ω/μm. The propagation constant is complex. Its real part is the attenuation coefficient, while its imaginary part is the wavenumber. For comparative purposes, the wavenumber of the lossless transmission line with identical dimensions is also shown.

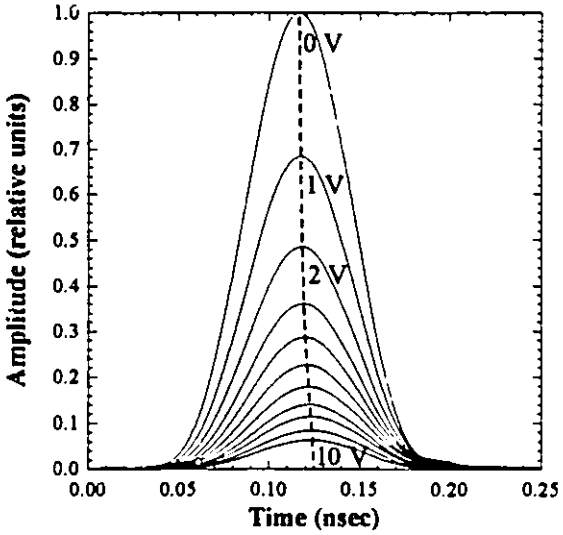

Fig. 5.10. Time domain transmission for the 5 μm wide tapered CPW transmission line for bias voltages from 0 to 10 V.

lossless transmission line. The phase velocity, $v_p = \frac{2\pi f}{\beta}$, is therefore smaller in the hotspot than in the lossless region. Since a larger bias means the hotspot is longer, one would expect the arrival time to be delayed as the bias is increased. Note that the width of the transmitted pulse is not due to dispersion from the device. Rather, the width is caused by the finite bandwidth of the network analyzer.

As was discussed in Section 4.3 on page 47, the total attenuation can be broken down into reflection and absorption components. Figure 5.11 shows these components for three different bias voltages. Most of the attenuation is due to reflection, although absorption becomes dominant at high frequencies and large bias voltages. The reason for this behaviour is evident in Figs. 5.8 and 5.9. Figure 5.8 shows that the characteristic impedance of the hotspot is much larger at lower frequencies. The larger characteristic impedance mismatch results in a larger reflection. Figure 5.9 shows that the attenuation coefficient increases with frequency. The combined effect of reduced reflection and increased attenuation at higher frequencies causes the effects seen in Fig. 5.11. A large reflected component is a disadvantage in sensitive systems which may be damaged by reflected power. However, the advantage of a large reflection is that the switch will be less sensitive to the incident microwave power level. At high microwave power levels, the switch can latch into an OFF state[35] so that even if the DC bias is reduced to zero, the switch will remain off. This latching power is important; it will be increased when more microwave power is reflected.

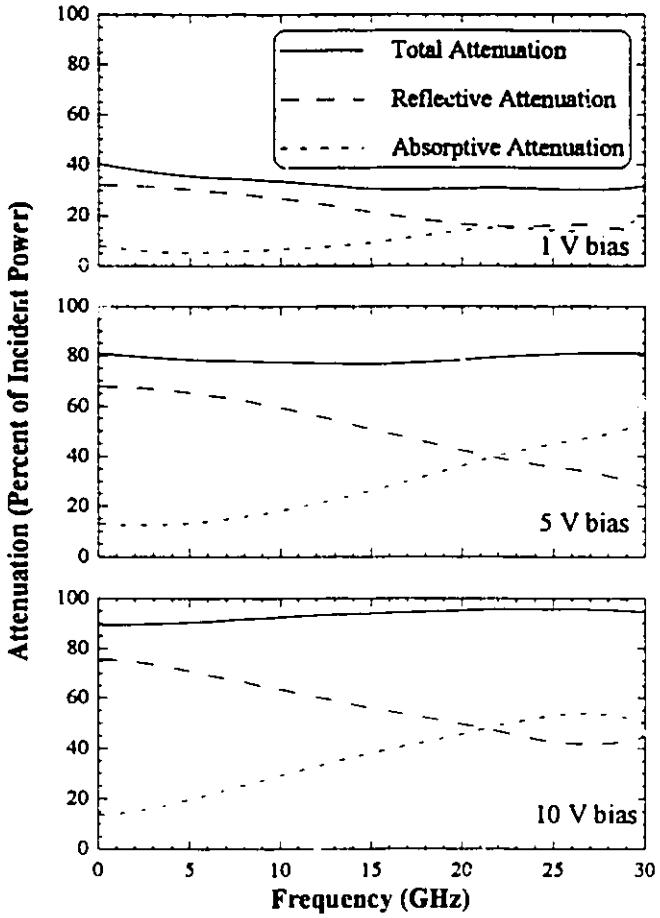

Fig. 5.11. Attenuation versus frequency for three different applied bias voltages. All measurements were made on the tapered CPW circuit with a final center conductor width of 5 μm. The attenuation is broken down into absorption and reflection, and is expressed as a percentage of the incident power level.

Measurements of the transmission coefficient have also been carried out on a sample tapering to a final center conductor width of 10 μm. The distributed loss model was applied to these measurements, with the result shown in Figs. 5.12 and 5.13. Because the width of the bridge was 10 μm rather than 5 μm, the resistance per unit length in the model was set to 0.7 Ω/μm rather than 1.4 Ω/μm. Again, the modelled magnitude and phase agree quite well with measured data. These figures have been plotted on the same scale as Figs. 5.5 and 5.6 to facilitate comparison. The attenuation has been decreased by approximately 4 dB at low frequencies, and the attenuation rolloff at higher frequencies is not as pronounced for the wider device.

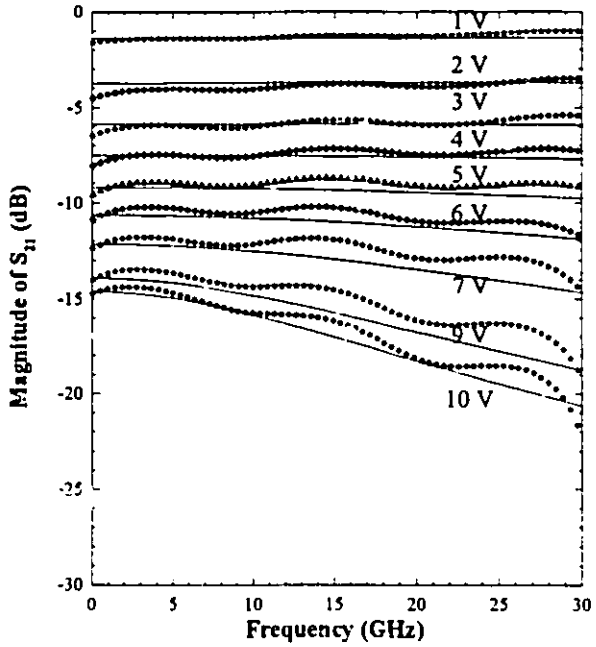

Fig. 5.12. Measured (symbols) and modelled (solid lines) S_{21} magnitude data for a CPW transmission line tapering to a final width of 10 μm. The model uses a capacitance per unit length of 235.67 pF/m, an inductance per unit length of 589 nH/m, and a resistance per unit length of 0.7 Ω/μm.

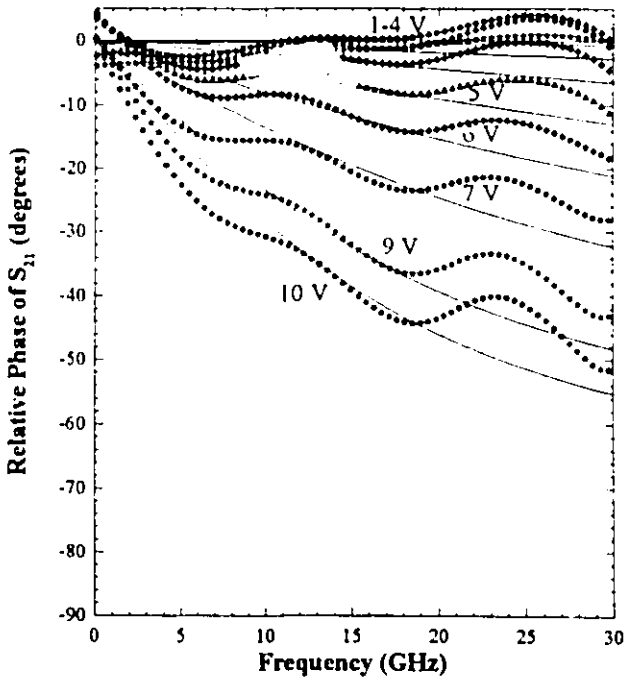

Fig. 5.13. Measured (symbols) and modelled (solid lines) phase data for a CPW transmission line tapering to a final width of 10 μm.

Finally, the model allows us to make predictions for different devices which have not been built. Shown in Fig. 5.14 is the predicted transmission coefficient for a hypothetical tapered CPW device with a final center conductor width of 1 μm and hence a resistance per unit length of 7 Ω/μm . Clearly, one can achieve much greater attenuation as the width of the center conductor is decreased. At 12 GHz, the attenuation will be 50 dB for a 10 V applied bias, compared to 22 dB for a 5 μm wide center conductor and 16 dB for one 10 μm wide. Similar gains could be achieved by decreasing the thickness of the film, decreasing the heat transfer coefficient, or increasing the bath temperature, as discussed in Table 3.1 on page 35.

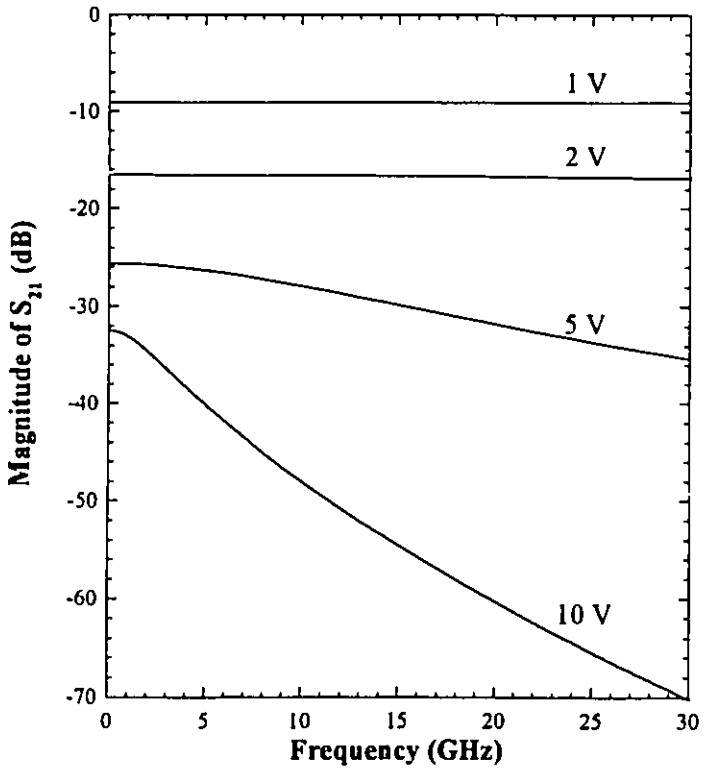

Fig. 5.14. Hypothetical transmission coefficient as a function of frequency for bias voltages of 1, 2, 5, and 10V applied to a tapering CPW transmission line with a final center conductor width of 1 μm. The parameters used in the distributed loss model are C=235.7 pF/m, L=589.25 nH/m, and R=7 Ω/μm.

5.5. Discussion

In this chapter, we have seen that a tapered superconducting CPW device can be used to attenuate microwave signals. The attenuation increases as the bias voltage applied to the device is increased. A typical device with a 5 μm wide center conductor will give an attenuation of approximately 22 dB when a 10V bias is applied. This attenuation is too low for many microwave switching applications. If greater attenuation is required, one can use a larger bias voltage, a narrower center conductor, or a thinner film as shown in Table 3.1 on page 35. Using a larger bias voltage will not damage the device, since it will not result in a temperature increase, but instead will only cause the hotspot to grow in length. However, a larger bias will result in greater DC power consumption. The current will be approximately independent of the voltage, so power consumption will increase linearly with the applied bias. Using a narrower center conductor or a thinner film will increase the attenuation and reduce the power consumption, but both of these changes will reduce the device power handling capacity.

Another technique to increase the device isolation is to cascade several devices in series. This technique is virtually identical to increasing the applied DC bias voltage. Doubling the bias voltage doubles the length of the hotspot, just as cascading two hotspots in series does. In both cases, DC power consumption will also be doubled. At low frequencies when the hotspot can be modelled as a lumped element resistor, cascading is relatively ineffective. Equation 4.20 on page 49 shows that in the lumped element model (valid at low frequencies) doubling the DC resistance only results in approximately a 6 dB increase in isolation. However, at higher frequencies, cascading becomes much more effective. This can be seen in Fig. 5.5 on page 68. At 5 GHz, increasing the applied voltage from 5 to 10 V increases the attenuation from 13.5 dB to 20 dB, an increase of about 6 dB. However, at 25 GHz, the attenuation increases from 14 dB at 5 V to 28 dB at 10 V, and the isolation doubles on a dB scale. The reason for this effect is that attenuation becomes dominant at higher frequencies, and signals are exponentially attenuated with distance. The frequency where cascading becomes more efficient corresponds to the frequency when the lumped element model begins to fail.

An excellent application for the device used as a switch is in receiver protection circuitry. Many satellite systems save weight and volume by using the same antenna for both receiving and transmitting signals. Because large microwave powers are transmitted, even a small reflection from the antenna can damage the sensitive receiver amplifier. A receiver protection switch is often placed between the receiver and the antenna, switched OFF when the satellite is transmitting. The superconducting switch described in this thesis is well suited for this application, since a very low insertion loss in the ON state is required, while only a moderate isolation in the OFF state is necessary.

This device can also be operated as a variable attenuator. The attenuation can be varied continuously from approximately 0 dB in the ON state to its maximum value which will depend on the device geometry. Attenuation is varied by changing the applied DC bias voltage. A viable application of this device is in an automatic gain control circuit. Due to non-linearities in receiver systems, it is desirable to have a constant input power. In a satellite system, received power can vary by as much as 15 dB over the course of a day.[69] The superconducting attenuator is ideal for this application, since fast switching speeds and large attenuation are not required.

It is useful to investigate the performance limitations and tradeoffs involved in using this device. In switching applications, the isolation and insertion loss are probably the most important properties. We have fabricated a device with very low insertion loss and moderate isolation. The isolation can be made arbitrarily large by either increasing the length of the device (and increasing the applied voltage) or by cascading a number of devices in series. Because the hotspot lengthens rather than heating up, there is no danger of damaging the device with large applied voltages. However, both of these techniques will increase the insertion loss and power consumption may become significant. To reduce power consumption, thinning and narrowing of the tapered region can be done. While sub-micrometer lithography has been used with $YBa_2Cu_3O_{7-\delta}$ films, a practical linewidth is probably about 1 μm. Again, as the linewidth is made narrower or the film is made thinner, insertion loss will increase. In addition, the microwave power handling capability of the device will be reduced under these changes.

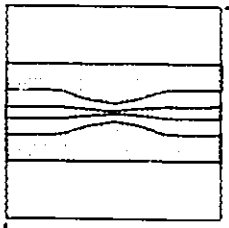

CONCLUSIONS

We have investigated a new thin film superconducting microwave device that can be used as a switch or as a continuously variable attenuator. The device consists of a tapered coplanar waveguide transmission line, and switching from a lossless to a lossy state is achieved by the application of a DC bias voltage.

To understand the nature of the switching mechanism, the behaviour of a DC voltage biased superconducting bridge has been investigated. Under zero bias, the bridge is lossless. However, any finite voltage applied across the bridge results in the formation of a hotspot in which a small region of the bridge heats up above the critical temperature. Since this region is now resistive, the bridge is switched into a lossy state. A thermal model has been developed to explain the steady state hotspot behaviour, and experiments were performed to confirm that the model accurately represents the actual device. The hotspot was found to have a flat-topped temperature distribution, with a temperature independent of the applied bias voltage. The length of the hotspot was found to increase linearly with the applied voltage, so the resistance of the bridge increases linearly with voltage, and the current is constant after switching. The thermal model allows predictions to be made regarding the effect of various changes on the resistance and power dissipation of the bridge in the switched state. To achieve maximum resistance at the lowest possible power dissipation, the bridge should be made as narrow and as thin as possible.

The microwave response of the hotspot has also been investigated, and microwave transmission measurements have been made on a tapered coplanar waveguide transmission line as a function of the applied bias. The attenuation of the device increases with the applied bias voltage, so the device can be used as a voltage controlled variable attenuator. When operated as a switch, the device has a very low ON state insertion loss, and a moderate OFF

state isolation. A typical device with a 5 μm wide bridge has an isolation of 23 dB at 10 GHz and a bias voltage of 10V.

Microwave modelling has been carried out to investigate the behaviour of the hotspot at microwave frequencies. Because the response time of the hotspot to changes in the applied voltage is slow, the microwave resistance is equal to the DC resistance rather than the small signal resistance as one would initially expect. Additionally, the hotspot can be modelled as a pure resistance. Assuming that the hotspot was a simple resistance per unit length, a distributed loss transmission line model was developed that accurately predicted the magnitude and phase of the transmitted signal as a function of DC bias. The model was also used to predict that a 1 μm wide bridge would result in an isolation of 50 dB at 10 GHz for an applied voltage of 10V.

In comparison with a PIN diode, the superconducting switch presented here has a much smaller insertion loss, but also a much lower isolation. Isolation can be increased by narrowing and thinning the bridge, but this also reduces its power handling capacity. The switch is quite amenable to integration with other superconducting components. A key difference between a PIN diode and the superconducting device presented here is that in the OFF state, the diode can be modelled as a capacitance, while our device is purely resistive. This means that the operating bandwidth of our device is inherently wider than that of a diode, since the isolation of a PIN diode decreases with frequency. Because the device relies on heat diffusion, it has a relatively slow switching speed. For this reason, the switch would not be suitable for high speed digital use, but is ideally suited for low power analog signal control applications.

We have concentrated on understanding the physics of operation of the superconducting switch presented in this thesis. We have not attempted to integrate the device into a larger assembly, nor have we looked into using the switch in any configuration other than as a single pole single throw device. This is a natural area to investigate for further work. Using diode based switching elements as a model, a wide variety of superconductor based switching devices should be possible.

Another area of further work would be to investigate a microstrip version of the device presented in this thesis. Microstrip based superconducting switches should also be

achievable, although their operating bandwidth will likely be reduced because there will be impedance mismatches introduced by the narrowed region required so a hotspot can be formed with reasonable power consumption.

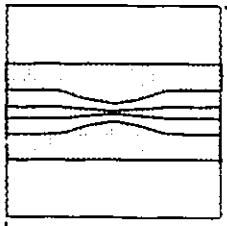

FILM PROCESSING

Considerable effort was devoted to developing processing techniques for patterning the $YBa_2Cu_3O_{7-\delta}$ films for use in the devices of this thesis. Processing was carried out in the CEMD cleanroom facilities at McMaster University using photolithography, modified to pattern the superconducting films. Etching was carried out using citric acid, and nitrogen was continuously bubbled through it, since it has been shown[70] that this etch has minimal effect on film quality. In particular, etching in a nitrogen bubbled citric acid solution has been shown to result in the smallest increase in microwave surface resistance. This is thought to occur because the nitrogen removes any CO_2 in the aqueous solution. Carbon dioxide has been shown[71] to react with $YBa_2Cu_3O_{7-\delta}$ to form insoluble $BaCO_3$ precipitates which are thought to degrade the film quality. A further advantage of citric acid is that it etches very uniformly, so the edges of the film are smooth and the etch is capable of producing submicrometer line widths.

Because the characteristic impedance of coplanar waveguide is a function of both the width and gap of the transmission line, precise knowledge of the undercutting produced during the wet chemical etching was needed. Undercutting will reduce the center conductor width and increase the gap between the center conductor and ground plane, causing large variations in the characteristic impedance of the transmission line. For example, for a 50 Ω CPW line with a width of 5 μm and a gap of 9.2 μm, a 1 μm undercut will change the impedance to 60 Ω which will result in microwave reflections. Three things were done to minimize the effect of undercutting. First of all, a very dilute 0.001M citric acid solution was used, resulting in a slow etch rate. It typically takes 6 minutes to completely etch through the film, so etching will be minimally affected by small timing errors (we previously used an etch that required only 20 seconds to completely remove the film, and timing was much more

critical). The citric acid solution was prepared by dissolving 0.21 grams of crystalline citric acid monohydrate (Scientific Stores part number 80755, molecular weight 210.4) into one litre of deionized water.

Secondly, it was found that etching occurred much more uniformly across the entire film surface if the film was held vertically in the citric acid solution, and rotated slowly during etching. When films were mounted horizontally, etching was much faster along the periphery of the device, and approximately 30% slower at the center. Ensuring uniform etch rates is very important in controlling undercutting. If the etch rate is faster along the periphery of the film, undercutting will be much more severe because the etchant is in contact with the exposed edge of the film for a longer period of time. Finally, to ensure the width and gap were correct after etching, the mask was designed allowing for 2 μm of undercut. All mask features were made 2 μm wider than desired, so that the final, etched film had the correct dimensions. This allowed us to overetch the film somewhat, ensuring its complete removal and precluding the occurrence of any short circuits between the center conductor and ground planes.

In addition to the use of citric acid and a 2 μm mask undercut, several other new procedures were developed in the processing steps listed above. The temperature of both the soft and hard bakes was reduced to minimize possible interaction between the photoresist and the $YBa_2Cu_3O_{7-\delta}$ film. Reducing the temperature also made the photoresist much easier to remove with acetone. The plasma etcher was used for film cleaning. It produced extremely clean film surfaces, resulting in improved etch uniformity. Finally, depositing a thin silver coating prior to the gold was found to improve contact adhesion dramatically. With the Ag/Au deposition, the contacts could withstand ultrasonic cleaning even with no post annealing. Post annealing was not used in processing, since the contact resistance was sufficiently low immediately following deposition to make its use unnecessary.

The following procedure summarizes all of the processing steps developed over the past two years.

Etching.

1. Clean the samples in the ultrasonic cleaner using organic solvents. Cleaning is done for 5 minutes each in acetone, acetone, methanol, acetone, methanol.
2. Mount samples onto glass disks for handling using crystal bond.
3. Clean the sample in the O_2 plasma etcher at 100 W for 3 minutes.
4. Spin Shipley photoresist (S1808) onto samples at 5000 RPM for 30 seconds.
5. Air dry for 5 minutes, then soft bake the photoresist for 2 minutes at 90°C.
6. Expose the photoresist at 9.4 mW/cm^2 for 6 seconds.
7. Develop the photoresist in MF-319 developer for 30 seconds.
8. Rinse the film in DI water then blow dry.
9. Inspect the film, mechanically removing any edge beads if necessary.
10. Hard bake the remaining photoresist for 2 minutes at 110°C.
11. Etch the film in a N_2 bubbled 0.001 M citric acid solution for 6 minutes or until the film clears, then rinse with N_2 bubbled DI water.
12. Inspect the films to ensure complete etching, then remove the photoresist by soaking for 5 minutes in acetone. Spray rinse with acetone, then methanol.
13. Remove any residual photoresist by cleaning in the O_2 plasma etcher at 100W for 3 minutes.

Metallization.

1. Spin Shipley photoresist (S1808) onto samples at 5000 RPM for 30 seconds.
2. Air dry the photoresist for 5 minutes.
3. Soft bake the photoresist for 1 minute at 80°C.
4. Expose the photoresist for 1 minute at 9.4 mW/cm^2.
5. Harden the photoresist by immersing in toluene for 6 minutes, then blow dry.
6. Develop the photoresist for 1.5 minutes in MF319 developer.

7. Inspect the openings to ensure complete photoresist removal over the contact pads, then etch for 30 seconds in a 0.001M, N_2 bubbled citric acid solution. Rinse in N_2 bubbled DI water then blow dry.

8. Evaporate 1000Å silver, then 3000Å gold onto the films. Lift off the photoresist in acetone, leaving metal only over the contact pads.

9. Remove any residual photoresist by cleaning in the O_2 plasma etcher at 100W for 3 minutes.

10. (Optional) Anneal the contacts in flowing oxygen for 45 minutes at 400°C.

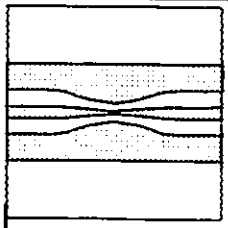

REFERENCES

1. J.C. Ritter, M. Nisenhoff, G. Price, and S.A. Wolf, "High Temperature Superconductivity Space Experiment (HTSSE)", IEEE Trans. Magn. **27**, 2533 (1991).

2. S.H. Talisa, M.A. Janocko, C.M. Moskowitz, J. Talvacchio, J.F. Billing, R. Brown, D.C. Buck, C.K. Jones, B.R. McAvoy, G.R. Wagner, and D.H. Watt, "Low and High Temperature Superconducting Microwave Filters", IEEE Trans. Microwave Theory Tech , **39**, 1448 (1991).

3. R. R. Mansour and V. Dokas, "C-Band Externally Equalized Superconductive Input Channel Filters", IEEE MTT-S Digest, 187 (1994).

4. S. Ye and R. R. Mansour, "Design of Manifold Coupled Multiplexers using Superconductive Lumped Element Filters", IEEE MTT-S Digest, 191 (1994).

5. Nathan Newman and W. Gregory Lyons, "High Temperature Superconducting Microwave Devices: Fundamental Issues in Materials, Physics, and Engineering", J. Supercond. **6**, 119 (1993).

6. Richard W Ralston, "Microwave Applications of Superconducting Electronics", Supercond. Sci. Tech. **4**, 386 (1991).

7. The first low loss narrowband HTS filters were demonstrated in HTSSE I in January of 1990. These results were later published in W.G. Lyons, R.R. Bonetti, A.E. Williams, P.M. Mankiewich, M.L. O'Malley, J.M. Hamm, Alfredo C. Anderson, R.S. Withers, A. Meulenberg, and R.E. Howard, "High T_c Superconductive Microwave Filters", IEEE Trans. Magn. **27**, 2537 (1991), Michael S. Schmidt, Robert J. Forse, Robert B. Hammond, Michael M. Eddy, and William L. Olson, "Measured Performance at 77K

of Superconducting Microstrip Resonators and Filters", IEEE Trans. Microwave Theory Tech. **39**, 1475 (1991), and H.S. Newman, D.B. Chrisey, J.S. Horwitz, B.D. Weaver, and M.E. Reeves, "Microwave Devices Using $YBa_2Cu_3O_{7-\delta}$ Films Made by Pulsed Laser Deposition", IEEE Trans. Magn. **27**, 2540 (1991).

8. G.L. Matthaei and G.L. Hey-Shipton, "High Temperature Superconducting 8.45 GHz Bandpass Filter for the Deep Space Network", IEEE MTT-S Digest, 1273 (1993).

9. Joseph M. Madden, "Practical High Temperature Superconductor Filters", Microwave Journal, **37**, 100 (October, 1994).

10. L.E. Amatuni, K.Y. Constantinian, A.A. Hakhumian, R.B. Hayrapetian, R.M. Martirossian, Kiejin Lee, and G. Park, "Microwave Mixing and Generation in the Low T_C and High T_C Superconducting Thin Film Bridges", Supercond. Sci. Technol. **5**, 107 (1992).

11. M. Lindgren, M.A. Zorin, V. Trifonov, M. I anerud, D. Winkler, B.S. Karasik, G.N. Gol'tsman, and E.M. Gershenzon, "Optical Mixing in a Patterned $YBa_2Cu_3O_{7-\delta}$ Thin Film", Appl. Phys. Lett. **65**, 3398 (1994).

12. G.C. Liang, R.S. Withers, B.F. Cole, S.M. Garrison, M.E. Johansson, W.S. Ruby, W.G. Lyons, "High Temperature Superconducting Delay Lines and Filters on Sapphire and Thinned $LaAlO_3$ Substrates", IEEE Trans. Appl. Supercond., **3**, 3037 (1993).

13. N.O. Fenzi and D.L. Aidnik, "An HTS 100 Nano-Second Delay Line", To be published in IEEE Trans. Appl. Supercond., June, 1995.

14. Ben G. Streetman, *Solid State Electronic Devices*, Second Edition, Prentice-Hall, Englewood Cliffs, NJ., 1980, pp. 173-176.

15. David M. Pozar, *Microwave Engineering*, Addison-Wesley, Reading, Mass., 1990, pp. 639-646.

16. J.S. Martens, V.M. Hietala, T.E. Zipperian, D.S. Ginley, C.P. Tigges, and G.K.G. Hohenwarter, "A Reflective Microwave Switch Made of Tl-Ca-Ba-Cu-O for Signal

Control Applications", IEEE Microwave and Guided Wave Letters, **10**, 291 (1991).

17. Neal O. Fenzi, Kurt F. Raihn, George V. Negrete, Edward R. Soares, and George L. Matthaei, "An Optically Switched Bank of HTS Bandstop Filters", IEEE MTT-S Digest, 195 (1994).

18. H.K. Onnes, Comm. Physical Lab., Univ. of Leiden, Suppl. 34b (1911).

19. J.G. Bednorz and K.A. Müller, "Possible High T_C Superconductivity in the Ba-La-Cu-O System", Z. Phys. B **64**, 189 (1986).

20. M.K. Wu, J.R. Ashburn, C.J. Torng, P.H. Hor, R.L. Meng, L. Gao, Z.J. Huang, Y.Q. Wang, and C.W. Chu, "Superconductivity at 93K in a New Mixed Phase Y-Ba-Cu-O Compound System at Ambient Pressure", Phys. Rev. Lett., **58**, 908 (1987).

21. A good overview of the various applications of High T_C materials can be found in J.D. Doss, *Engineer's Guide to High Temperature Superconductivity*, John Wiley & Sons, New York, 1989.

22. F. London, *Superfluids*, Vol. 1, John Wiley & Sons, New York, 1950.

23. This analysis follows the analysis presented in the excellent book, T.P. Orlando and K.A. Delin, *Foundations of Applied Superconductivity*, Addison-Wesley, Reading, Mass., 1991.

24. See either N.W. Ashcroft and N.D. Mermin, *Solid State Physics*, Saunders College, Philadelphia, 1976, or C. Kittel, *Introduction to Solid State Physics*, 5th ed., John Wiley & Sons, New York, 1976.

25. T.P. Orlando and K.A. Delin, *Foundations of Applied Superconductivity*, Addison-Wesley, Reading, Mass., 1991, pp 60-66.

26. A.B. Pippard, "The Surface Impedance of Superconductors and Normal Metals at High Frequencies, Part III.: The Relation between Impedance and Superconducting Penetration Depth", Proc. Royal Soc. London A, **191** (1947).

27. F. Gao, J.W. Kruse, C.E. Platt, M. Feng, and M.V. Klein, "Microwave Surface Impedance at 10 GHz and Quasiparticle Scattering in $Y_1Ba_2Cu_3O_{7-\delta}$ Films", Appl. Phys. Lett. **63**, 2274 (1993).

28. W. Rauch, E. Gornik, G. Sölkner, A.A Valenzuela, F. Fox, and H. Behner. "Microwave Properties of $YBa_2Cu_3O_{7-\delta}$ Thin Films Studied with Coplanar Transmission Line Resonators", J. Appl. Phys. **73**, 1866 (1993).

29. David M. Pozar, *Microwave Engineering*, Addison-Wesley, Reading, Mass., 1990, Chapter 2.

30. D.A. Bonn, K. Zhang, R. Liang, D.J. Baar, D.C. Morgan, and W.N. Hardy, "Oxygen Vacancies, Zinc Impurities, and the Intrinsic Microwave Loss of $Y_1Ba_2Cu_3O_{7-\delta}$", Journal of Superconductivity, **6**, 219 (1993).

31. E.H. Brandt, "The Flux-Line Lattice in High T_C Superconductors", Journal of Superconductivity, **4**, 201 (1993).

32. Daniel S. Fisher, Matthew P.A. Fisher, and David A. Huse, "Thermal Fluctuations, Quenched Disorder, Phase Transitions, and Transport in Type II Superconductors", Phys. Rev. B, **43**, 130 (1991).

33. C. Dekker, W. Eidelloth, R.H. Koch, "Measurement of the Exponent μ in the Low Temperature Phase of $YBa_2Cu_3O_{7-\delta}$ Films in a Magnetic Field: Direct Evidence for a Vortex-Glass Phase", Phys. Rev. Lett., **68**, 3347 (1992).

34. J.W. Bremmer and V.L. Newhouse, "Thermal Propagation Effects in Thin Superconducting Films", Phys. Rev. Lett. **1**, 282 (1958).

35. W.J. Skocpol, M.R. Beasley, and M. Tinkham, "Self-Heating Hotspots in Superconducting Thin Film Microbridges", J. Appl. Phys., **45**, 4054 (1974).

36. G. Darcy Poulin, Jean Lachapelle, Steven H. Moffat, Frank A. Hegmann, and John S. Preston, "Current-Voltage Characteristics of DC Voltage Biased High Temperature Superconducting Microbridges", Appl. Phys. Lett., **66**, 2576 (1995).

37. For a good discussion of heat transfer analysis in superconducting films, see appendix B of Frank Hegmann, *Picosecond Photoresponse of High T_C Superconductor Thin Films*, PhD Thesis, McMaster University (1994).

38. S.J. Hagen, Z.Z. Wang, and N.P. Ong, "Anisotropy of the Thermal Conductivity of $YBa_2Cu_3O_{7-\delta}$", Phys. Rev. B, **40**, 9389 (1989).

39. The heat transfer coefficient is approximated as the inverse of the thermal boundary resistance, giving estimates for the heat transfer coefficient of between 300 and 1250 $Wcm^{-2}K^{-1}$. See C.D. Marshall, A. Tokamoff, I.M. Fishman, C.B. Eom, J.M. Phillips, and M.D. Fayer, J. Appl. Phys. **73**, 850 (1993) or M. Nahum, S. Verghese, P.L. Richards, and K. Char, Appl. Phys. Lett. **59**, 2034 (1991).

40. J.M. Valles, Jr., A.E. White, K.T. Short, R.C. Dynes, J.P. Garno, A.F.J. Levi, M. Anzlowar, and K. Baldwin, "Ion Beam Induced Metal Insulator Transition in $YBa_2Cu_3O_{7-\delta}$: A Mobility Edge", Phys. Rev. B, **39**, 11599 (1989).

41. Simon Ramo, John R. Whinnery, and Theodore Van Duzer, *Fields and Waves in Communication Electronics*, Third Edition, Wiley, New York, NY., 1993, Chapter 4.

42. David M. Pozar, *Microwave Engineering*, Addison-Wesley, Reading, Mass., 1990, pp. 205-212.

43. David M. Pozar, *Microwave Engineering*, Addison-Wesley, Reading, Mass., 1990, pp. 76-79.

44. David M. Pozar, *Microwave Engineering*, Addison-Wesley, Reading, Mass., 1990, pp. 220-231.

45. F.L. Warner, *Microwave Attenuation Measurement*, Peter Peregrinus Ltd., Herts., England, 1977, Chapter 2.

46. David M. Pozar, *Microwave Engineering*, Addison-Wesley, Reading, Mass., 1990, pp. 107-114.

47. Robert Collin, *Field Theory of Guided Waves*, McGraw-Hill, New York, NY., 1960, pp. 124-132.

48. David M. Pozar, *Microwave Engineering*, Addison-Wesley, Reading, Mass., 1990, pp. 231-244.

49. David M. Pozar, *Microwave Engineering*, Addison-Wesley, Reading, Mass., 1990, pp. 16-19.

50. E.K. Hollmann, O.G. Vendik, A.G. Zaitsev, and B.T. Melekh, "Substrates for High T_c Superconductor Microwave Integrated Circuits", Supercond. Sci. Technol. 7, 609 (1994).

51. Brian C. Wadell, *Transmission Line Design Handbook*, Artech House, Norwood, Mass., 1991, pp. 437.

52. Brian C. Wadell, *Transmission Line Design Handbook*, Artech House, Norwood, Mass., 1991, pp. 74.

53. C.H. Edwards, Jr. and D.E. Penney, *Calculus and Analytic Geometry*, Prentice-Hall, Englewood Cliffs, N.J., 1982, pp. 547-554.

54. David M. Pozar, *Microwave Engineering*, Addison-Wesley, Reading, Mass., 1991, pp. 184-185.

55. G. Ghione and C. Naldi, "Analytical Formulas for Coplanar Lines in Hybrid and Monolithic MICs", Electronics Letters, **20**, pp. 179-181 (1984).

56. Brian C. Wadell, *Transmission Line Design Handbook*, Artech House, Norwood, Mass., 1991, pp. 73-92.

57. T. Van Duzer and C.W. Turner, *Principles of Superconductive Devices and Circuits*, Elsevier, N.Y., 1981, pp. 31-34.

58. H.H. Shigesawa, M. Tsuji, and A.A. Oliner, "Conductor-Backed Slotline and Coplanar Waveguide: Dangers and Full Wave Analysis", IEEE MTT-S Digest, 199 (1988).

59. C.C. Cheng, C-K.C. Tzuang, S.T. Peng, and C-C. Chang, "Transmission Characteristics of Finite Width Conductor Backed Coplanar Waveguide", IEEE Trans. Microwave Theory Tech., **41**, 1616 (1993).

60. Nirod K. Das, "Two Conductor-Backed Configurations of Slotline or Coplanar Waveguide for Elimination or Suppression of the Power Leakage Problem", IEEE MTT-S Digest, 153 (1994).

61. Yaozhong Liu and Tatsuo Itoh, "Leakage Phenomena in Multilayered Conductor-Backed Coplanar Waveguide", IEEE Microwave and Guided Wave Lett., **3**, 426 (1993).

62. Mark A. Magerko, Lu Fan, and Kai Chang, "Multiple Dielectric Structures to Eliminate Moding Problems in Conductor Backed Coplanar Waveguide MIC's", IEEE Microwave and Guided Wave Lett., **2**, 257 (1992)

63. Microwave absorbing foam (part number MTLF-22) was purchased from Microsorb Technologies Inc., Hopefield, Mass.

64. Wiltron K-connectors™ are coaxial connectors designed to operate from DC to 40 GHz with a return loss greater than 20 dB over the entire frequency range. Full details regarding the connector can be found in the Wiltron catalogue.

65. The coaxial connectors (Wiltron Part # SCK120MF) were specially ordered with a male connector on one end and a female connector on the other end so they could connect the test set cables to the K-connectors™. The coaxial cable has a TM mode cutoff frequency of 42 GHz, so it is compatible with the 40 GHz K-connector™, operating in a pure TEM mode to 42 GHz.

66. CPW calibration standards have been fabricated at NIST, but they are not generally available. See Don C. DeGroot, "Tunable Microwave Properties of YBCO/$SrTiO_3$ Thin Film Transmission Lines", to be published in June, 1995 issue of IEEE Trans. Appl. Supercond.

67. J. Lachapelle, *The Resistive Hotspot in Superconducting Thin Films*, Master's Thesis, McMaster University, Hamilton, Ontario, Canada, 1995.

68. Brian C. Wadell, *Transmission Line Design Handbook*, Artech House, Norwood, Mass., pp. 99.

69. Private communication, Tony Romano, COM DEV.

70. D.S. Ginley, C.I.H. Ashby, T.A. Plut, D. Urea, M.P. Siegal, and J.S. Martens, "Di- and Tricarboxylic Acid Based Etches for Processing High Temperature Superconducting Thin Films", Appl. Phys. Lett., **63**, 2429 (1993).

71. Carol I.H. Ashby, Jon Martens, Thomas A. Plut, David S. Ginley, and Julia M. Phillips, "Improved Aqueous Etchant for High T_c Superconductor Materials", Appl. Phys. Lett., **60**, 2147 (1992).

Patent Application

"Voltage Controlled Superconducting Microwave Switch
and Method of Operation Thereof"

G. Darcy Poulin, Frank A. Hegmann, Steven H. Moffat, and John S. Preston

Summary:

The following patent was applied for in October of 1994 and was assigned to COM DEV. The patent describes fundamental features of the microwave switch described in this thesis.

Voltage Controlled Superconducting Microwave Switch and Method of Operation Thereof

Inventors: Darcy Poulin, Frank Hegmann, Steven Moffat, and John Preston, all of Hamilton, Ontario, Canada.

Assignee: COMDEV Inc., Cambridge, Ontario, Canada.

ABSTRACT

A low insertion loss, wide bandwidth, microwave switch comprises a superconducting transmission line that can reversibly go from a superconducting state to a normal state by the application of a DC voltage. When in the normal state, the switch is `OFF' and microwave signals are attenuated. To reduce the voltage necessary to cause switching, the width of the transmission line is decreased. This decrease is done in a controlled manner so that there are no spurious reflections produced on the line, resulting in a wide operating bandwidth.

BACKGROUND OF THE INVENTION

1. Field of the Invention

The invention relates to a microwave switch comprising a microwave transmission line constructed in such a way so it can go reversibly from a superconducting (`ON') state to a normal (`OFF') state. A switch of this type can be advantageously applied, for example, as part of a microwave phase shifter, as a redundancy switch in a satellite communications system, or as a microwave attenuator.

The characteristics of a microwave switch are:

the bandwidth of its operation;

the extent of losses due to the presence of the switch in the transmission line in the `ON' state, and the isolation when in the `OFF' state;

its switching time between the `ON' state and the `OFF' state;

its power consumption;

its power handling capability and long term stability.

2. Description of the Prior Art

Many microwave switches employ PIN diodes as the switching device. When forward biased, a PIN diode behaves like an `ON' switch, and when reverse biased, it appears like an `OFF' switch. However, the PIN diode introduces a series resistance when mounted on a transmission line, and its maximum power handling capability is limited by the value of the avalanche voltage of the diode. Finally, PIN diodes may be difficult to integrate with superconducting circuits.

It is known that superconductors can be switched from the superconducting to the normal state (in non microwave applications) using an applied current. While the switching mechanism is similar to that disclosed in this patent, the use of a constant current source rather than a constant voltage source to control switching results in higher power dissipation and a greater risk of damage to the superconductor in the `OFF' state.

There are several ways in which superconductors are used for microwave switches. Some versions vary the temperature of the entire switching region using an external means such as a heater or a light source. This approach typically leads to slow switching speeds and increased complexity. Others have used applied magnetic fields to decrease the critical temperature of the superconductor below the temperature of the cryogen. Still others use current pulses to switch the superconductor to the normal state, and rely on resonant structures to provide adequate isolation. This approach inherently limits the bandwidth of the switch.

SUMMARY OF THE INVENTION

It is the object of the present invention to provide a superconducting microwave switch that has a wide operating bandwidth, and low overall insertion loss. It is another object of the invention to provide a microwave switch that is voltage controlled. It is still another object of the invention to provide a superconducting switch that may be interconnected on integrated circuits with other superconducting circuits.

The invention can be summarized as a single superconducting microwave transmission line that can be switched from the `ON' state to the `OFF' state by the application of an appropriate DC voltage. The size of the voltage required to switch the line to the `OFF' state is preferably reduced by decreasing the width of the transmission line. The width is reduced in such a manner so that no spurious reflections are produced in the transmission line, resulting in a wide operating bandwidth.

BRIEF DESCRIPTION OF THE DRAWINGS

The accompanying drawings illustrate several aspects of the present invention, and with the description serve to explain the principles of the present invention. In the drawings:

FIG. 1 is a top view of the microwave switch, with the DC control lines shown schematically.

FIG. 2 is a bottom view of the microwave switch.

FIG. 3 is a typical current versus voltage (IV) curve for the structure shown in FIG. 1, with DC load lines shown as an aid in determining the operating point of the device.

DETAILED DESCRIPTION OF THE PREFERRED EMBODIMENTS

FIG. 1 shows a top view of the switch 1 according to the present invention. The switch 1 is a 50 Ohm coplanar waveguide transmission line 5 comprising a superconducting film 11 on an insulating substrate 10. The characteristic impedance of the transmission line 5 is controlled by the width of the center conductor 2, by the width of the gap 3 between the center conductor 2 and the adjacent ground planes 4, and by the thickness and dielectric constant of the substrate 10. Superconducting ground planes 4 are present adjacent to the gap 3, and may also be present on the back side of the insulating substrate 10 , shown as 14 in FIG. 2. The transmission line 5 is normally in the `ON' state, until the DC voltage source 9 is enabled, causing a DC current to flow through the center conductor 2. To ensure that a relatively small voltage will be sufficient to cause switching of the transmission line 5, center conductor 2 is gradually tapered down to a much smaller width 6. To maintain a characteristic impedance of 50 Ohms throughout the transmission line 5, the gap 3 is reduced accordingly to 7, and the ground plane width 4 is therefore increased to 8. The exact width of the center conductor 6 and of the gap 7 yielding a characteristic impedance of 50 Ohms are determined for substrate 10 of known thickness and dielectric constant in articles by Ghione and Naldi entitled "Parameters of Coplanar Waveguides with Lower Groundplane" appearing in Electronics Letters, Volume 19, 1983, at pages 734-735, and "Analytical Formulas for Coplanar Lines in Hybrid and Monolithic MICs" appearing in Electronic Letters, Volume 20, 1984, at pages 179-181. The center conductor 2 of the switch 1 must be a superconducting film such as $Y_1Ba_2Cu_3O_7$. The ground planes 4, and the ground plane 14 that may be present on the back side of the insulating substrate 10, are preferably of the same material as the center conductor 2, but the device will function (with increased insertion losses) provided any conductor is used. The biasing voltage source 9 is connected to the center conductor 2 through an optional bias resistor 12. The connection of the bias voltage source 9 and bias resistor 12 is shown only schematically in FIG. 1. The connection is made with minimal perturbation of the microwave transmission line 5 by using a bias-tee 13.

FIG. 3 shows the switching characteristic of a typical device patterned as shown in FIG. 1. The IV curve 20 shows the current as a function of the device voltage. The term `device voltage' refers to the actual voltage appearing across the switch. The term `applied voltage' refers to the voltage set on the biasing voltage source 9. The current increases rapidly with very small device voltage, until the critical current 25 is reached, and a small resistance appears across the film for further increases in the device voltage. As the device voltage continues to increase, the resistance of the film further increases until the thermal switching current 26 is reached when the current abruptly decreases to 27 and the film resistance abruptly increases. Further increases in the device voltage result in little change in the current. This current remains approximately constant until a much larger voltage (not shown in FIG. 3) when the current again increases. Also shown in FIG. 3 are two load lines, 21 and 22, which determine the DC operating point with a 20 Ohm bias resistor for two different applied voltages 9. For a 0.75 Volt applied voltage, load line 21 applies, and the current level will be 29. For a 1.8 Volt applied voltage, load line 22 applies, the thermal switching current has been exceeded, and the device has switched to 31. Load line 24 is a load line that would apply if a constant current source was used to bias the device. In this case, the device voltage in the switched state, if attainable without permanent damage occuring, would be 32, and much greater power (given by the product of the current and the voltage) would be dissipated in the device. Voltage biasing results in safer switch operation since power dissipation levels are controllable and are greatly reduced. Additionally, by reducing the value of the load resistance 12 towards zero, power dissipation in the switched state is minimized.

It is believed that the slightly increased resistance between currents 25 and 26 is due to flux creep. This effect is described by Anderson in "Theory of Flux Creep in Hard Superconductors", appearing in Physical Review Letters, Volume 9, 1962, pages 309-311. The onset of a large resistance when the current drops abruptly from 26 to 27 is believed to occur when the temperature of a short region in the tapered section 6 of the center conductor suddenly rises above the critical temperature of the superconductor. When this `hot spot' is present, the device is in the `OFF' state, and the

current through the center conductor 2 is reduced. Since the resistance associated with the `hot spot' is large, it continues to dissipate power, and is therefore a stable region. Microwave energy is also absorbed in this region, leading to decreased microwave transmission through the device when in the `OFF' state. When the applied DC voltage 9 is reduced to zero, the `hot spot' disappears, the switch turns `ON', and the microwave signal is transmitted with minimal attenuation.

We have observed that the microwave attenuation can be continuously adjusted by changing the applied voltage. For zero applied voltage, the attenuation is approximately zero. For larger applied voltages, after the current reaches the thermal switching current 26, a `hot spot' develops, the current decreases, and microwave signals are attenuated. Microwave attenuation increases as the applied voltage is further increased, with the ultimate limit governed by the maximum allowable power dissipation of the superconducting film 11.

In the preferred embodiment of FIG. 1, the signal carrying center conductor 2 of the transmission line tapers down in width to reduce the required applied voltage 9 necessary to attain the thermal switching current 26. However, it will be readily apparent to those skilled in the art that this applied voltage can also be reduced by decreasing the thickness of the superconducting film 11, by increasing the temperature so the operating temperature is closer to the critical temperature, by selectively irradiating a portion of the film with an ion beam, or by any combination of these techniques. Additionally, the technique disclosed herein is not limited to a coplanar waveguide configuration. Other superconducting planar transmission lines including microstrip and stripline can also be employed for switching, if the applied voltage necessary to induce switching is sufficiently small to be practical. For microstrip and stripline circuits, the signal carrying conductors for 50 Ohm systems are relatively wide, so impractically large applied voltages would be required. These types of transmission lines would require ion beam irradiation or operation at temperatures closer to the critical temperature for practical use.

The embodiments of the invention in which an exclusive property or privilege is claimed are defined as follows:

1. A low insertion loss, wide bandwidth superconducting microwave switch having an input and an output comprising:

a microwave transmission line comprising a superconducting film on an insulating substrate capable of reversibly going from a superconducting state to a normal state by the application of a DC voltage;

said DC voltage applied to the signal carrying conductor of said transmission line, in series with an optional bias resistor and a bias-tee.

2. A superconductong switch as in claim 1 with said transmission line in a coplanar waveguide configuration;

said coplanar waveguide having a tapering center conductor and a decreasing spacing between the center conductor and the adjacent ground planes, reducing the voltage necessary to effect switching while decreasing spurious reflections to maintain a wide operating bandwidth.

3. A superconducting switch as in claim 1, where said transmission line is non-tapering coplanar waveguide, microstrip, or stripline, and the switching voltage is decreased to a practical value by ion beam irradiation of the signal carrying conductor of said transmission line or by operation at temperatures close to the critical temperature of the superconductor.

4. A superconducting switch as in claim 1, 2, or 3, where the signal carrying conductor is a superconductor, and the ground plane is a metal.

5. A superconducting switch as in claim 1, 2, or 3 where the superconductor is $Y_1Ba_2Cu_3O_7$, and the insulating substrate is $LaAlO_3$.

6. A superconducting switch as in claim 2, where the center, signal carrying conductor tapers from a width of 150 μm to a width of 10 μm, the gap between the center conductor and the adjacent ground planes tapers from 525 μm to 18 μm, and the thickness of the $LaAlO_3$ insulating substrate is 508 μm.

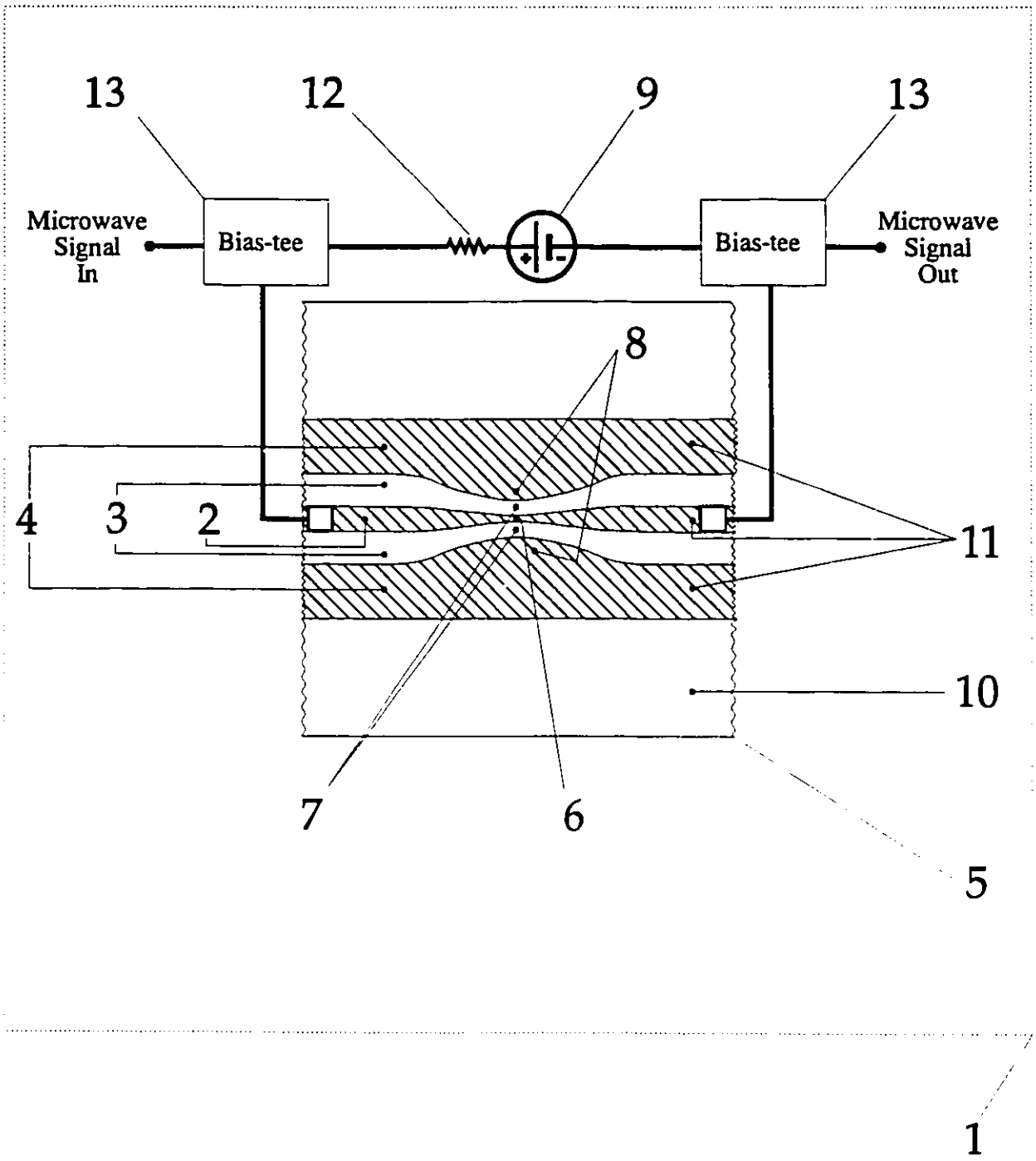
13
12
9
13
Microwave Signal In
Bias-tee
Bias-tee
Microwave Signal Out
8
4
3
2
11
10
7
6
5
1

Figure 1

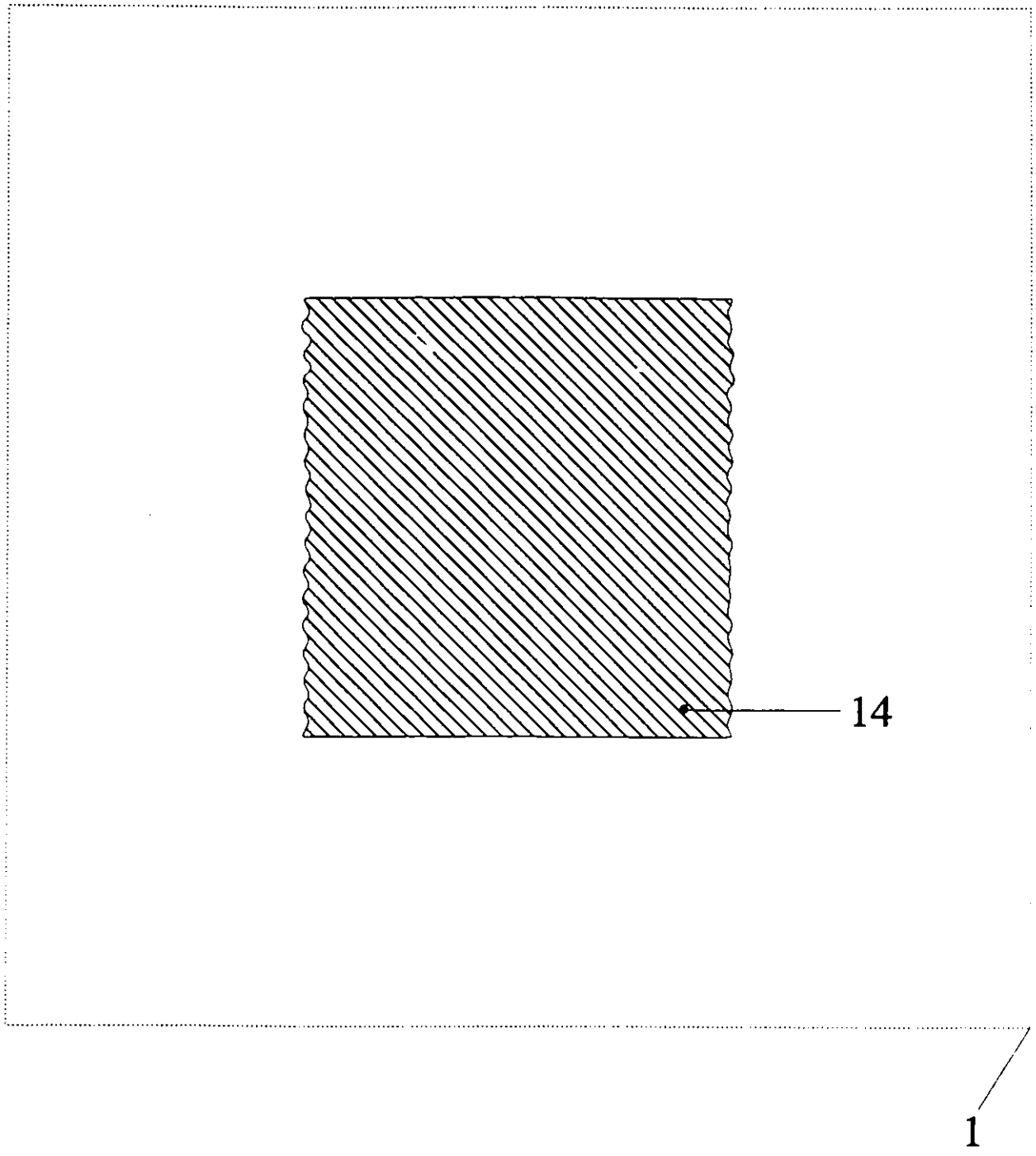

Figure 2

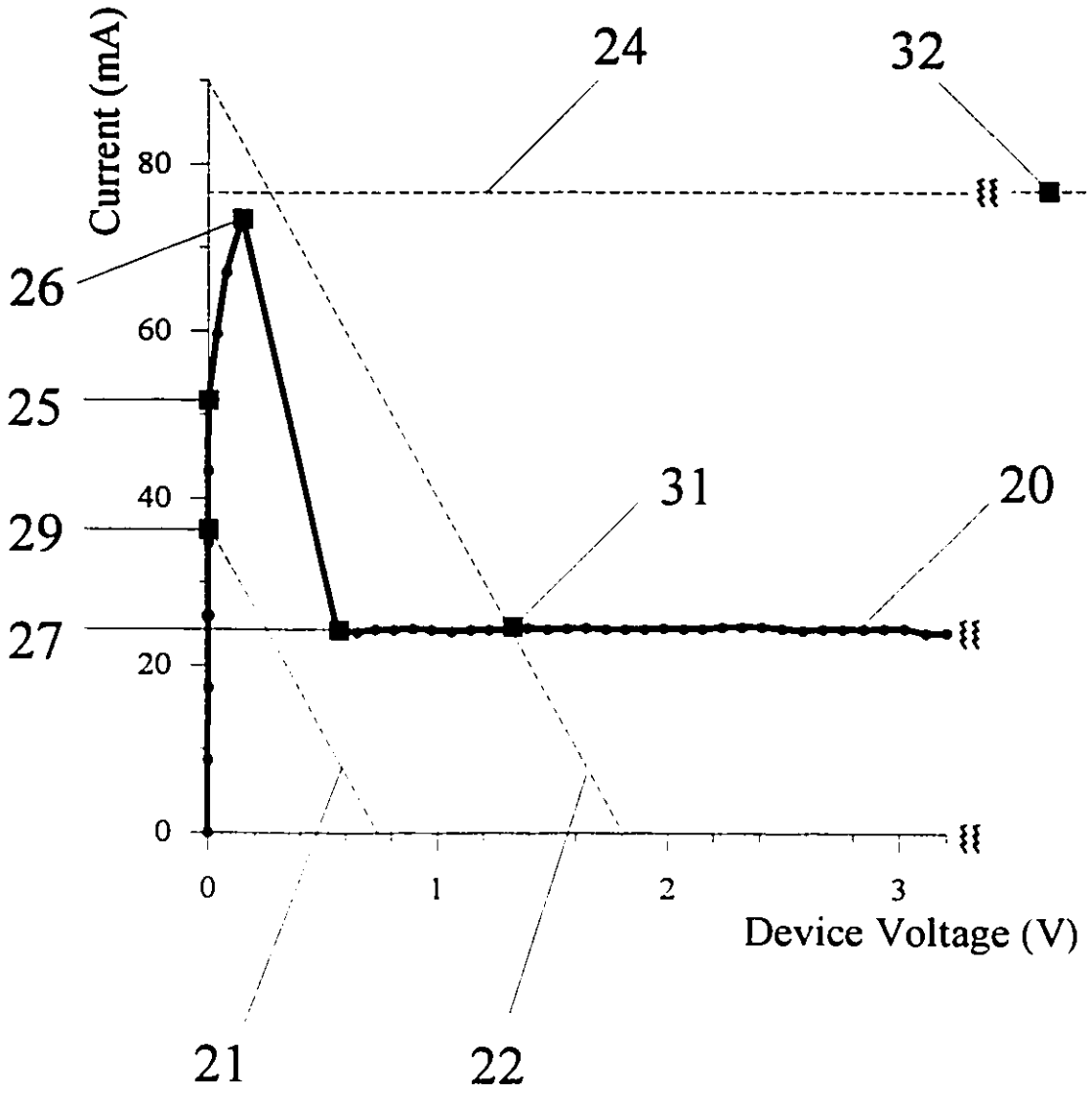
Current (mA)
80
60
40
20
0
0
1
2
3
Device Voltage (V)
24
32
26
25
29
27
31
20
21
22

Figure 3

Paper A

"A Superconducting Microwave Switch"

G. Darcy Poulin, Frank A. Hegmann, Jean Lachapelle,
Steven H. Moffat, and John S. Preston.
IEEE Trans. Appl. Supercond., **5**, 3046 (1995).

Summary:

This paper was presented in October 1994 at the Applied Superconductivity Conference in Boston, Mass. The paper was presented as a poster, and was published in the conference proceedings after standard refereeing. The paper described the main features of the switch, although a complete understanding of the microwave response had not yet been developed, nor was the nature of the hotspot completely understood.

A Superconducting Microwave Switch

G. Darcy Poulin, Frank A. Hegmann, Jean Lachapelle, Steven H. Moffat, John S. Preston
Dept. of Engineering Physics, McMaster University, Hamilton, Ontario, L8S-4L7

Abstract–We describe a superconducting microwave switch. The switch comprises a tapering microwave transmission line which can be switched from a very low loss ON state to a high impedance OFF state with a DC voltage applied to the transmission line through a bias-tee. Switching is essentially thermal in nature, occurring due to the formation of a 'hot spot' in the transmission line. Thermal runaway is avoided through the use of voltage rather than current biasing. Once switched, the transmission line attenuates the applied microwave signal. An isolation of 20 dB is readily achievable. The intrinsic response time of the hot spot to applied microwave fields was estimated to be approximately 1 μs by measuring the frequency dependence of the transmitted signal.

I. INTRODUCTION

Due to their low resistive losses, superconductors are currently used in a variety of microwave devices. In this paper, we present a superconducting microwave switch controlled by an applied DC voltage. With no applied voltage, the device transmits the signal with negligible loss. When a DC bias is applied, the superconductor becomes lossy, and the signal is attenuated. We have investigated the DC switching characteristics of a superconducting transmission line and have fabricated a microwave switch incorporating the transmission line.

II. EXPERIMENTAL

Devices were produced using a diced 5 cm diameter, 2000 Å thick Conductus $YBa_2Cu_3O_{7-\delta}$ film on a 508 μm thick $LaAlO_3$ substrate with a CeO_2 buffer layer. The wafer was diced into 1 cm squares, and devices were fabricated using photolithography and wet etching. A 0.001M citric acid solution was used for etching [1]. Contacts consisting of 1000Å silver and 4000Å gold were vacuum deposited and patterned using a liftoff technique. The contacts were annealed in flowing oxygen at 400°C for 45 minutes. DC current-voltage (IV) measurements were made using a four lead arrangement as shown in Fig. 1. Once DC measurements were complete, the device was mounted in a custom designed microwave housing. Wiltron K connectors were attached to the contact pads using ultrasonic bonding. Microwave measurements of transmission (S_{21}) and reflection (S_{11}) coefficients were made using an HP8510 network analyzer from 1 to 30 GHz. Low frequency measurements from 100 kHz to 0.2 GHz were made with an HP3577A network analyzer. For all microwave measurements, the DC bias was applied through the internal bias-tee of the network analyzer.

To ensure identical thermal environments, both DC and microwave measurements were made with the devices immersed in liquid nitrogen.

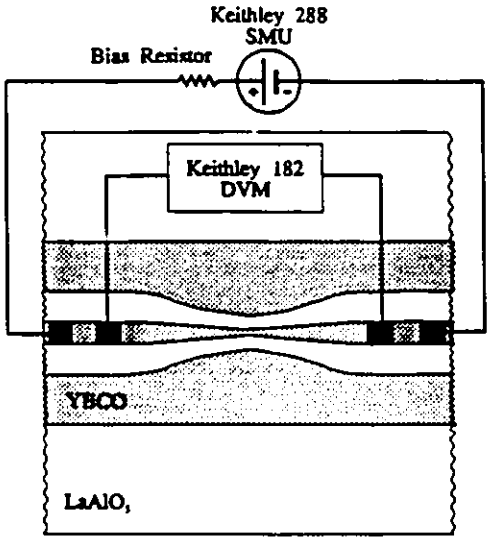

Fig 1. Microwave switch shown with the four point measurement apparatus for measuring the DC IV curve. Microwave measurements are made with the device mounted in a housing, and the DC bias is applied using a bias-tee.

III. CIRCUIT DESIGN

Shown in Fig. 1 is a typical device consisting of a coplanar waveguide (CPW) transmission line with a centre conductor tapering from a width of 150 μm to 10 μm. In order to maintain a 50Ω characteristic impedance throughout the entire transmission line, the ground planes are also tapered [2]. A key difference between a microstrip transmission line and a coplanar waveguide transmission line is that the impedance of CPW is a function of both the width of the center conductor and the gap between the center conductor and the ground plane. This feature allows transmission lines with narrow center conductors to be fabricated. Since the DC bias is applied only to the centre conductor, this reduces the critical current of the line, allowing switching to occur at lower power levels.

It is important to minimize any impedance mismatches in the transmission line since mismatches result in spurious microwave reflections, cause undesirable device resonances, and limit the operating bandwidth of the device.

The type of CPW used is an important design issue. The use of conductor backed CPW (CBCPW) is a desirable feature for cooling of the device. However, it has recently been shown [3] that the use of a conductor backing, particularly when the device is mounted in a housing, results in serious resonance problems due to microstrip like modes. We have therefore used CPW without conductor backing for the work described below.

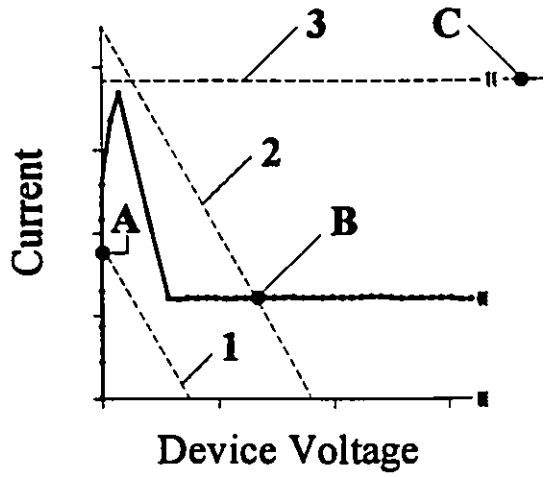

Fig. 2. Schematic IV curve with load lines shown. The load line slop is -1/R (where R is the total resistance in the external bias circuit) and the x-intercept is the applied voltage

It is also important to point out why DC voltages rather than currents are used to bias the transmission line. Fig. 2 shows a typical IV curve for the device. The reasons for the shape of the IV curve will be discussed in the next section, however, the device characteristic is nonlinear, so the DC operating point can be determined using a load line. For small applied voltages, load line **1** applies, and the operating point will be at **A**. For a larger applied voltage, load line **2** applies, the operating point is at **B**, and the device has switched. The use of current biasing is shown schematically with load line **3**. The operating point will be at **C**, so much greater power is dissipated and device damage is probable.

IV. MEASUREMENTS

A. DC Measurements

The DC IV characteristics of the device are shown in Fig. 3a. For small applied voltages, current flows with no voltage across the bridge. As the applied voltage is increased, small losses appear in the superconductor. These losses are likely due to flux flow [4] and result in a small amount of power dissipated by the device. This power appears as heat which must be removed by the system. At higher voltages, more heat is generated, and eventually more heat is generated than can be dissipated. The temperature rises rapidly in a localized region of the film, and a 'hot spot' forms [5]. The current drops sharply once the hot spot forms, and remains approximately constant as the applied voltage is further increased, suggesting that the device can be used as a current regulator. The fact that the current is reduced allows most of the bridge to remain fully superconducting; only the small hot spot is lossy. The resistance of the device therefore increases linearly with the bridge voltage, also shown in Fig. 3a. A plausible explanation for this is that the length of the 'hot spot' and therefore its resistance, increases linearly with the applied voltage. The DC resistance of the device is therefore adjustable from 0Ω with no applied bias, to 500Ω with an 8 Volt bias. Fig. 3b shows the resistance as a function of power dissipation. Increased resistance is only attainable at increased power dissipation levels.

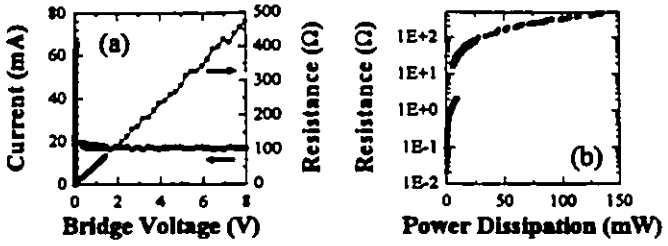

Fig. 3. DC measurements for the device shown in Fig. 1. 3(a) shows the IV characteristic and bridge resistance vs. bridge voltage. 3(b) shows the resistance vs. power dissipation for a DC voltage biased bridge.

B. Microwave Measurements

Microwave measurements of the device shown in Fig. 1 are shown in Fig. 4 The microwave transmission is modulated by the applied DC bias. Clearly, larger DC bias voltages result in larger signal attenuation. An attenuation of ≈20 dB occurs for a 15V applied bias. Fluctuations in the transmission coefficient are due to an impedance mismatch in the transmission line. This particular device was initially designed to be used with a backside ground plane. As discussed in Section III, this results in poor performance. The measurements shown in Fig. 4 were made using the design for CBCPW, but without the backside ground plane, resulting in an impedance mismatch.

The dynamic resistance of the hotspot can be extracted from the transmission measurement. For a series impedance Z in a 50Ω transmission line, the transmission coefficient is S_{21}=100/(100+Z) [6]. The dynamic resistance Z can therefore be determined from the measured data in Fig. 4. Neglecting the mismatch ripple, the dynamic resistance is found to equal the *DC resistance* of the bridge, rather than the slope of the IV curve as one would expect on a cursory examination of the system. Normally, the DC bias fixes the operating point of the device, and the microwave signal

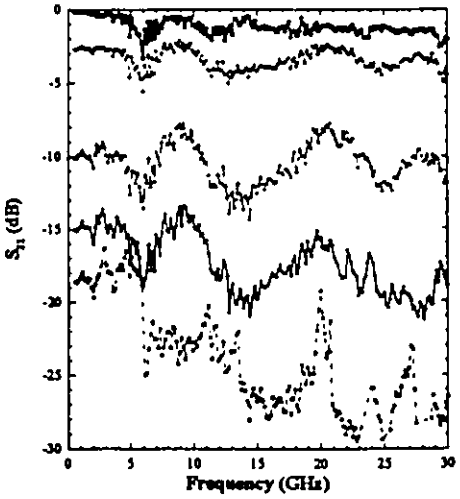

Fig. 4. Transmission coefficient vs. frequency at 77K unbiased (■), and biased with 1V(●), 5V(▲), 10V(★) and 15V(✱). The incident microwave power was 10 mW.

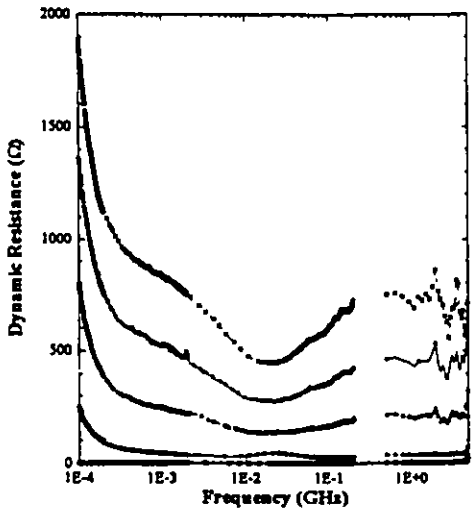

Fig. 5. Dynamic resistance of CPW transmission line at lower frequencies computed from transmission coefficients. Data is for DC voltage bias of 0V (■), 1V(●), 5V(▲), 10V(★) and 15V(✱).

acts as a small signal, but this is not the case here. We interpret this as meaning that the hotspot can not respond quickly enough to the microwave signal, but instead responds only to the average signal present.

By measuring the transmission coefficient at lower frequencies, one can estimate the hot spot response time. Fig. 5 shows the results of measurements at lower frequencies. At frequencies above 100 MHz, the microwave resistance equals the DC resistance. Below 1 MHz , the microwave resistance increases, indicating that the hot spot response time toapplied signals is approximately 1 μs. This is not the switching speed, but rather this indicates how fast the hot spot can respond to an applied voltage. In general, very little work has been done investigating switching speeds. However, switching times of less than 1 ns have been reported [7] for a current biased transmission line.

V. CONCLUSIONS

DC voltage biasing of superconductors causes switching between a low impedance and a high impedance state. A voltage bias applied to a superconducting bridge results in the formation of a thermal hot spot. When a DC voltage bias is combined with a microwave transmission line, a microwave switch results. Microwave signals are attenuated by the high impedance hot spot. The attenuation can be varied continuously by changing the DC bias voltage. At microwave frequencies, the response time of the hot spot is much slower than the applied signal. The microwave resistance therefore equals the DC resistance. At lower frequencies, the microwave resistance approaches the true dynamic resistance given by the slope of the IV curve. By measuring the frequency dependence of the microwave resistance, the intrinsic response time of the hot spot is estimated to be 1μs.

REFERENCES

[1] D.S. Ginley et al., "Di- and Tricarbolic-acid-based etches for processing high temperature superconducting thin films," *Appl. Phys. Lett., vol* 63, pp. 2429-2431, 1993.

[2] Brian C. Wadell, *Transmission Line Design Handbook*, Artech House, 1991, pp. 73-75.

[3] C.C. Tien, C.K.C. Tzuang, S.T. Peng, and C.C. Chang, "Transmission characteristics of finite-width conductor-backed coplanar waveguide," *IEEE Trans. Microwave Theory Tech.* vol. 41, pp. 1616-1623, 1993.

[4] E.H. Brandt, "The flux-line lattice in high T_c superconductors", *Journal of Superconductivity*, vol. 6, no. 4, pp. 201-217, 1993.

[5] W.J. Skocpol, M.R. Beasley, and M. Tinkham, "Self-heating hotspots in superconducting thin-film microbridges," *J. App. Phys.*, vol. 45, pp. 4054-4066, September 1974.

[6] D.M. Pozar, "*Microwave Engineering*", Addison-Wesley, 1990, pp.231-237.

[7] A. Frenkel, T. Venkatesan, C. Lin, X.D. Wu, and A. Inam, "Dynamic electrical response of YBCO," *J. App.Phys*, vol. 67, pp. 3767-3775, April 1990.

Paper B

"Current-Voltage Characteristics of DC Voltage Biased High Temperature Superconducting Microbridges"

G. Darcy Poulin, Jean Lachapelle, Frank A. Hegmann,
Steven H. Moffat, and John S. Preston.

Appl. Phys. Lett. **66**, 2576 (1995).

Summary:

The following paper describes our thermal hotspot modelling. Much of the material presented in Chapter 3 was taken from it. The paper presents, for the first time, a model that explains the observed I-V characteristics of high temperature superconducting bridges when biased with a DC voltage.

Current–voltage characteristics of dc voltage biased high temperature superconducting microbridges

G. Darcy Poulin, Jean Lachapelle, Steven H. Moffat, Frank A. Hegmann, and John S. Preston
Dept. of Engineering Physics, McMaster University, 1280 Main Street West, Hamilton, Ontario, L8S 4L7, Canada

(Received 16 January 1995; accepted for publication 7 March 1995)

We have investigated the dc current–voltage characteristic of high temperature superconducting microbridges. When a dc voltage is applied to a microbridge, it switches to a lossy state due to the formation of a hotspot in the bridge. We have measured the length and temperature of the hotspot as a function of the applied voltage, and have developed a thermal model to explain its steady state behavior. The hotspot has a flat-topped temperature profile, with the maximum temperature independent of the applied voltage. The length of the hotspot, and hence the bridge resistance, increases linearly with the applied bias, so the current is independent of the applied voltage once switching has occurred. © *1995 American Institute of Physics.*

There is considerable interest in studying transport properties of high-temperature superconducting (HTS) thin films for potential device applications. HTS materials exhibit a peculiar response when biased with a dc voltage; they switch to a virtually constant current state, independent of the applied bias. In this paper, we investigate the origin of this response.

Figure 1 shows a typical dc current–voltage (I-V) curve for a 10 μm wide bridge. At low voltages the resistive losses due to flux creep or thermally activated flux flow[1-3] are small and can be dissipated by the cryogen. If the heat generation exceeds the dissipation rate, a section of the bridge spontaneously heats up above the critical temperature. This hotspot is resistive so the current abruptly drops and the bridge is in the switched state.[4,5] Voltage, rather than current, biasing results in safer operation in the switched state.[6] A model describing the formation of the hotspot was developed for conventional superconductors.[7] However, the linear temperature dependence of the resistivity in HTS materials leads to a switching behavior.

We consider a simple one-dimensional heat flow model for a bridge of length L, width W, and thickness d, biased so a hotspot exists. We assume that thermal conduction takes place along the bridge, and each point along the bridge is linearly coupled to a bath at temperature T_b. The resistivity ρ is assumed to be a step function, increasing linearly with temperature above T_c. The slope of the ρ-T curve is c and the zero temperature intercept is ρ_0. The appropriate one-dimensional heat flow equations are

$$-K_N\frac{d^2T}{dx^2}+\frac{\alpha}{d}(T-T_b)=\left(\frac{I}{wd}\right)^2(cT+\rho_0)\quad(|x|\leq x_0),$$
$$-K_S\frac{d^2T}{dx^2}+\frac{\alpha}{d}(T-T_b)=0\quad(|x|\geq x_0), \tag{1}$$

where K_N and K_S are the thermal conductivities of the film in the normal and superconducting states, T is the film temperature, α is the heat transfer coefficient to the bath, I is the current, and x_0 is the hotspot boundary, defined as the position where $T=T_c$. Applying the boundary condition $T(\pm L/2)=T_b$, the symmetric solution to the temperature distribution is

$$T_N(x)=\beta\eta_N^2+(T_c-\beta\eta_N^2)\left[\frac{\cosh\left(\frac{x}{\eta_N}\right)}{\cosh\left(\frac{x_0}{\eta_N}\right)}\right]\quad(|x|\leq x_0),$$
$$T_S(x)=T_b+(T_c-T_b)\left[\frac{\sinh\left(\frac{L/2-x}{\eta_S}\right)}{\sinh\left(\frac{L/2-x_0}{\eta_S}\right)}\right]\quad(|x|\geq x_0), \tag{2}$$

where

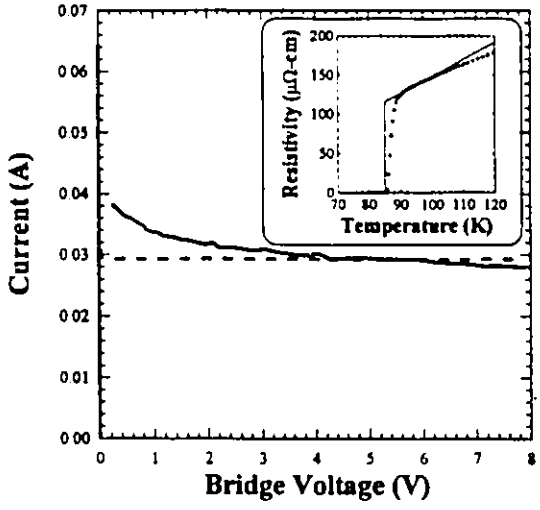

FIG. 1. Measured (solid line) and modeled (dashed line) I-V curve for a dc voltage biased bridge. The critical current is 22 mA based on the 1 μV/cm criterion, but because of the large voltage scale, these small losses are not noticeable. A hotspot is formed when the current reaches 64 mA. The inset shows the measured ρ-T curve (■). The solid line is a linear fit to the measured data centered at T=95 K and gives c=2.164 $\mu\Omega$ cm/K and $\rho_0=-68.188$ $\mu\Omega$ cm.

 0003-6951/95/66(19)/2576/3/$6.00

$$\beta=\frac{T_b\alpha W^2 d+\rho_0 I^2}{K_N W^2 d^2},$$

$$\eta_N=\sqrt{\frac{K_N d}{\alpha}}\left(1-\frac{cI^2}{\alpha W^2 d}\right)^{-1/2},$$

and

$$\eta_S=\sqrt{\frac{K_S d}{\alpha}}.$$

We refer to η_N and η_S as the thermal healing length in the normal and superconducting regions, respectively; their sum determines the length of the transition between the hotspot and superconducting region. When a further boundary condition $K_N(dT_N/dx)=K_S(dT_S/dx)$ at $x=\pm x_0$ is imposed, an expression is obtained for the current:

$$(T_c-\beta\eta_N^2)\tanh\left(\frac{x_0}{\eta_N}\right)=-\left(\frac{K_S}{K_N}\right)\left(\frac{\eta_N}{\eta_S}\right)(T_c-T_b)\coth\left(\frac{L/2-x_0}{\eta_S}\right). \quad (3)$$

After setting x_0, Eq. (3) is solved iteratively for β and η_N to get I. Equation (2) can then be used to obtain the temperature distribution. Since this determines the resistivity, we can determine the voltage by integrating across the bridge. Repeating the procedure for different values of x_0 determines the temperature distribution and current for different bridge voltages.

The solutions are simplified if $\rho_0=0$, $K_S=K_N$, and $\eta_N \ll x_0 \ll L/2-\eta_S$. The first two conditions are good approximations for HTS materials while the third is valid if the current is approximately independent of the voltage. Then the current is

$$I=\sqrt{\frac{\alpha W^2 d}{c}}\left[1-\frac{T_b^2}{T_c^2}\right]^{1/2}, \quad (4)$$

$\beta\eta_N^2=T_c^2/T_b$, and the temperature at the center of the hotspot is T_c^2/T_b. The bridge voltage, neglecting the small voltage drop across the transition region, is

$$V=2x_0T_c\sqrt{\frac{\alpha c}{d}}\left[\frac{T_c^2}{T_b^2}-1\right]^{1/2}. \quad (5)$$

The films were 2000 Å thick $Y_1Ba_2Cu_3O_{7-\delta}$ from Conductus with $T_c=85$ K. The ρ-T curve, measured with a 10 μm wide, 450 mm long bridge is shown in the inset of Fig. 1. A series of ten 3 μm wide voltage taps was connected to the bridge at 50 μm intervals, and the voltage was measured at each tap with respect to tap 10 for a series of applied voltages. All measurements were carried out in liquid nitrogen. While theory predicts the hotspot will form at the center of the bridge, Fig. 2 shows it has nucleated at one end of the bridge, presumably at the narrowest region. The temperature can be determined as a function of position by measuring the voltage difference between adjacent taps. Since the current is known, the voltage difference is converted to resistivity and the temperature is determined from the ρ-T curve.

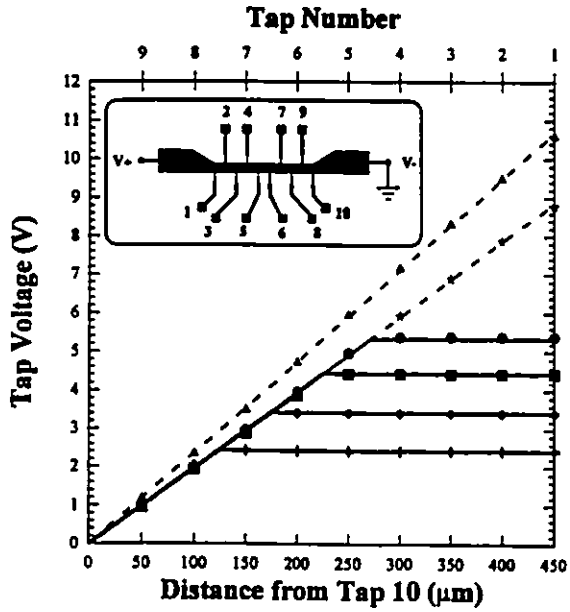

FIG. 2. Tap voltage measured as a function of position for bridge voltages of 2.4 (+), 3.4 (◆), 4.4 (■), 5.4 (●), 8.8 (★), and 10.6 (▲) volts. The data points are measured values, while the solid lines are determined from the thermal model. Since this model is only valid when the hotspot length is less than the length of the bridge, modeled results are not shown for the two largest voltages. The dashed lines are straight line fits to the data, and are guides to the eye only.

Thermal modeling was carried out, and comparisons were made with the experimental data. Since we had already measured the temperature of the hotspot to be 94 K, we obtained values for c and ρ_0 by doing a linear least squares fit to the ρ-T curve using data between 90 and 100 K. We assumed that[8] $K_S=K_N=0.1$ W cm^{-1}K^{-1}, then set x_0 to 112.5 μm and adjusted α until the modeled current matched the measured current. The resulting value, $\alpha=350$ W cm^{-2}K^{-1}, is in reasonable agreement with measured values.[9] These thermal parameters were fixed, and the temperature distribution, current, and voltage were determined for a range of values of x_0.

The modeled I-V curve is shown in Fig. 1. While the thermal model predicts that the current should be constant for voltages above about 100 mV, the measured current decreases slightly with increasing voltage and diverges from model predictions below 2 V. The modeled I-V curve can be broadened by increasing K_N and K_S, but the increases required to broaden the transition significantly are unphysical. We believe the disparity between modeled and measured results are caused by variations of the effective value of the heat transfer coefficient. In our model, α is a constant. However, it likely decreases as the hotspot grows, with lateral heat diffusion in the substrate near the ends of the hotspot becoming less significant. More exact modeling would require a full three dimensional solution of the thermal transport which we have not attempted.

Figure 2 shows measured and modeled tap voltages as a function of distance for a variety of bridge voltages. For voltages less than 8.8 V, our model predicts the length of the hotspot to be proportional to the voltage, since the tempera-

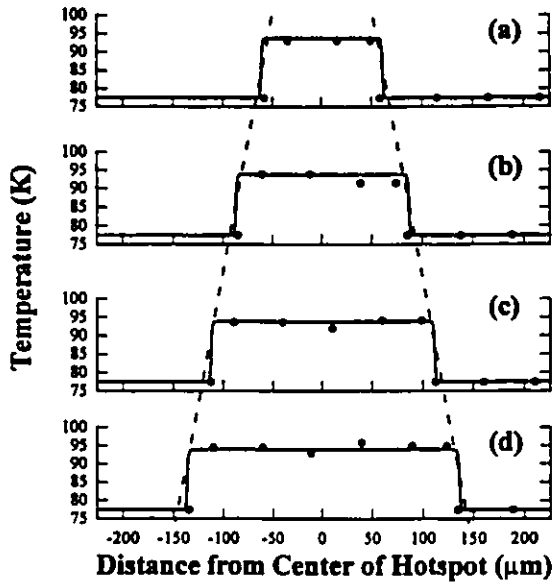

FIG. 3. Temperature as a function of position along the bridge for bridge voltages of (a) 2.4, (b) 3.4, (c) 4.4, and (d) 5.4 V. The data points are computed temperatures from Fig. 2, while the solid lines are calculated from the thermal model. The temperature remains constant at 94 K for all applied voltages.

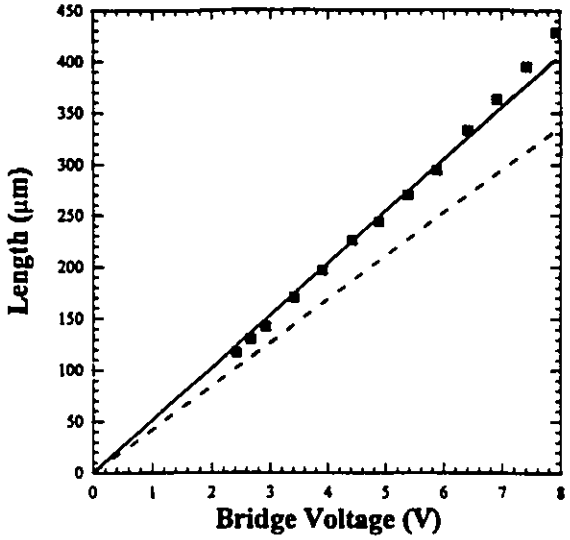

FIG. 4. Hotspot length as a function of bridge voltage. The data points are computed lengths from Fig. 2, while the solid line is calculated from the model. The dashed line is calculated from the simplified expression, Eq. (5).

ture is independent of length and is approximately T_c^2/T_b. The total voltage drop predicted from the modeled temperature distribution agrees well with the measured bridge voltage, even though we have approximated the ρ-T curve with a step function. Given the current flowing in the bridge, the transition will be significantly broadened. However, since the thermal healing lengths are much less than the length of the hotspot this leads to negligible differences in the total bridge voltage. Beyond 8.8 V, the entire bridge is heated, and the hotspot model is no longer applicable. The temperature is essentially uniform along the bridge and increases with increasing voltage. For the bridge voltage shown of 10.6 V, we obtain a temperature of 105 K from the slope of the fitted straight line.

Figure 3 shows the excellent agreement between the temperature distribution determined from Fig. 2 and the modeled temperature distribution. The temperature is flat-topped, and independent of the applied voltage. The endpoints of the measured hotspot temperature profile were determined by assuming a very narrow transition, and extrapolating the constant slope hotspot regions of Fig. 2 to find the intersection with the superconducting regions.

Figure 4 shows the hotspot length as a function of the bridge voltage. Some discrepancy between measured and modeled results occurs for hotspot lengths comparable to the bridge length since the temperature at the ends of the bridge can no longer be assumed to be fixed at T_b. Our measurements are limited to hotspots longer than about 100 μm since our tap spacing is 50 μm. The simple approximation for the hotspot length in Eq. (5) is also shown in the figure. It underestimates the hotspot length since, for the film investigated here, the resistivity offset ρ_0 is not zero.

When a superconductor is biased with a dc voltage, a hotspot spontaneously forms, causing the superconductor to switch to a lossy state. The temperature distribution has been measured, and the temperature of the hotspot was found to be flat topped and independent of the applied voltage. The length of the hotspot, and hence the bridge resistance, was found to increase linearly with the applied voltage. A one dimensional thermal model was developed to explain the measured I-V curve and temperature distribution. The model predicts the temperature of the hotspot will be approximately T_c^2/T_b, and the current will be constant and independent of the applied voltage, in good agreement with measured data.

This work was supported by the Natural Sciences and Engineering Research Council of Canada, and made use of the facilities of the Centre for Electrophotonic Materials and Devices. F.H., J.L., S.H.M., and G.D.P. all acknowledge financial support from NSERC postgraduate scholarships.

[1] E. H. Brandt, J. Supercond. 6, 201 (1993).
[2] M. Leghissa, A. Koniger, M. Lippert, W. Dorsch, M. Kraus, and G. Saemann-Ischenko, Z. Phys. B Condens. Matter 92, 163 (1993).
[3] T. T. M. Palstra, B. Batlogg, R. B. van Dover, L. F. Scheemeyer, and J. V. Waszczak, Phys. Rev. B 41, 6621 (1990).
[4] A. V. Gurevich and R. G. Mints, Rev. Mod. Phys. 59, 941 (1987).
[5] A. Sh. Fix, I. L. Maksimov, K. V. Morozov, and V. V. Osipov, IEEE Trans. Appl. Supercond. 3, 1608 (1993).
[6] G. Darcy Poulin, F. A. Hegmann, J. Lachapelle, S. H. Moffat, and J. S. Preston, IEEE Trans. Appl. Supercond. (to be published).
[7] W. J. Skocpol, M. R. Beasley, and M. Tinkham, J. Appl. Phys. 45, 4054 (1974).
[8] S. J. Hagen, Z. Z. Wang, and N. P. Ong, Phys. Rev. B 40, 9389 (1989).
[9] The heat transfer coefficient is approximated as the inverse of the thermal boundary resistance, giving estimates for the heat transfer coefficient of between 300 and 1250 W cm^{-2}K^{-1}. See for example, C. D. Marshall, A. Tokamoff, I. M. Fishman, C. B. Eom, Julia M. Phillips, and M. D. Fayer, J. Appl. Phys. 73, 850 (1993), or M. Nahum, S. Verghese, P. L. Richards, and K. Char, Appl. Phys. Lett. 59, 2034 (1991).